NAVAL POSTGRADUATE SCHOOL
Monterey, California

THESIS

REMOTELY SENSED DENSITY MEASUREMENTS OF VOLCANIC SULFUR DIOXIDE PLUMES USING A SPECTRAL LONG WAVE INFRARED IMAGER

by

Aimee Gail Mares

September 2002

Thesis Advisor:	Richard C. Olsen
Second Reader:	Paul G. Lucey

Approved for public release; distribution unlimited

THIS PAGE INTENTIONALLY LEFT BLANK

REPORT DOCUMENTATION PAGE			Form Approved OMB No. 0704-0188
Public reporting burden for this collection of information is estimated to average 1 hour per response, including the time for reviewing instruction, searching existing data sources, gathering and maintaining the data needed, and completing and reviewing the collection of information. Send comments regarding this burden estimate or any other aspect of this collection of information, including suggestions for reducing this burden, to Washington headquarters Services, Directorate for Information Operations and Reports, 1215 Jefferson Davis Highway, Suite 1204, Arlington, VA 22202-4302, and to the Office of Management and Budget, Paperwork Reduction Project (0704-0188) Washington DC 20503.			
1. AGENCY USE ONLY ***(Leave blank)***	**2. REPORT DATE** September 2002	**3. REPORT TYPE AND DATES COVERED** Master's Thesis	
4. TITLE AND SUBTITLE: Remotely Sensed Density Measurements of Volcanic Sulfur Dioxide Plumes Using a Spectral Long Wave Infrared Imager			**5. FUNDING NUMBERS**
6. AUTHOR(S) Aimee Gail Mares			
7. PERFORMING ORGANIZATION NAME(S) AND ADDRESS(ES) Naval Postgraduate School Monterey, CA 93943-5000			**8. PERFORMING ORGANIZATION REPORT NUMBER**
9. SPONSORING /MONITORING AGENCY NAME(S) AND ADDRESS(ES) N/A			**10. SPONSORING/MONITORING AGENCY REPORT NUMBER**
11. SUPPLEMENTARY NOTES The views expressed in this thesis are those of the author and do not reflect the official policy or position of the Department of Defense or the U.S. Government.			
12a. DISTRIBUTION / AVAILABILITY STATEMENT Approved for public release; distribution unlimited			**12b. DISTRIBUTION CODE**

13. ABSTRACT ***(maximum 200 words)***

This thesis examines the process of detecting and quantifying volcanic SO_2 plumes using the Airborne Hyperspectral Infrared Imager (AHI) developed by the University of Hawaii. AHI was flown over Pu'u'O'o Vent of Kilauea Volcano in Hawaii to collect data on SO_2 plumes. In conjunction with these observations, data were taken with the Hawaii Volcano Observatory's Correlation Spectrometer (COSPEC) and University of Hawaii's FLYSPEC. These are ultraviolet remote sensors with a successful history of monitoring volcanic SO_2 plumes at ~0.3 μ.

AHI is a LWIR pushbroom imager sensitive to the 7.5 – 11.5 μ region. Spectral analysis and mapping tools were used to identify and classify the SO_2 plume in both radiance and emissive space. MODTRAN was used to model the radiance observed by the sensor as it looked to the ground through an SO_2 plume. A spectral library of radiance profiles with varying ground surface temperatures and SO_2 concentrations was developed, and the AHI data fitted to the varying model profiles. Reasonable values of SO_2 emission were obtained, though the values directly over the vent obtained by AHI were much higher than those obtained by the UV sensors some distance away.

14. SUBJECT TERMS hypersepctral, airborne remote sensing, Long Wave Infrared (LWIR), Ultraviolet (UV), Sulfur Dioxide, gas detection, volcanic plumes, Airborne Hyperspectral Infrared Imager (AHI), FLYSPEC			**15. NUMBER OF PAGES** 147
			16. PRICE CODE
17. SECURITY CLASSIFICATION OF REPORT Unclassified	**18. SECURITY CLASSIFICATION OF THIS PAGE** Unclassified	**19. SECURITY CLASSIFICATION OF ABSTRACT** Unclassified	**20. LIMITATION OF ABSTRACT** UL

NSN 7540-01-280-5500

Standard Form 298 (Rev. 2-89)
Prescribed by ANSI Std. 239-18

THIS PAGE INTENTIONALLY LEFT BLANK

Approved for public release; distribution unlimited

REMOTELY SENSED DENSITY MEASUREMENTS OF VOLCANIC SULFUR DIOXIDE PLUMES USING A SPECTRAL LONG WAVE INFRARED IMAGER

Aimee G. Mares
Captain, United States Marine Corps
B.S., United States Naval Academy, 1995

Submitted in partial fulfillment of the
requirements for the degree of

MASTER OF SCIENCE IN SPACE SYSTEMS OPERATIONS

from the

NAVAL POSTGRADUATE SCHOOL
September 2002

Author: Aimee Gail Mares

Approved by: Richard C. Olsen
Thesis Advisor

Paul G. Lucey
Second Reader

Rudy Panholzer
Chairman, Space Systems Academic Group

THIS PAGE INTENTIONALLY LEFT BLANK

ABSTRACT

This thesis examines the process of detecting and quantifying volcanic SO_2 plumes using the Airborne Hyperspectral Infrared Imager (AHI) developed by the University of Hawaii. AHI was flown over Pu'u'O'o Vent of Kilauea Volcano in Hawaii to collect data on SO_2 plumes. In conjunction with these observations, data were taken with the Hawaii Volcano Observatory's Correlation Spectrometer (COSPEC) and University of Hawaii's FLYSPEC. These are ultraviolet remote sensors with a successful history of monitoring volcanic SO_2 plumes at ~0.3 μ.

AHI is a LWIR pushbroom imager sensitive to the 7.5 – 11.5 μ region. Spectral analysis and mapping tools were used to identify and classify the SO_2 plume in both radiance and emissive space. MODTRAN was used to model the radiance observed by the sensor as it looked to the ground through an SO_2 plume. A spectral library of radiance profiles with varying ground surface temperatures and SO_2 concentrations was developed, and the AHI data fitted to the varying model profiles. Reasonable values of SO_2 emission were obtained, though the values directly over the vent obtained by AHI were much higher than those obtained by the UV sensors some distance away.

THIS PAGE INTENTIONALLY LEFT BLANK

TABLE OF CONTENTS

I. INTRODUCTION **1**

II. ULTRAVIOLET DETECTION OF SO_2 ..... **5**
- **A. ULTRAVIOLET SESNORS** **5**
  - **1. COSPEC** **5**
    - ***a. System Design*** *5*
    - ***b. Sensor Design*** *7*
    - ***c. Data Collection Techniques*** *8*
    - ***d. Data Analysis and Calculations*** *10*
  - **2. FLYSPEC** **12**
    - ***a. System Design*** *12*
    - ***b. Sensor Design*** *14*
    - ***c. Data Collection Methods and Techniques*** *17*
    - ***d. Data Analysis and Calculations*** *18*
- **B. SULFUR DIOXIDE EMISSION RATES OF KILAUEA VOLCANO, HAWAII, USING UV SENSORS** **22**
- **C. SUMMARY OF UV DETECTION** **25**

III. INFRARED DETECTION OF SO_2 ..... **27**
- **A. AIRBORNE AND SPACEBORNE INFRARED SENSORS** **27**
  - **1. Thermal Infrared Multispectral Scanner (TIMS)** **28**
    - ***a. Sensor Design and Data Collection*** *28*
    - ***b. Data Analysis Techniques*** *30*
  - **2. Advanced Spaceborne Thermal Emission Reflection Radiometer (ASTER)** **38**
    - ***a. ASTER Description*** *38*
    - ***b. ASTER Simulation and Results*** *40*
  - **3. Airborne Hyperspectral Imager (AHI)** **42**
    - ***a. System Design*** *42*
    - ***b. Sensor Design*** *44*
    - ***c. Data Collection Techniques and Applications*** *47*
- **B. SUMMARY OF IR DETECTION** **50**

IV. DATA COLLECTION AND SO_2 DETECTION **51**
- **A. DATA COLLECTION** **51**
  - **1. Weather Conditions** **51**
  - **2. COSPEC and FLYSPEC Data Collection** **52**
  - **3. AHI Data Collection** **53**
- **B. SO_2 DETECTION** **54**
  - **1. Initial Detection** **55**
  - **2. Application of Spectral Classification Tools** **56**
    - ***a. Conversion From Radiance to Emissive Space*** *57*
    - ***b. Application of Spectral Classification Tools*** *62*

3. Development of Spectral Libraries. 68
C. SUMMARY OF SO_2 DETECTION 72

V. QUANTIFICATION OF SO_2 DETECTIONS 73
A. MODTRAN 73
1. Inputs 73
2. Outputs 74
3. MODTRAN Model Examples. 74
B. AHI DATA CHOSEN FOR ANALYSIS 76
C. AHI DATA ANALYSIS RESULTS 78
1. SO_2 Class Results 78
a. Red Class 78
b. Orange Class 79
c. Orchid Class 80
d. Cyan Class 81
e. Green and Blue Classes 82
f. Class Summary 84
2. COSPEC / FLYSPEC Results 85
D. SUMMARY 87

VI. SUMMARY AND CONCLUSIONS 89

APPENDIX A. FALSE COLOR SIMULATED TIMS IMAGES WITH DECORRELATION STRETCH APPLIED 93

APPENDIX B. MODTRAN CODE 111

APPENDIX C. MODTRAN AND AHI RADIANCE PROFILE COMPARISONS 113

LIST OF REFERENCES 123

INITIAL DISTRIBUTION LIST 127

LIST OF FIGURES

Figure 1. COSPEC System Components of Data Collection Segment 6
Figure 2. COSPEC System Inputs, Components, and Outputs Used for Data Collection Segment 6
Figure 3. COSPEC System Inputs, Components, and Outputs of the Data Analysis Segment 7
Figure 4. COSPEC Sensor Components (After Barringer, Figure 1, p. 8)..... 8
Figure 5. Ideal Scenario for Collecting Data Using the Ground Mobile Technique..... 9
Figure 6. Simulated COSPEC Absorption Profile Illustrating Variables Used in the Concentration Path Length Calculation in Equation 1.1..... 11
Figure 7. FLYSPEC System Components Used in the Data Collection Segment 13
Figure 8. FLYSPEC System Inputs, Components, and Outputs Used in the Data Collection Segment 14
Figure 9. FLYSPEC System Inputs, Components, and Outputs Used in the Data Analysis Segment 14
Figure 10. FLYSPEC Sensor Components (After Bo Galle, Figure 5, p.40)..... 15
Figure 11. FLYSPEC Telescope and Calibration Cells 16
Figure 12. Concurrent Data Collection with COSPEC and FLYSPEC Using the Ground Mobile Technique 17
Figure 13. SO_2 Absorption Spectrum in UV Spectral Region (After Galle, Figure 2., p.17)..... 18
Figure 14. Example Reference, Dark, and Sample Data frames collected by FLYSPEC during traverse on Kilauea Volcano, Hawaii on March 4, 2002... 19
Figure 15. FLYSPEC's Calibration Cell Spectrum and Concentration Path Length Plot for a March 4, 2002, Traverse On Kilauea Volcano, Hawaii 20
Figure 16. FYSPEC Data Text Format Stored During Data Collection..... 21
Figure 17. Typical Routes for Vehicle-Based Traverses of Kilauea Caldera and East Rift Zone (After Sutton et al., Figure 1., p.284)..... 23
Figure 18. Long Term Data Set Of Emission Rates Determined By COSPEC For The Kilauea Summit Caldera Area (From Elias et al., Figure 3., p.5) 24
Figure 19. Long Term Data Set Of Emission Rates Determined By COSPEC For The Chain of Craters Road Area (From Elias et al., Figure 4., p.6)..... 25
Figure 20. Scanning Multispectral Data Collection And Resulting Data Cube 29
Figure 21. Atmospheric Transmission Profiles With and Without SO_2 (from Realmuto et al., Figure 2, p.483)..... 32
Figure 22. Decorrelation Stretch Applied To TIMS Image Data (Realmuto et al., Figure 2, p. 15060) 33
Figure 23. Estimation Maps of Ground Temperature and SO_2 Column Abundance Generated For Pu'u'O'o Vent Of Kilauea Volcano, Hawaii (after Realmuto et al., Figure 3 and Figure 4, p. 15061 – 15062)..... 35
Figure 24. Typical Pahoehoe And Aa Lava Flows..... 35

Figure 25. Spectral Response for ASTER's TIR Subsystem (from Hook, "Instrument") 39
Figure 26. Simulation Data With A Decorrelation Stretch Applied (after Realmuto et al., Plate 1, p. 106) 40
Figure 27. Comparison of Pu'u'O'o Plume Maps At Spatial Resolutions of TIMS and ASTER (After Realmuto et al., Plate 1, p.106) 41
Figure 28. Results of ASTER's Sensitivity Simulation (After Realmuto et al., Plate 1, p.106) 41
Figure 29. AHI System Components (after Lucey et al., Figure 3, p. 41) 43
Figure 30. AHI System Mounted In A Twin Otter Fixed Wing Aircraft 43
Figure 31. Snapshot of AHI's Monitor Display 44
Figure 32. Main Subsystems of the Sensor Design (from Lucey et al., Figure 1, p. 37) . 45
Figure 33. Main Components of Sensor Subsystems (after Lucey et al., Figure 3, p. 41) 45
Figure 34. Pushbroom Hyperspectral Data Collection and Resulting Data Cube 47
Figure 35. AHI Collection Platforms: Helicopter, Ground Based, and Fixed Wing Aircraft 48
Figure 36. Single Band Images and Single Pixel Spectra Demonstrating AHI's Gas Detection Capability (from Lucey et al., 2000, p. 35) 49
Figure 37. Using Matched Filter On Single Band Images Indicating Gas Detection In Hashed Area (from Lucey et al., 2000, p. 36) 49
Figure 38. Visible and Infrared Image of Pu'u'O'o Vent of Kilauea Volcano, Hawaii, Collected on April 18, 2002 51
Figure 39. Routes of Data Collection for COSPEC, FLYSPEC, and AHI on April 18, 2002 53
Figure 40. False Color RGB Radiance Image Generated by the Decorrelation Stretch Method 55
Figure 41. Radiance Spectra of Yellow Pixels Demonstrating the SO_2 Absorption Feature 56
Figure 42. R1_C_095349 Emissivity and Temperature Images Generated By the Normalized Emissivity Method and the Corresponding Radiance Image 59
Figure 43. R1_C_095349 Black Body and AHI Radiance Comparison With Corresponding Emissivity Plot 59
Figure 44. R1_A_093718 Emissivity and Temperature Images Generated By the Normalized Emissivity Method and the Corresponding Radiance Image 60
Figure 45. R1_A_093718 Black Body and AHI Radiance Comparison of Lava Pixels With Corresponding Emissivity Plot 61
Figure 46. R1_A_093718 Black Body and AHI Radiance Comparison of Water Pixels 61
Figure 47. Regions of Interest Used in the Application of Spectral Mapping Tools 63
Figure 48. Initial SAM Results in Radiance and Emissive Space 64
Figure 49. SAM Rule Images for Red and Orange SO2 Classes in Radiance and Emissive Space 64
Figure 50. Scatter Plots of SAM SO_2 Rules in Radiance and Emissive Space for the Red and Orange SO_2 Classes 65

Figure 51. MF Gray-Scale Images for Orange and Red Classes of SO_2 in Radiance and Emissive Space 66
Figure 52. Scatter Plots of MF SO_2 Results in Radiance and Emissive Space for the Red and Orange SO_2 Classes 66
Figure 53. Scatter Plot of SAM and MF Results for SO_2 Classes in Radiance Space 67
Figure 54. Scatter Plot of SAM and MF Results for SO_2 Classes in Emissive Space..... 68
Figure 55. 2-D Scatter Plot of SO2 Classes in Radiance Space Using PC Bands 1 and 2 and the Corresponding Radiance Spectral Library of the SO_2 Classes..... 69
Figure 56. 5-D Scatter Plot of SO2 Classes in Emissivity Space Using the First Five PC Bands and the Corresponding Emissivity Spectral Library of the SO_2 Classes 70
Figure 57. R1_C_095349 Radiance Image With Final SO_2 Classes Annotated 71
Figure 58. MODTRAN Standard Atmospheric Profile 75
Figure 59. MODTRAN Radiance and Relative Radiance Model Profiles for Multiple Concentrations of SO_2 at 350 K and 380 K 75
Figure 60. X-Y Coordinates of Pixel Blocks in the Plume Chosen for Analysis 77
Figure 61. Upper, Lower, and Mid Plume Section AHI – MODTRAN Comparison Plots for the Red Class 78
Figure 62. Upper and Lower Plume Section AHI – MODTRAN Comparison Plots for the Orange Class..... 80
Figure 63. Lower Plume Section AHI – MODTRAN Comparison Plots for the Orchid Class 80
Figure 64. Upper Plume Section AHI – MODTRAN Comparison Plots for the Cyan Class 81
Figure 65. Upper Plume Section AHI – MODTRAN Comparison Plots for the Green Class 82
Figure 66. Lower Plume Section AHI – MODTRAN Comparison Plots for the Blue Class 83
Figure 67. Summary of MODTRAN Ground Surface Temperatures and SO_2 Concentrations Producing the Best Fit to Corresponding AHI Data 84
Figure 68. Plots of Data Collected Simultaneously by COSPEC and FLYSPEC Traveling Northeast on Highway 11 from 0958 to 1028 on April 18, 2002... 86
Figure 69. Plot of Data Collected Simultaneously by COSPEC and FLYSPEC Traveling Southwest on Highway 11 from 1030 to 1056 on April 18, 2002.. 86
Figure 70. Decorrelation Stretch Applied to Simulated TIMS Image of R1_A_093134. 93
Figure 71. Decorrelation Stretch Applied to Simulated TIMS Image of R1_A_093226. 94
Figure 72. Decorrelation Stretch Applied to Simulated TIMS Image of R1_A_093433. 95
Figure 73. Decorrelation Stretch Applied to Simulated TIMS Image of R1_A_093525. 96
Figure 74. Decorrelation Stretch Applied to Simulated TIMS Image of R1_A_093618. 97
Figure 75. Decorrelation Stretch Applied to Simulated TIMS Image of R1_A_093718. 98
Figure 76. Decorrelation Stretch Applied to Simulated TIMS Image of R1_B_094450. 99
Figure 77. Decorrelation Stretch Applied to Simulated TIMS Image of R1_B_094542 100
Figure 78. Decorrelation Stretch Applied to Simulated TIMS Image of R1_B_094635 101
Figure 79. Decorrelation Stretch Applied to Simulated TIMS Image of R1_C_095258 102
Figure 80. Decorrelation Stretch Applied to Simulated TIMS Image of R1_C_095349 103

Figure 81. Decorrelation Stretch Applied to Simulated TIMS Image of R2_B_100030 104
Figure 82. Decorrelation Stretch Applied to Simulated TIMS Image of R2_B_100121 105
Figure 83. Decorrelation Stretch Applied to Simulated TIMS Image of R2_B_100213 106
Figure 84. Decorrelation Stretch Applied to Simulated TIMS Image of R2_B_100312 107
Figure 85. Decorrelation Stretch Applied to Simulated TIMS Image of R2_B_100403 108
Figure 86. Decorrelation Stretch Applied to Simulated TIMS Image of R2_B_100455 109
Figure 87. Decorrelation Stretch Applied to Simulated TIMS Image of R2_B_100549 110
Figure 88. MODTRAN Code Used for AHI Data Analysis 111
Figure 89. MODTRAN and AHI Radiance Profile Comparison for Pixels of the Red SO_2 Class 113
Figure 90. MODTRAN and AHI Radiance Profile Comparison for Pixels of the Red SO_2 Class Continued 114
Figure 91. MODTRAN and AHI Radiance Profile Comparison for Pixels of the Red SO_2 Class End 115
Figure 92. MODTRAN and AHI Radiance Profile Comparison for Pixels of the Orange SO_2 Class 116
Figure 93. MODTRAN and AHI Radiance Profile Comparison for Pixels of the Orange SO_2 Class Continued 117
Figure 94. MODTRAN and AHI Radiance Profile Comparison for Pixels of the Orange SO_2 Class End and for Pixels of the Green SO_2 Class 118
Figure 95. MODTRAN and AHI Radiance Profile Comparison for Pixels of the Orchid SO_2 Class 119
Figure 96. MODTRAN and AHI Radiance Profile Comparison for Pixels of the Orchid SO_2 Class 120
Figure 97. MODTRAN and AHI Radiance Profile Comparison for Pixels of the Orchid SO_2 Class 121

LIST OF TABLES

Table 1. Remote Sensing Instruments Used In Volcanic Monitoring (after Mouginis-Mark, et al., Appendix 3., p. 269) 2
Table 2. Physical and Performance Specifications of the COSPEC and FLYSPEC sensors 16
Table 3. TIMS Sensor Specifications 29
Table 4. MODTRAN's Required Inputs And Respective Sources 31
Table 5. Quantified TIMS Results Of Pu'u'O'o Data Collected On September 30, 1988 (After Realmuto et al., 1997, p. 15066) 35
Table 6. Comparison of TIMS and COSPEC Results 37
Table 7. Sensitivity Analysis Results For SO_2 For Plume Mapping Procedure 38
Table 8. Characteristics of ASTER's Three Subsystems (after Hook, "Instrument") .. 39
Table 9. Physical and Performance Specifications of the AHI System and Sensor..... 46
Table 10. Summary of Files Produced From AHI Data Collection 54
Table 11. SO_2 Class Temperature Statistics 71
Table 12. AHI Pixel Data Chosen for Analysis 77
Table 13. Maximum and Minimum Temperature and SO_2 Results for the Red Class ... 79
Table 14. Maximum and Minimum Temperature and SO_2 Results for the Orange Class 80
Table 15. Maximum and Minimum Temperature and SO_2 Results for the Orchid Class 81
Table 16. Maximum and Minimum Temperature and SO_2 Results for the Cyan Class . 82
Table 17. Maximum and Minimum Temperature and SO_2 Results for the Green Class 83
Table 18. Maximum and Minimum Temperature and SO_2 Results for the Blue Class .. 84
Table 19. Summary of MODTRAN Ground Surface Temperatures and SO_2 Concentrations Producing the Best Fit to Corresponding AHI Data 85

THIS PAGE INTENTIONALLY LEFT BLANK

ACKNOWLEDGMENTS

What a great experience this has been, and it would not have been possible without several people I would like to thank. I would like to thank Professor Olsen for giving me the opportunity to work with the incredibly talented and knowledgeable faculty and staff of the Hawaii Institute of Geophysics and Planetology (HIGP) at the University of Hawaii at Manoa. Thanks to Doctor Paul Lucey for welcoming me to HIGP and for your valuable time. Thank you for providing AHI on multiple occasions (thanks to Mother Nature) to collect the data. I'd also like to thank you for showing me that it *does* snow in Hawaii! Thanks to Doctor Keith Horton for the countless hours of teaching, guidance, and mentoring. Thank you for all of the hard work involved in providing FLYSPEC for the data collection. I truly appreciated the chance to be in the field collecting data for this project and learned that collecting the data is almost as difficult as analyzing it sometimes! I learned several very important things from working with you, and just to name a few: always file important things in temp/junk folders, always know where the reset button is, you can never have enough duck tape when you go to the field, never throw away the vegetable rubberbands, and last but not least, blueberry gravy has a pretty interesting taste. If you see Joan again anytime soon, pass a hello onto her. Thanks to Harold for helping make the data collection with FLYSPEC possible. I know you will forever have a soft spot in your heart for palm pilots! Thanks to Tim and Dave for the hard work in getting AHI prepped for the flights and thanks to Dave, for braving the multiple flights it took to get the data collected. Thanks to Eric for all of the computer support, and thanks to Mike Winter for the many trips to the post office to ensure the data made it to Monterey. I enjoyed the experience tour with all of you and hope to stay in touch.

I'd also like to thank both Tamar Elias and Jeff Sutton of the Hawaii Volcano Observatory. I really enjoyed getting to work with you and the chance to see COSPEC operating first hand. I appreciated your patience, cooperation, and enthusiasm, and the many "spur of the moment" data collections. It was fantastic to learn about the valuable work you do for the volcanology community. The experience generated a newfound interest for me. I hope to be back again some day.

Thanks again to Professor Olsen for helping me develop an appreciation for "real science". I truly appreciated the opportunity to participate in the data collection, and I appreciated the encouragement to maintain the diligence it took to get the data. I learned a tremendous amount from the experience. Thank you also for the many hours of patience and guidance in analyzing the data. The "powers of IDL" are now well recognized. (I know Keith and Paul will appreciate that one too.)

Finally, thanks to my family and friends spread across the country who gave me many hours of support and encouragement over the phone via e-mail and even visits out to Monterey. I couldn't have accomplished anything without you. A special thanks goes to my husband, Jeff. I know you didn't expect to find snow in Hawaii either. You made a great "research buddy" at the top of Mauna Kea, not to mention coming up with a brilliant way of returning equipment to a rental store when it was already closed. Thanks for listening to the many hours of babble about sensors, data, volcanoes, and space. To all of my family and friends, your patience, love, support, and encouragement throughout these two years of school will not be forgotten.

I. INTRODUCTION

The modern science of volcanology originated in Hawaii with the establishment of the Hawaiian Volcano Observatory (HVO) in 1912. Prior to the advent of volcanology, volcanoes were generally only studied after a major eruption. In the early 1900's, Thomas A. Jaggar, Jr., a geologist at the Massachusetts Institute of Technology (MIT) started promoting a continuous study of volcanoes. He believed that scientists would gain a better understanding of volcanoes if studies were conducted before, during, and after eruptions. His beliefs compelled the residents of Hawaii to establish the Hawaiian Volcano Research Association (HVRA). With assistance from HVRA and the Whitney Fund of MIT, Jagger established the HVO. Today, the HVO is operated by the U.S. Geological Survey (USGS). (Tilling, R., Heliker, C., and Wright, T., "Eruptions of Hawaiian Volcanoes")

The mission of HVO is to monitor Hawaii's Mauna Loa and Kilauea Volcanoes. "The term volcano monitoring refers to the observations and measurements scientists make to document changes in the state of the volcano during and between eruptions." (Watson, "Eruptions of Hawaiian Volcanoes") Through this continuous and close monitoring, the scientists can help protect the people of Hawaii and their property by issuing timely warnings of hazardous activity. Lava flows and explosive eruptions are the hazards most often associated with volcanoes, but additional hazards exist such as volcanic smog, earthquakes, and tsunamis. (Heliker, C., Stauffer, P, and Hendley, J., "Living on Active Volcanoes")

Hawaii's Kilauea Volcano is unique in its long-term (1983 – present), nearly continuous eruptive activity and has provided scientists an ideal site to develop a greater understanding of many volcanic life processes. Another unique aspect of Kilauea Volcano is its approachable lava flows. Kilauea's relatively gentle nature and convenient accessibility can be deceiving, as these characteristics do not eliminate any dangers associated with studying or viewing the volcano.

Scientists use a wide variety of instruments, sensors, methods, and techniques to monitor and study volcanic activity. In order to conduct safe and continuous monitoring,

scientists are researching sensors and systems that will allow them to remotely collect data for their studies. Remote collection not only ensures safety, but it often offers a synoptic and repetitive view of the volcanoes that may not always be possible through direct collection. Mouginis-Mark et al.'s Remote Sensing of Active Volcanism is a compilation of many scientific papers addressing a wide range of airborne and spaceborne remote sensing instruments that have been applied to aid in the study of volcanoes throughout the world. A summary of these instruments and the volcanic processes studied is found in Table 1.

Instrument	Sensor Platform	Wavelength Range	Volcanic Process Studied
Total Ozone Mapping Spectrometer (TOMS)	Spaceborne	.300 - .340 microns	Stratospheric sulfur dioxide
Advanced Very High Resolution Radiometer (AVHRR)	Spaceborne	.58 - 1.1 microns 10.3 - 12.5 microns	Daytime identification of eruption p Identification of ash clouds
Land Satellite (Landsat)	Spaceborne	.8 - 2.2 microns 10.4 - 12.4 microns	Determination of temperatures and Detection of low temperature therm
Airborne Topographic Laser Altimeter System (ATLAS)	Airborne	1.06 microns	Topographic mapping via an active
Fourier Transform Infrared Spectroscopy (FTIR)	Ground	3 - 5 microns 8 - 12.5 microns	Monitoring volcanic gas emissions Monitoring volcanic gas emissions
Geostationary Operational Environmental Satellite (GOES)	Spaceborne	3.78 - 4.03 microns	Real-time identification of hot spots
Thermal Inrared Multispectral Scanner (TIMS)	Airborne	8 - 12 microns	Retrieval of sulfur dioxide emission
High Resolution Sounder (HIRS/2)	Spaceborne	8.16 - 13.97 microns	Properties of silicate ash in clouds
Earth Resource Satellite (ERS-2), Shuttle Imaging Radar (SIR-C), and Topographic Synthetic Aperture Radar (TOPSAR)	Spaceborne	5.6 - 24 cm	Topographic mapping using radar i
ERS-2, Japanese Earth Resource Satellite (JERS-1)	Spaceborne	5.6 - 24 cm	Deformation of volcanoes using rad

Table 1. Remote Sensing Instruments Used In Volcanic Monitoring
(after Mouginis-Mark, et al., Appendix 3., p. 269)

This paper focuses on monitoring the gas emission process of Kilauea Volcano. During periods of sustained eruption, Kilauea emits about 2,000 tons of sulfur dioxide gas (SO_2) each day. There are many reasons for monitoring the amount of SO_2 emitted from Kilauea. SO_2 is a poisonous gas that can irritate human respiratory systems. It also reacts with oxygen and water in the atmosphere to produce volcanic smog (vog) and acid rain. (Sutton, et al., "Volcanic Air Pollution") In addition to better understanding the affects it may have on the health and welfare of the people of Hawaii, the SO_2 emission rate is also monitored with the belief that it can also aid in predicting periods of increasing or decreasing activity within the volcano. Sutton et al. investigate this topic in their study of the "implications for eruptive processes as indicated by sulfur dioxide emissions".

The Correlation Spectrometer (COSPEC) is the accepted and standard instrument used by HVO and volcano observatories throughout the world in monitoring volcanic SO_2 emission rates. Chapter II describes the sensor, the data collection and analysis techniques, along with a summary of data collected for Kilauea from 1979 through 1997. FLYSPEC, a miniature correlation spectrometer developed by the University of Hawaii's Hawaii Institute of Geophysics and Planetology (HIGP) is also described in Chapter II. FLYSPEC's original design applies new and current technologies to detecting SO_2 and producing emission rates in a manner similar to that of the older technologies of COSPEC. The two instruments have collected multiple data sets simultaneously. Results from these data collections are also discussed in Chapter II. COSPEC and FLYSPEC, operating in the ultraviolet (UV) range of the electromagnetic spectrum and most often employed from the ground, do have some limitations. This paper looks to imaging airborne sensors in the infrared (IR) region of the electromagnetic spectrum that may be used to augment COSPEC or FLYSPEC and fill any void that may be left by these sensors.

NASA's Thermal Infrared Multispectral Scanner (TIMS) is a long wave infrared (LWIR) imaging sensor that has collected data on Kilauea Volcano and demonstrated the ability detect the SO_2 gas and produce an SO_2 emission rate. The TIMS sensor, its data collection and analysis techniques, and a summary of the data results are discussed in Chapter III. Chapter III also briefly discusses the application of TIMS analysis techniques to data collected by the Advanced Spaceborne Thermal Emission Reflection Radiometer (ASTER). ASTER is another multispectral LWIR imager employed on the Terra Satellite as part of NASA's Earth Observing System (EOS). A third LWIR sensor, the Airborne Hyperspectral Imager, is also introduced in Chapter III. The University of Hawaii's HIGP originally designed and built (AHI) for detection of buried mines, but many additional applications are being explored. The sensor, its data collection techniques, and its current applications are disused in Chapter III.

Chapter IV explores the ability of AHI to detect SO_2 and produce an emission rate. AHI, COSPEC, and FLYSPEC collected data on the SO_2 plume of Kilauea on April 18, 2002. The site of the data collection, analysis techniques applied to AHI's data, and the results are discussed in Chapter IV. Chapter V discusses these results and provides a

conclusion on the potential use of AHI for SO_2 detection and producing SO_2 emission rates.

II. ULTRAVIOLET DETECTION OF SO_2

A. ULTRAVIOLET SESNORS

The Correlation Spectrometer (COSPEC) is the proven and trusted sensor widely used within the volcanological community for detecting and measuring SO_2 concentrations within volcanic plumes and determining SO_2 emission rates. COSPEC has been used for over 30 years, yet there has been very little advancement in its technology or data analysis methods. FLYSPEC is currently a developmental sensor using new spectrometer and computing technologies that may prove capable of detecting and measuring SO_2 concentrations and determining emission rates with the same accuracy and reliability as COSPEC, but with a much smaller system that has more processing capability and is less expensive to acquire, develop, and maintain. FLYSPEC will hopefully prove that in some cases better, faster, cheaper, and smaller is actually possible.

Both sensors operate in the ultraviolet (UV) region of the electromagnetic spectrum and use similar concepts for detection, measurement, and data processing. The following paragraphs provide an overview of the system and sensor designs, the data collection methods, and basic calculation methods used by COSPEC and FLYSPEC.

1. COSPEC

Barringer Research, Toronto, Canada, developed COSPEC primarily for environmental monitoring of SO_2 in the 1960s. Researchers first used COSPEC to monitor the SO_2 flux from volcanoes in April 1971, at Mt. Mihara in Japan. The use of COSPEC for volcanic SO_2 flux measurements spread throughout the world providing a collection of data that has been used to estimate a worldwide SO_2 flux from volcanoes, delineate the shapes and concentrations within volcanic plumes, and to determine temporal variations of SO_2 flux from volcanoes. (Tazieff and Sabroux, 1983, p. 425)

a. System Design

The COSPEC system can be described in two segments: a data collection segment and a data analysis segment. These segments are sequential, as COSPEC does not have the ability to process and analyze the data as it is collected.

(1) Data collection segment. The data collection segment is normally composed of three main components: the UV sensor, a portable computer or data logger, and an analogue paper chart recorder as illustrated in Figure 1. Solar UV

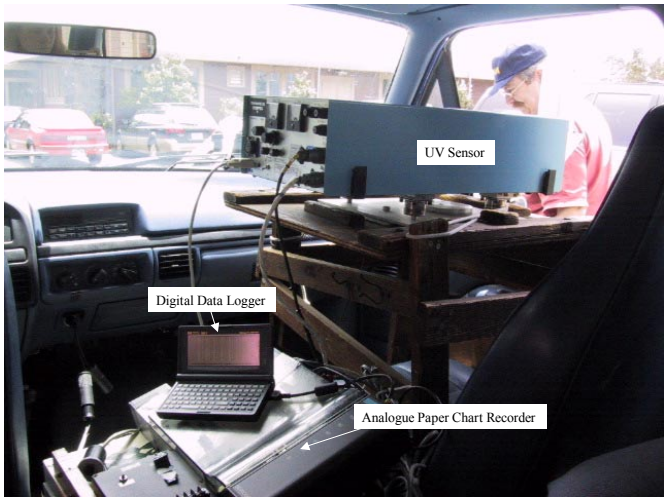

Figure 1. COSPEC System Components of Data Collection Segment

radiation passes through the UV sensor, which is connected to both the data logger and paper chart recorder. The paper chart recorder displays analog voltage recordings, which correspond to a real time SO_2 absorption profile for the area covered by the sensor. The data logger records these voltage readings in a digital format. Figure 2 summarizes the data collection segment including inputs and outputs of the system.

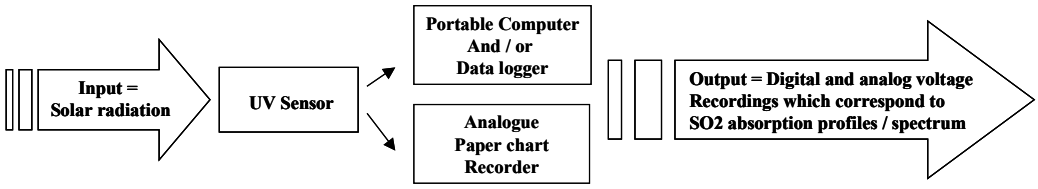

Figure 2. COSPEC System Inputs, Components, and Outputs Used for Data Collection Segment

(2) Data analysis segment. The digital voltage recordings, collected in the field, are transferred from the data logger to a desktop computer. The data processing produces an average SO_2 concentration path length with units of parts per million-meter (ppm-m). This average concentration path length is then combined with wind data (speed and direction), location data, and time to produce an average SO_2 emission rate for the day with units of tons per day (t/d). The data analysis segment and

the information it produces are illustrated in Figure 3. Details of this data processing and calculations are given in Section d.

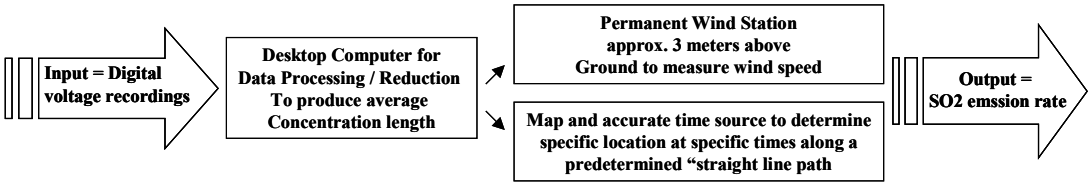

Figure 3. COSPEC System Inputs, Components, and Outputs of the Data Analysis Segment

b. Sensor Design

Resonance Inc. is the company currently manufacturing COSPEC sensors. Several physical and performance specifications for the sensor are listed in Table 2. COSPEC's sensor design is normally described in three sections: front optics, mid optics, and rear optics. (Barringer, 1976, p. 7) These sections, the components that comprise them, and the general flow of radiation through the sensor are depicted in Figure 4.

(1) Front Optics. Solar radiation is collected by the cassegrain style telescope, which has a field of view of 23 milliradians by 7 milliradians (1.3178 degrees by .401 degrees). This collected radiation passes through an entrance slit, which reduces the amount of radiation that will enter the mid optics section.

(2) Mid Optics. The radiation is directed and focused onto a diffraction grating, by a series of mirrors in the mid section of the sensor. The diffraction grating separates the radiation into individual wavelengths, and this dispersed radiation is directed toward the rear optics section.

(3) Rear Optics. In the rear section of the sensor, the radiation is focused on a correlator disc, which has arrays of circular slits etched in it correlating to positive and negative (peaks and troughs) SO_2 absorption bands. A photomultiplier tube monitors the radiation modulated by these slits. Changes in the ratio of radiation coming through the slits indicate a presence or absence of SO_2 and are proportional to the concentration of SO_2 detected. These ratio changes are reflected in the output voltages processed by the electronics and displayed in a text format on the data logger and as a real time absorption profile on the paper chart recorder. It should be noted that the units

of measure of the real time absorption profile are simply volts and require post-processing to obtain SO_2 column content.

The rear optics also includes two quartz glass calibration cells. Each cell contains a known concentration of SO_2 gas. One of the cells contains a concentration that is anticipated to be relatively higher than any actual SO_2 concentration measured, and the other cell contains a concentration that is anticipated to be relatively low in comparison to what is being measured. The calibration cells aid in determining sensor response and detecting any sensor drift that may be present. (Tazieff and Sabroux, 1983, p. 427)

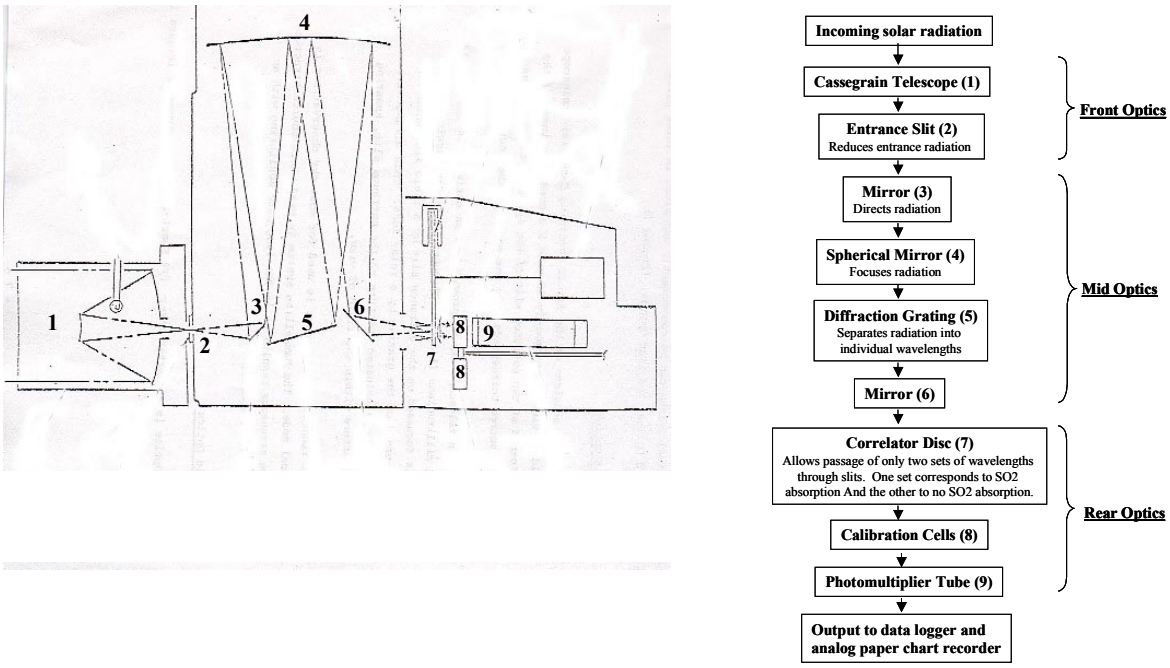

Figure 4. COSPEC Sensor Components (After Barringer, Figure 1, p. 8)

c. Data Collection Techniques

COSPEC has three standard techniques of collecting data on volcanic plumes: airborne, ground stationary, and ground mobile. Each technique has advantages and disadvantages that revolve around the location, access to, surrounding terrain, and environment of the volcano. Typical plume size, shape, and altitude also effect decisions as to which collection technique may be best. This presentation will focus on the ground mobile technique.

Using the ground mobile technique, COSPEC is typically mounted in a

vehicle as illustrated in Figure 1. The telescope is pointed out the passenger side window with a clear view of the sky directly above it. In an ideal scenario, the vehicle will be able to make several traverses under the volcano's plume on roads that are close to the vent and as perpendicular to the direction of the plume drift as possible. The traverses are normally broken down into segments along the road, which are relatively straight with uniform geometry to the plume. These road segments are manually annotated on the absorption profile generated by the paper chart recorder as the traverses are made. During data analysis, data from each of these segments is processed separately. This allows individual geometry corrections to be applied to any road segments which may not have been exactly perpendicular to the plume. Figure 5 illustrates an ideal scenario for using the ground mobile technique. (Tazieff and Sabroux, 1983, p. 433)

As Figure 5 illustrates, one traverse is typically broken into several straight-line segments. The plume will not be continuously visible for the entire traverse. The vehicle will be driving in and out of the plume. It is standard procedure to start collecting data outside of the plume under "clean air", air that is free of SO_2. At the beginning of each traverse, calibration data is collected using both the high and low calibration cells. This is accomplished by rotating the calibration cells into the sensor's field of view. It is very important to ensure the vehicle is in "clean air" as the calibration data is recorded. This is fairly easy to accomplish using the real time absorption profile generated by the analog paper chart recorder. Once the calibration data is collected, the sensor is driven through the traverse. At the end of the traverse, a collection of calibration data is repeated.

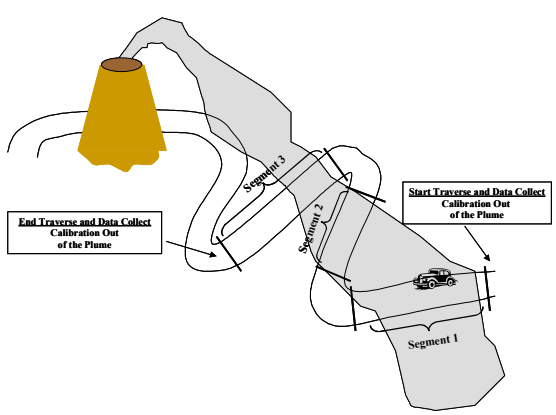

Figure 5. Ideal Scenario for Collecting Data Using the Ground Mobile Technique

The ground mobile technique works best when the plume is "on the ground", and when there is convenient road access with appropriate geometry close to the vent and plume. It is logistically easier, requires fewer people, and is less costly with respect to both money and time when compared to other techniques. (Tazieff and Sabroux, 1983, p. 433)

d. Data Analysis and Calculations

COSPEC has been monitoring volcanic SO_2 plumes for 30 years. Extensive records of SO_2 emission rates have been maintained for volcanoes throughout the world. The upkeep of these records and establishing a historical data set is an important aspect in improving the understanding of volcanic processes and their effects on the environment. In an effort to maintain consistency over time and throughout the world, two standard calculations for analysis of COSPEC data have been established to compliment the standard data collection techniques.

(1) Calculation of Average Concentration Path Length. The first calculation converts the SO_2 plume's absorption profile values, initially in units of volts, to an average concentration path length in parts per million-meter (ppm-m) for one segment of the traverse.

> One ppm-m of SO_2 is equivalent to one cubic centimeter of SO_2 gas uniformly mixed in one million cubic centimeters of air that is viewed by COSPEC over an optical path of one meter at a pressure of 101.325 kPa and a temperature of 20 degrees Celsius. (Jones and Stix, 2001, p. 44)

The following equation is used to calculate this average concentration path length per segment in ppm-m:

$$SO_{2seg} = \frac{P_{seg}}{P_{cal}} * SO_{2cal} \qquad (1.1)$$

SO_{2seg} = average concentration path length in ppm-m

SO_{2cal} = known concentration of the appropriate calibration cell in ppm-m

P_{cal} = peak height of the appropriate calibration cell in arbitrary units

P_{seg} = average segment peak height also in arbitrary units

P_{seg} must be calculated from the following equation in order to choose the appropriate values for the P_{cal} and SO_{2cal} variables in Equation 1.1:

$$P_{seg} = \frac{Segment\ \ Area}{Segment\ Width} \tag{1.2}$$

If P_{seg} is less than the low calibration peak height, then the low calibration cell values should be used for the SO_{2cal} and P_{cal} variables in equation 1.1. If P_{seg} falls between the high and low calibration heights, then an average of the two calibration cell values should be used for the SO_{2cal} and P_{cal} variables. Finally, if P_{seg} is greater than the high calibration peak height, then the high calibration cell value should be used for the SO_{2cal} and P_{cal} variables. A simulated COSPEC absorption profile is shown in Figure 6. In this figure P_{seg} is between the high and low calibration cell heights, so the average of the calibration cell values would be used for calculating Equation 1.1. (Jones and Stix, 2001, p. 45)

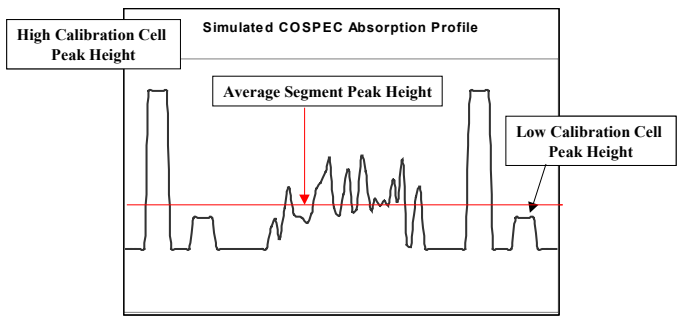

Figure 6. Simulated COSPEC Absorption Profile Illustrating Variables Used in the Concentration Path Length Calculation in Equation 1.1

(2) Calculation of Emission Rates. The second calculation determines an emission rate in tons per day (t/d) by taking the average concentration path length calculated in Equation 1.1 and combining it with wind data (speed and direction), segment length, and any angle corrections required to create a perpendicular geometry between the plume and road segment. An emission rate is calculated for each segment. These values are then summed to determine the total SO_2 emission rate for a given traverse. The SO_2 emission rate calculation for each segment is shown in Equation 1.3. (Jones and Stix, 2001, p. 44)

$$E_{seg} = SO_{2seg} * \cos\Theta * dl * v_{wind} * C_F \tag{1.3}$$

E = SO_2 emission rate per segment in tons per day (t/d)

SO_{2seg} = average concentration path length per segment in ppm-m

$\cos\Theta$ = angle correction required to create perpendicular geometry between the

plume and road segment

dl = length of a segment in meters determined from a map

v_{wind} = average wind speed in m/s determined by wind station or other means

C_F = conversion factor to convert from ppm-m^3/s to metric tons per day (t/d)

Equation 1.4 calculates the conversion factor:

$$C_F = 2.8579 * .001 * 10^{-6} * 86400 * 273/293 = .00023008194 \quad (1.4)$$

2.8579 = density of SO_2 gas in kg/m^3 at standard temperature (0 degrees Celsius) and pressure (101.325 kPa)

.001 = conversion of kg to g

10^{-6} = conversion of g to tons

86400 = conversion of seconds to days

273/279 = converts SO_2 gas density from standard temperature (0 degrees Celsius) to 20 degrees Celsius

These collection techniques and analysis methods have faithfully generated trusted data calculations for three decades; however, this does not mean COSPEC is a perfect system. As with many systems, advancements in technology create opportunities for improvements that should not be overlooked.

2. FLYSPEC

Keith Horton, Assistant Researcher at the Hawaii Institute of Geophysics and Planetology, is currently developing a sensor referred to as FLYSPEC (a name given to emphasize its size in comparison to COSPEC). FLYSPEC is essentially a miniature COSPEC that takes advantage of new spectrometer and computing technology. The new technology reduces the size and cost of the system, in addition to reducing the amount of time required to manually analyze the data. More importantly, the new technology offers real time data analysis capability with spectral fitting algorithms that could prove to provide more accurate results.

a. System Design

As FLYSPEC is a developmental sensor, no formal literature is currently published. For comparison purposes, the FLYSPEC system can be described in the same two segments as COSPEC: a data collection segment and a data analysis segment. With FLYSPEC these segments are not strictly sequential. The data collection segment *does*

perform some data processing and produces real time data that can be read in ppm. This difference is explained in further detail in the following paragraphs.

(1) Data Collection Segment. FLYSPEC's data collection segment is composed of three main components: the UV sensor, a portable computer, and a Global Positioning System (GPS). These three components are pictured in Figure 7. Solar UV radiation passes through the UV sensor which is connected to the portable

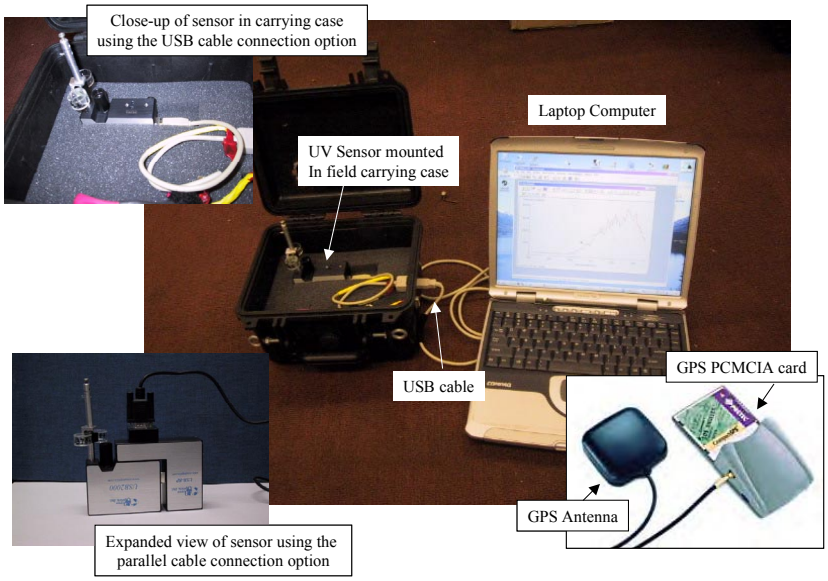

Figure 7. FLYSPEC System Components Used in the Data Collection Segment

computer via either a USB or a parallel port cable. The portable computer displays the real time UV spectrum seen by the sensor along with a real time SO_2 absorption profile for the area covered by the sensor. To accompany these visual displays, the portable computer also calculates and stores values for concentration path length with units of ppm-m which correspond to the real time displayed SO_2 absorption spectrum. Concurrently, the GPS collects position information and the computer stores these values in a file with the average concentration path length. This automated calculation of concentration path length significantly reduces the amount of time required and chance for inconsistencies in the data analysis segment. The information provided by GPS can be used to calculate the straight-line segments of the traverse without requiring a map. Figure 8 summarizes FLYSPEC's Data Collection segment in terms of system inputs, components, and outputs.

(2) Data Analysis Segment. With the average concentration path length and straight-line segments determined in the data collection segment, wind

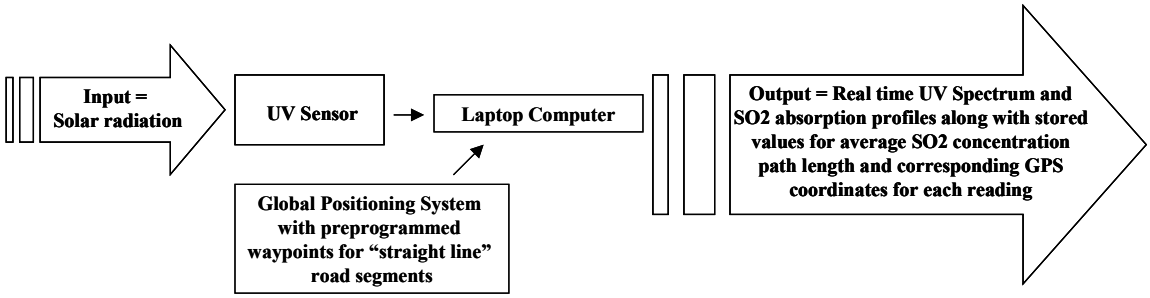

Figure 8. FLYSPEC System Inputs, Components, and Outputs Used in the Data Collection Segment

speed data is the only other variable needed to produce the average SO_2 emission rate with units of tons per day. The wind speed data is collected separately and then combined with the average concentration path length to produce the emission rate. Figure 9 illustrates the Data Analysis Segment in terms of system inputs, components, and outputs. The calculations required in the data collection and data analysis segments are discussed in further detail in Section d.

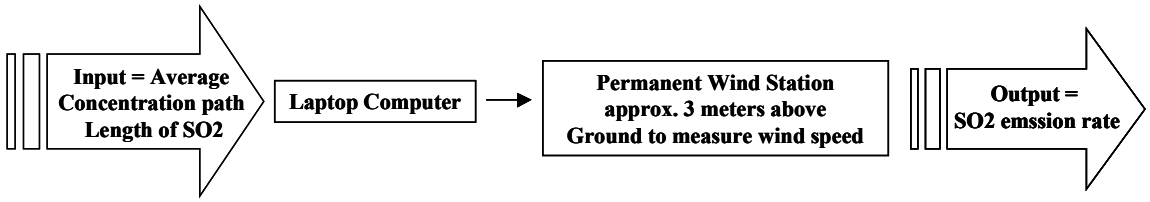

Figure 9. FLYSPEC System Inputs, Components, and Outputs Used in the Data Analysis Segment

b. Sensor Design

FLYSPEC's UV sensor is the USB2000 Miniature Fiber Optic Spectrometer developed by Ocean Optics, Inc, Dunedin, Florida. The company started in 1989 when researchers in Florida developed a fiber optic pH sensor as part of an instrument designed to study the ocean's role in global warming. As part of the sensor design, they wanted to place a spectrometer on a buoy. At the time, there were no spectrometers small enough to do this, so they developed their own. The end product was a fiber optic spectrometer nearly a thousand times smaller and ten times less expensive than existing systems. (Ocean Optics, p.1) The USB2000 is the second generation of these miniature spectrometers. Several physical and performance

specifications for the sensor are listed in Table 2. For comparison purposes, the following paragraphs will describe the sensor in the same three sections as were used with COSPEC: front optics, mid optics, and rear optics. Figure 10 displays the sensor components divided into these sections.

(1) Front Optics. Solar radiation is collected through a filter lens that is built into the sensor's carrying case. This filter aids in reducing the amount of stray light reaching the spectrometer. Normally, the radiation will then be collected with the sensor's small telescope with a focal length of 42 mm. However, during calibration, the radiation will pass through the calibration cells before entering the telescope. FLYSPEC has a high and low calibration cell. The glass quartz cells have slightly different known concentrations than the cells used in COSPEC, but the same company manufactures them. To perform calibrations, the calibration cells are rotated into the path of the radiation in the same way demonstrated by COSPEC. The cells are mounted to the

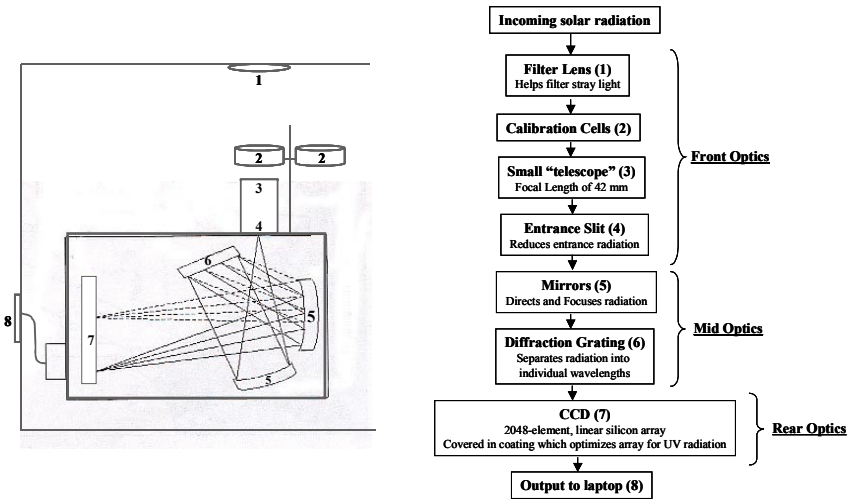

Figure 10. FLYSPEC Sensor Components (After Bo Galle, Figure 5, p.40)

outside of the spectrometer and are rotated above the telescope as illustrated in Figure 11. Once the radiation has passed through the calibration cells and telescope, it passes through an entrance slit into the mid optics section.

(2) Mid Optics. The radiation is directed and focused onto a diffraction grating that disperses the radiation and directs it to the rear optics. The components and functions of this section are very similar to COSPEC, but they operate on a much smaller scale.

(3) Rear Optics. The dispersed radiation is focused onto a

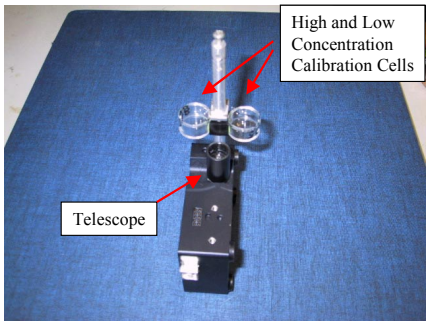

Figure 11. FLYSPEC Telescope and Calibration Cells

2048-element charge coupled device (CCD). The CCD is a linear silicon array. It is covered in a coating that optimizes the CCD for detection of UV radiation. The CCD detects UV radiation and forms a spectrum that ranges from 177 – 333 nm. This entire spectrum is transferred to the portable computer. This is a significant difference from the data that COSPEC produces which corresponds to a limited number of specific wavelengths in the UV spectrum. A software program has been developed to display this detected UV spectrum, calculate and display a corresponding SO_2 absorption spectrum, and maintain a log of concentration path length values in ppm-m along with the corresponding GPS location recordings at a rate of 1 Hz.

The following table presents a summary of physical and

Physical Specifications	**FLYSPEC**	**COSPEC**
Dimensions (LWH in inches)	3.5 x 2.5 x 1.31	31 x 14.74 x 8.75
Weight	.6 lb with cable	42.5 lbs
Power	.5 W	8 W @ 12VDC
Operating Temp Range (Celcius)	10 - 50	0 - 50
Detector Specifications		
Detector Type	2048-element Linear Silcon CCD array	Photomultiplier Tube
CCD element size (microns)	12.5 x 200	N/A
Effective Range (nm)	177 - 333	280 - 320
Optics Specifications		
Grating	2400 lines	1200 l/mm, plane, 68 x 54 mm
Slit (WH in microns)	25 x 1000	.25 x 5.8
Focal Length	42 mm (input) 68 mm (output)	25 cm
Optical Resolution (nm)	~.25	0.4
Pixel Resolution (nm)	~.1	N/A
Stray light	< 0.10% at 250 nm	N/A
Performance Specifications		
A/D resolution	12-bit	12-bit
A/D sampling frequency	1 Hz - 1 KHz	1 Hz (max)
Integration Time	3 milliseconds to 60 seconds	1 second - 32 seconds
Field of View (degrees)	10	1.3178 x .401
Sensitivity	86 photons/count or 2.9*10^-17 watts/count	2.8 millivolts/ppm.m (typical low range)
Signal to Noise Ratio	250 : 1 -- single acquistion at full signal	N/A
SO2 Detection Limit (low range)	9 - 13 ppm.m	< 5 ppm.m

Table 2. Physical and Performance Specifications of the COSPEC and FLYSPEC sensors

performance specifications for the sensors on both COSPEC and FLYSPEC. There are several differences between the sensors, but some of the key differences are at the system level. The new spectrometer technology has offered solid improvements to SO_2 detection, but it is the *combination* of new spectrometer technology and new computing technology that may allow FLYSPEC to prove the ability collect and process data more efficiently, consistently, and effectively than COSPEC.

c. Data Collection Methods and Techniques

FLYSPEC hopes to prove capable of collecting data using all three techniques demonstrated with COSPEC. To date, FLYSPEC has only demonstrated collection of data using the same ground mobile technique. FLYSPEC performs the ground mobile technique using a similar method to COSPEC; however, there are a few differences. Due to FLYSPEC's smaller size, it is mounted to the top of the vehicle, either on the hood or on the roof, so that it can point directly up at the sky. FLYSPEC has made several traverses collecting data concurrently with COSPEC in this manner (see Figure 12).

At the beginning of a traverse, while the sensor is under "clean air", FLYSPEC collects several frames of data on each of its calibration cells just as COSPEC does. In addition to the calibration data, FLYSPEC also collects data on a dark frame and a reference frame. A dark frame is created by simply covering the lens of the carrying case so that no radiation can enter the sensor. A reference frame is created by looking straight up at "clean air". All of this initial data collected prior to the start of the traverse plays a very important role in the data analysis and calculations. Following these initial measurements, a traverse is made. Calibration, dark, and reference data is occasionally collected at the end of a traverse; however this is not required.

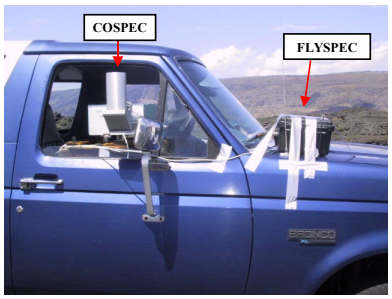

Figure 12. Concurrent Data Collection with COSPEC and FLYSPEC Using the Ground Mobile Technique

d. Data Analysis and Calculations

Although the data collection methods and techniques of COSPEC and FLYSPEC are nearly identical, the differences in the technology of the sensors translate to slightly different data analysis and calculations. FLYSPEC calculates a real time SO_2 absorption profile from data collected over a range of wavelengths using Equation 1.5. The calculation uses real time sample data, reference frame data, and dark frame data over the range of UV wavelengths to produce an absorption profile.

$$A_\lambda = -\log_{10}\left(\frac{S_\lambda - D_\lambda}{R_\lambda - D_\lambda}\right) \tag{1.5}$$

A_λ = Absorbance at some wavelength (unitless)

S_λ = Sample intensity at some wavelength

D_λ = Dark intensity at some wavelength

R_λ = Reference intensity at some wavelength

Figure 13 shows a UV absorption spectrum for a laboratory sample of SO_2 with several

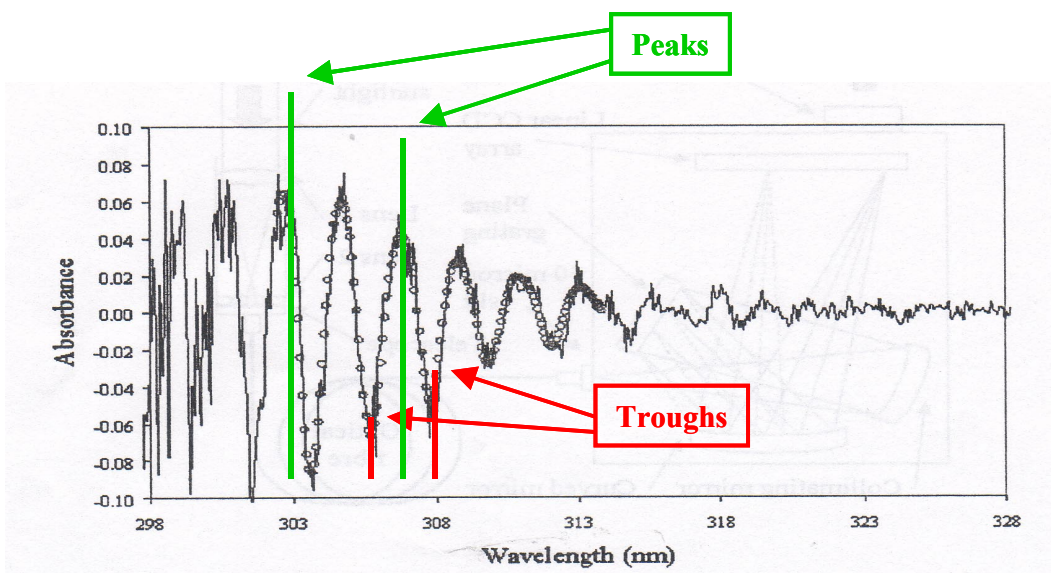

Figure 13. SO_2 Absorption Spectrum in UV Spectral Region (After Galle, Figure 2., p.17)

peaks and troughs annotated. Most of the strong SO_2 absorption peaks and troughs are located between 300 and 310 nm. Although FLYSPEC collects over the much broader range of 177 – 333 nm, many of the figures illustrating FLYSPEC data will be truncated to a more limited range of 300 – 310 nm in order to highlight these stronger absorption features of SO_2.

Figure 14 displays sample data from one of FLYSPEC's traverses on

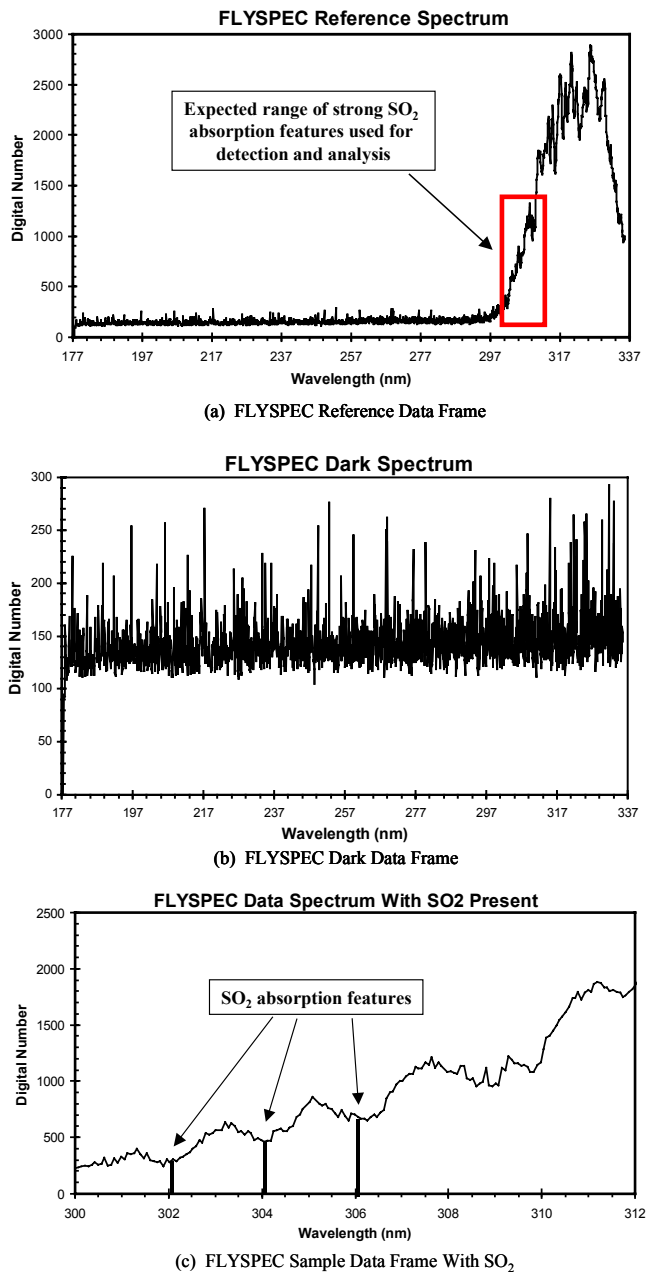

Figure 14. Example Reference, Dark, and Sample Data frames collected by FLYSPEC during traverse on Kilauea Volcano, Hawaii on March 4, 2002

Kilauea Volcano, Hawaii on March 4, 2002. Sample (a) illustrates a reference data frame during the traverse to produce real time absorbance spectra. Sample (c) illustrates a data frame in the middle of the traverse in which SO_2 is present. Although the absorbance spectra are calculated and displayed real time on the portable computer, these spectra are

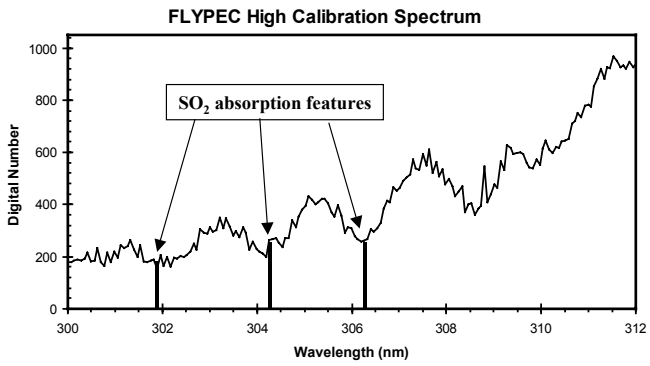

(a) FLYSPEC's High Calibration Cell Spectrum

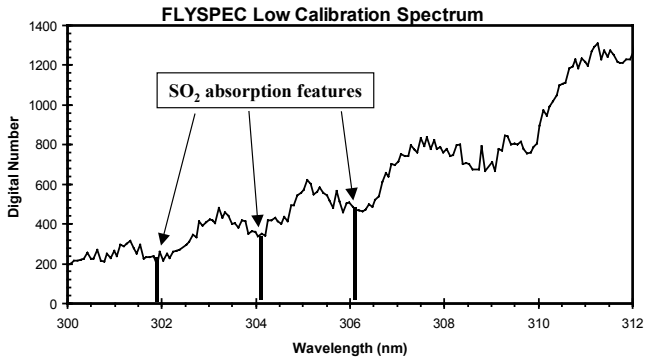

(b) FLYSPEC's Low Calibration Cell Spectrum

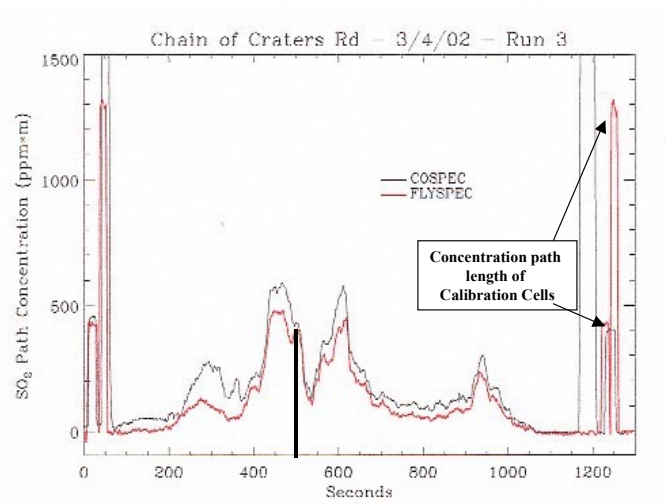

(c) FLYSPEC's Concentration Path Length Vs Traverse Time

Figure 15. FLYSPEC's Calibration Cell Spectrum and Concentration Path Length Plot for a March 4, 2002, Traverse On Kilauea Volcano, Hawaii

not stored but simply used as data in the next step of calculating the concentration path length. These absorbance spectra are fitted using a non-linear quadratic to a laboratory SO_2 spectrum generated by the calibration cells. High and low calibration data collected during this March 4th traverse are displayed in Figure 15 as samples (a) and (b) respectively. This spectral fitting results in the average concentration path length of the observed plume in ppm-m. These calculations are performed at a rate of 1 Hz. The results are values of concentration path length over the time of the traverse. The concentration path length plot representing the March 4th traverse is also included in Figure 15. The point highlighted on the concentration path length plot corresponds to the absorbance calculated using the data frame in Figure 14, sample (c). In addition to the complete spectrum calculations, FLYSPEC can also be programmed to perform and store these same calculations at specific wavelengths. This is similar to what COSPEC does with the slits in its correlation disc; however, FLYSPEC's peaks and troughs are not limited by a specific number of physical slits and can be easily changed through the computer's custom built software.

The concentration path length results are recorded along with corresponding GPS coordinates and are stored in a text format on the portable computer. All of these calculations are performed real time during the data collection. A sample of the typical FLYSPEC data text format is show in Figure 16. The time is Hawaii Standard Time.

Data Point	Year	Month	Day	Hour	Minute	Second	Latitude	Longitude	Elevation	Raw SO2	Smooth SO2
0	2002	4	18	9	58	54	1924.1201 N	15515.9316 W	1131.4	5.93	5.93
1	2002	4	18	9	58	55	1924.1201 N	15515.9316 W	1131.5	5.8	5.8
2	2002	4	18	9	58	56	1924.1202 N	15515.9316 W	1131.5	5.2	3.03
3	2002	4	18	9	58	57	1924.1202 N	15515.9316 W	1131.5	-1.89	-0.65
4	2002	4	18	9	58	58	1924.1202 N	15515.9316 W	1131.5	-5.25	-5.15
5	2002	4	18	9	58	59	1924.1202 N	15515.9316 W	1131.5	-8.31	-4.06

Figure 16. FYSPEC Data Text Format Stored During Data Collection

The latitude and logitude readings are in degrees and decimal minutes. The elevation readings are in meters. The raw and 3-point smooth readings of SO_2 concentration path length are in ppm-m.

Following the data collection, FLYSPEC uses the same equation as COSPEC (Equation 1.3) to generate an emission rate in tons per day. The stored average concentration path length is combined with corresponding wind data and segment length

data. The wind data (speed and direction) is obtained from a ground station near the volcano's vent. The segment length can be derived from the GPS data; however, the computer program is not fully developed yet and does not use the GPS data in this way. Currently a map is being used to generate the segment length which is the same method used in analyzing COSPEC's data.

These data collection and analysis methods are still under development. Several traverses have been made concurrently with COSPEC in order to validate the sensor and calculations. Figure 15 (c) is one of several comparisons that have been made between COSPEC and FLYSPEC data up to this date. In general, the results have been very similar and promising. There are a few minor differences that have not yet been fully explained. Some of differences are believed to stem from the substantial physical difference that exists between the fields of view of the two sensors. The variances in the results may actually correspond to the fact that each sensor is physically "seeing" a different "piece of sky". Both sensors are also sensitive to different sun angles and cloud cover, and their degrees of sensitivity to these issues may be the cause of the different variances in the results. Additional tests and concurrent traverses with COSPEC will help eliminate many of these questions.

B. SULFUR DIOXIDE EMISSION RATES OF KILAUEA VOLCANO, HAWAII, USING UV SENSORS

Kilauea's long-term activity has made it an ideal volcano for many different studies. Located in Hawaii, Kilauea currently hosts the longest running SO_2 emission-rate data set on the planet. (Sutton, Elias, Gerlach, and Stokes, 2001, p. 283) Stoiber and Malone first used COSPEC to measure Kilauea's SO_2 emission rates in 1975. A program of nearly weekly SO_2 emission rates was started in 1979 and has continued through the present. (Casadvevall and others, 1987; Greenland and others, 1985; Elias and others, 1993; Elias and Sutton, 1996). The US Geological Survey's Hawaiian Volcano Observatory (HVO) has served as a headquarters for this SO_2 monitoring, and has published a compilation of COSPEC measured SO_2 emission rates covering the period from 1979 through 1997. Much of HVO's staff and volunteers have participated in the monitoring program consisting of approximately 1100 days of measurements including

more than 5,000 plume traverses over the 19-year period. (Elias, Sutton, Stokes, Casadevall, 1998, p.3)

Initially, in 1979, Kilauea's main area of SO_2 release was its summit caldera. In 1983, an eruption began along the East Rift Zone (ERZ) initiating an additional significant area of release at the Pu'u'O'o vent. Currently, these two areas are the main focus for SO_2 emission rate measurements. Measurements have been made in both of these areas using all three methods available to COSPEC; however, only the vehicle based traverse method results will be discussed, as this is the method of focus for this paper.

Figure 17 illustrates the two main areas of SO_2 release on Kilauea. Measurements of SO_2 emission from the summit caldera are typically made along a section of Crater Rim Drive which encircles the caldera. This section of road is highlighted in Figure 17. Typically brisk northeasterly trade winds (3-12 m/s from 0 to 45 degrees east) create a plume of SO_2 that drifts approximately 1 km from its Halemaumau and solfatara source across Crater Rim Drive. Under ideal wind conditions, the plume will be dense, compact, and measurable close to the source. Daily emission rates are typically calculated from an average of data collected over six or more ten-minute plume traverses in the summit caldera area.

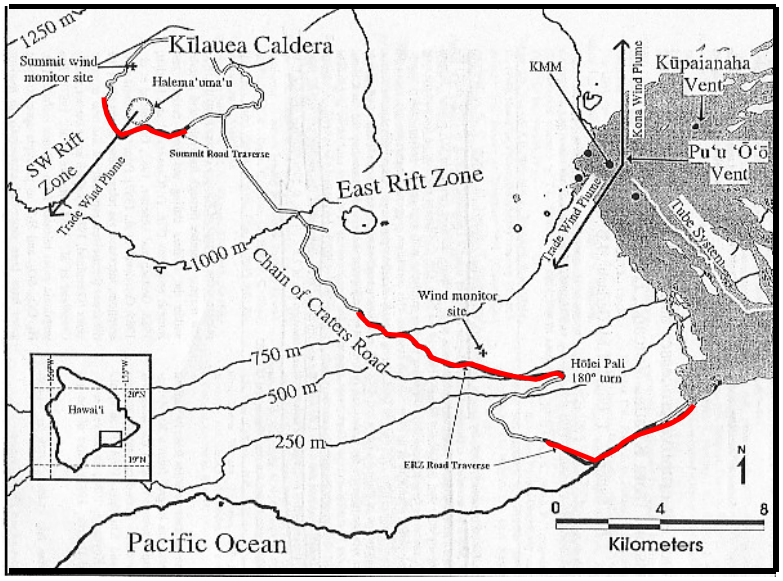

Figure 17. Typical Routes for Vehicle-Based Traverses of Kilauea Caldera and East Rift Zone (After Sutton et al., Figure 1., p.284)

At this point it is important to note that wind speed is normally one of the largest sources of error in the data analysis. Several different methods have been used to measure wind speed over this extensive data collection period. Experiments have determined that wind measurements collected from 3 meters above the ground at a site next to HVO most accurately reflect the plume speed in the caldera region. As of 1998, wind speed measurements are made at a station 3 meters above ground at HVO. This station is labeled as the summit wind monitor site in Figure 17. Data collected in the past have been adjusted by up to 20% in some instances in order to normalize the variances that are believed to have been caused by the different wind collection methods. With the appropriate wind adjustments, Figure 18 displays SO_2 emission rates calculated for the Kilauea caldera area from June 1979 through 1997. The units of emission rates are metric tons per day (mt/d). An increase in emission rates begins with the eruption of Pu'u'O'o in 1983. A continuous decline is seen from 1987 through 1997.

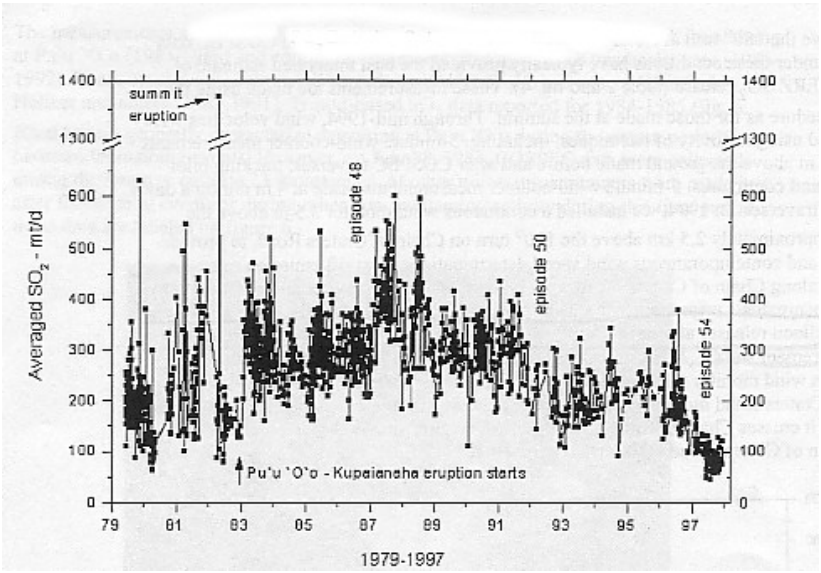

Figure 18. Long Term Data Set Of Emission Rates Determined By COSPEC For The Kilauea Summit Caldera Area (From Elias et al., Figure 3., p.5)

SO_2 measurements collected along sections of Chain of Craters road were initiated in 1992 in order to better account for the emission rate of Pu'u'O'o. These sections are also highlighted in Figure 17. Ideal wind conditions for these measurements consist of speeds greater than 5 m/s and directions between 25 and 40 degrees east. These conditions will normally create a compact plume approximately 9 km downwind

of the Pu'u'O'o vent which crosses the Chain of Craters Road above the 180-degree turn at the Holei Pali annotated in Figure 17. Daily emission rates for these sections are also calculated from an average of data collected over several plume traverses.

HVO performed multiple experiments to determine the best method for collecting wind data in the Chain of Craters Road area. It was determined the winds measured near the center of the traverse and a good distance above the ground provided the best measurements. Currently, HVO uses a continuous wind monitor 3.5 m above the ground near the 180-degree turn at Holei Pali. This wind monitor site is also labeled in Figure 17. Figure 18 displays emission rates calculated for the Chain of Craters Road section from 1992 through 1997. The black vertical bars represent the standard deviation of all traverses on a single day. The units for average daily emission rates are mt/d. (Sutton, Elias, Gerlach, and Stokes, 2001, p. 285-286)

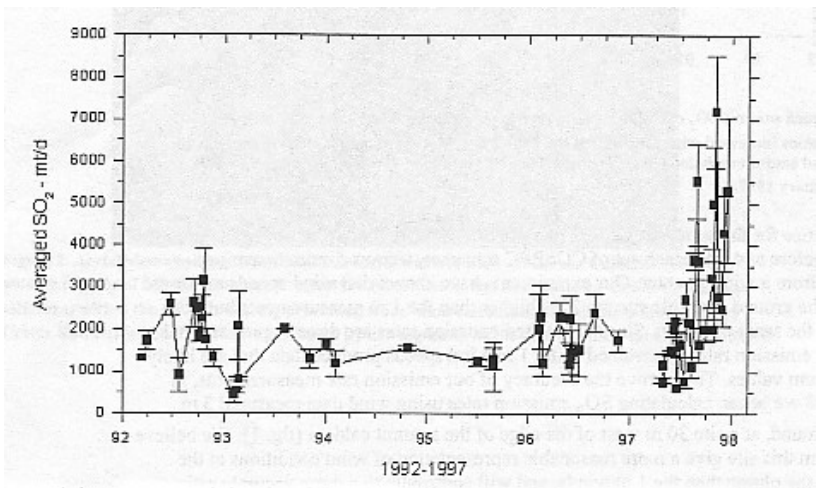

Figure 19. Long Term Data Set Of Emission Rates Determined By COSPEC For The Chain of Craters Road Area (From Elias et al., Figure 4., p.6)

C. SUMMARY OF UV DETECTION

There are advantages and disadvantages in using COSPEC and FLYSPEC to monitor volcanic SO_2 emission rates. Both of the sensors operate using scattered skylight, which allows for simplistic and versatile collection methods and techniques for the sensors. Neither sensor requires a specialist operator or subsequent spectral analysis because the fit to the SO_2 spectrum is achieved with the calibration cells. The main disadvantage is that the emission rates are subject to large errors due to uncertainty in the

plume velocity. The speed of the plume is often assumed to be equal to wind-speed measurements obtained close to the ground. These wind speeds near the ground are not always accurate for the plume. (McGonigle and Oppenheimer, 2002, pp. 4-5)

The concepts used for the data collection and analysis are very similar for COSPEC and FLYSPEC; however, the advantages offered by the new technologies used in FLYSPEC should not be overlooked. The most obvious advantage is in the physical size of the sensor. COSPEC is roughly the size and weight of a 40-pound sack of potatoes, whereas FLYSPEC is roughly the size and weight of a deck of cards. Some volcanic plumes are accessible only on foot. Having a sensor the size of FLYSPEC to complete this form of data collection and analysis would greatly simplify the process. FLYSPEC is also less expensive which could facilitate the ability of researchers to obtain multiple sensors. COSPEC collects data corresponding to a limited number of specific wavelengths within the UV spectrum, whereas FLYSPEC collects data over an entire band of the UV spectrum. This range of data combined with the spectral fitting algorithm could prove to provide a more accurate and consistent means of analyzing data. The addition of the new computing power to the system makes this analysis possible in real-time. The lower cost, ability to have multiple sensors, automatic analysis, and data storage capability could facilitate putting several FLYSPECs at a remote site to collect SO_2 plume samples over several days at the same spot. These are significant advantages which will hopefully be proven over time and provide researchers a better, faster, cheaper, and smaller means of detecting and analyzing volcanic SO_2 emission rates.

III. INFRARED DETECTION OF SO_2

A. AIRBORNE AND SPACEBORNE INFRARED SENSORS

Although COSPEC has set the precedence for detecting and measuring concentrations of SO_2 within volcanic plumes, its various data collection and analysis techniques do have some inherent limitations. Most of these limitations originate in the geographic locations of the various volcanoes, in the volcanoes' natural and man-made surroundings, or in the standard meteorological conditions of the area, rather than in the COSPEC system or sensor. For example, if typical wind conditions do not generate a plume drift with appropriate geometries to an existing road system, COSPEC's ground mobile collection technique could become difficult and produce less accurate results. COSPEC's airborne collection technique requires the sensor to be flown beneath the plume, and if the plume consistently drifts near the ground, an aircraft may not be able to achieve an altitude low enough to allow COSPEC to collect data. Solutions to these limitations could be developed through new data collection and analysis techniques; however, they may also be discovered in the application of sensors operating in a different region of the electromagnetic spectrum, such as thermal infrared sensors.

Collecting data in a different region of the electromagnetic spectrum not only implies different data collection and analysis techniques, but it also generates the possibility of seeing new characteristics in the data. In addition to measuring the plume's SO_2 concentration, the transition to the thermal infrared region gives the sensor the ability to collect information on thermal aspects of the volcano. Several airborne and spaceborne infrared sensors have recently been used to explore some of these capabilities.

NASA has used its airborne Thermal Infrared Multispectral Scanner (TIMS) to develop data analysis techniques and potential algorithms to map volcanic plumes and to determine a plume's SO_2 concentration and emission rate. TIMS has also been used to map temperature and emissivity of volcanic lava surface flow fields. These studies with TIMS laid initial groundwork that is being further developed for use with the Advanced

Spaceborne Thermal Emission and Reflection Radiometer (ASTER), a sensor currently flown on a Terra Satellite that is part of NASA's Earth Observing System (EOS).

The Airborne Hyperspectral Imager (AHI), owned by the University of Hawaii, is another thermal infrared (TIR) sensor that can be used to monitor volcanic activity. This paper explores AHI's ability to detect volcanic plumes and determine a plume's SO_2 concentration. The following paragraphs provide an overview of the TIMS sensor, its data analysis techniques, and some of its published results. ASTER and its potential to use the TIMS analysis techniques are also discussed. Finally, a description of AHI's system and sensor design, along with its data collection techniques is presented.

1. Thermal Infrared Multispectral Scanner (TIMS)

TIMS is an airborne long wave infrared (LWIR) sensor developed by NASA Stennis Space Center, the Jet Propulsion Laboratory (JPL), and Daedalus Corporation. TIMS has demonstrated abilities in a variety of applications from ground temperature mapping and mineral classification to detecting volcanic plumes and determining SO_2 concentrations. In addition to performing its airborne remote sensing mission, TIMS has also served as a simulator for ASTER, a spaceborne IR sensor. A brief overview of the sensor follows, as well as a description of data analysis techniques that allow the sensor to detect and quantify volcanic SO_2 plumes.

a. Sensor Design and Data Collection

TIMS is a multispectral LWIR sensor with a six-element HgCdTe array. This array is sensitive to an LWIR band ranging from 8.2 to 12.2 microns. A dispersive grating spreads this LWIR band over the six pixels so that each pixel is sensitive to a smaller segment of the broad LWIR region. (Baer-Riedhart, "TIMS")

TIMS operates from several different aircraft: C-130, ER-2, Stennis Learjet, and DOE Cessna Citation aircraft. It operates in a scanning mode and scans the array over a 76.56 degree FOV collecting data for 638 points on the ground per scan line. It has a variable scan rate from 7.3 to 25 scans per second. (Hydrology Data Support Team, "Performance Parameters") The multispectral image cube that is produced consists of 638 pixels along the x-axis, a number of pixels in the y-axis that are determined by the number of scan lines collected along the flight line, and six x-y planes

along the z-axis that each represent one of the smaller segments of the 8.2 – 12.2 wavelength region. Figure 20 illustrates the scanning collection mode. Often in a

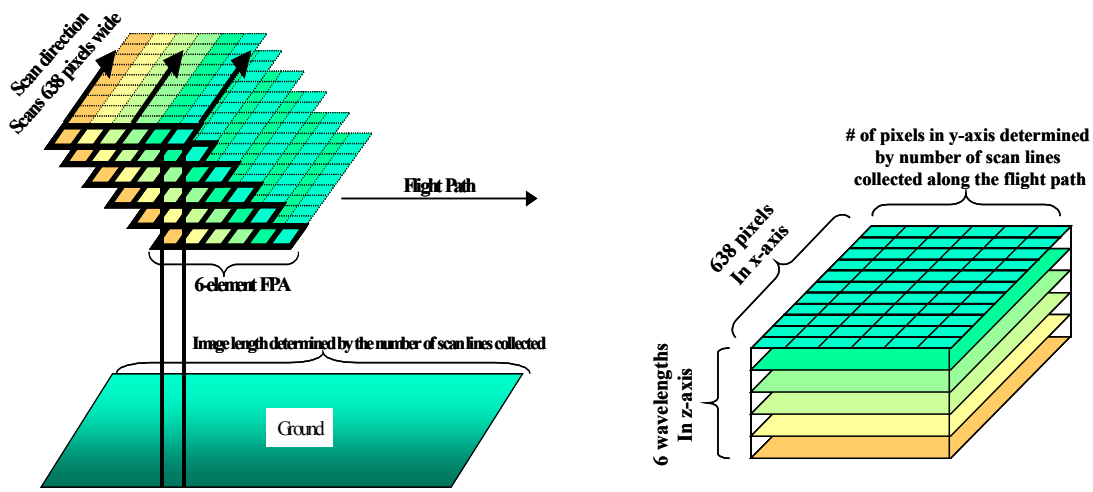

Figure 20. Scanning Multispectral Data Collection And Resulting Data Cube

scanning mode the array is stationary, and some form of rotating mirror performs the actual scanning motion; however, the figure depicts TIMS' six-element array performing the scanning motion. This was done in order to clearly illustrate the relationship between the scanning array and resulting multispectral data cube.

Detector Specifications

Imager	6 element HgCdTe FPA
Spectral Coverage (microns)	8.2 - 12.2
Number of Spectral Bands	6

Optics Specifications

Spectral Resolution	700 nm
Angular Resolution (mrad)	2.5
Ground Resolution (m)	50 at 65,000 ft altitude
Aperture (in)	7.5

Performance Specifications

Quantization	8 bits
Pixels per scan line	638
Scan Rate (scans/second)	varable: 7.3, 8.7, 12, 25
Software	Data can be read with any standard image processing package, e.g. PCI, ERDAS, IDL etc.
File Size	4 - 9 MB
Set Size	~2.5 GB
FOV (full / angular)	76.5 degrees
Swath Width (km)	31.3
Guidance Sensor	roll corrections of + / - 15 degrees
Operating Alitudes (km)	1 - 20
NEDT	< .4 K

Table 3. TIMS Sensor Specifications

The sensor has a Noise Equivalent Delta Temperature (NEDT) of less than 0.4 degrees K. Two on-board black bodies perform calibration for the sensor. High and low temperatures are chosen for these black bodies based upon the temperatures expected to be imaged in a particular scene. Data is collected on these black bodies at the beginning and end of each scan line. Additional sensor specifications are included in Table 3. (Baer-Riedhart, "Sensor/Aircraft Parameters")

b. Data Analysis Techniques

As seen with FLYSPEC, data analysis of SO_2 plume concentrations using ultraviolet wavelengths is based on an absorbance profile calculation over a straight-line distance transecting the plume. These results are fitted to a known laboratory SO_2 concentration absorbance profile. The data is collected looking up at the sky, providing a fairly constant background to measure against, with the main exception being cloud cover. Data analysis of SO_2 plume concentrations using thermal infrared wavelengths is slightly more complicated than using ultraviolet wavelengths. Calculations are based on a form of the radiative transfer equation. Using TIMS or AHI, the data is collected looking down at the ground, possibly resulting in measurements against a highly varied background.

(1) Estimating SO_2 Concentration. Realmuto et al. (1994) introduced a procedure for estimating the SO_2 content of volcanic plumes using data collected by TIMS. This procedure models the radiance observed by TIMS as it looks to the ground through an SO_2 plume using the MODTRAN radiative transfer code (Berk et al., 1989).

> MODTRAN calculates atmospheric transmission and radiance using models of the absorption bands of 12 gas molecules (H_2O, CO_2, O_3, N_2O, CO, CH_4, O_2, NO, SO_2, NO_2, NH_3 and HNO_3), utilizing three-parameter band models with spectral resolutions of 1 cm^{-1}. Realmuto et al., 1997, p.15059)

Equation 3.1 is the basic radiance equation used in the code. It is a simplified version of the equation, as it does not account for any viewing angles other than nadir.

$$L_s(\lambda, T_0) = \{\varepsilon(\lambda)B(\lambda, T_0) + [1 - \varepsilon(\lambda)]L_d(\lambda)\}\tau(\lambda) + L_u(\lambda) \qquad (3.1)$$

$L_s(\lambda, T_0)$ = Radiance of the ground as it is viewed through the atmosphere as a function of wavelength (λ) and ground temperature (T_0)

$\varepsilon(\lambda)$ = Ground emissivity as a function of wavelength

$B(\lambda, T_0)$ = Planck function in terms of wavelength and ground temperature

$L_d(\lambda)$ = Ambient or sky radiance at ground altitude as a function of wavelength

$\tau(\lambda)$ = Spectral transmittance of the atmosphere as a function of wavelength

$L_u(\lambda)$ = Ambient or sky radiance at instrument or sensor altitude as a function of wavelength

Table 4 lists inputs and their sources that are required to run the MODTRAN code. With these inputs, the model calculates values for L_s, L_d, L_u, and τ. Figure 11 illustrates two example atmospheric transmission profiles generated by MODTRAN. The dashed line represents a transmission profile through an atmosphere that is free of SO_2 whereas the solid line represents a transmission profile through an atmosphere that contains SO_2. A typical SO_2 plume is cooler than the ground so it will absorb the ground radiance making

Input Parameter	Source
Ground emissivity	Estimate from TIMS radiance measurements of ground that is not beneath the plume
Ground altitude	DEM or other mapping product
TIMS or sensor Altitude	Aircraft measurements
Zenith angle	Path between sensor and ground determined by aircraft measurements
Barometric pressure	Meteorlogical measurement or packaged LOWTRAN atmospheric model
Temperature	Meteorlogical measurement or packaged LOWTRAN atmospheric model
Humidity	Meteorlogical measurement or packaged LOWTRAN atmospheric model

Table 4. MODTRAN's Required Inputs And Respective Sources

it an identifiable feature in the TIMS ground radiance profiles. This is illustrated by comparing the dashed line profile (0 gm^{-2} of SO_2) and the solid line profile (23 gm^{-2} of SO_2) in Figure 21.

Indicated by shaded regions, Figure 21 also illustrates the normalized spectral responses for the six TIMS channels operating in a typical atmosphere free of SO_2. The figure illustrates that if there is SO_2 in the atmosphere, the strongest response is featured in TIMS' channel 2. Having the strong absorption response in one channel generates opportunities to expose the feature through applying different processing techniques that enhance or emphasize that particular channel.

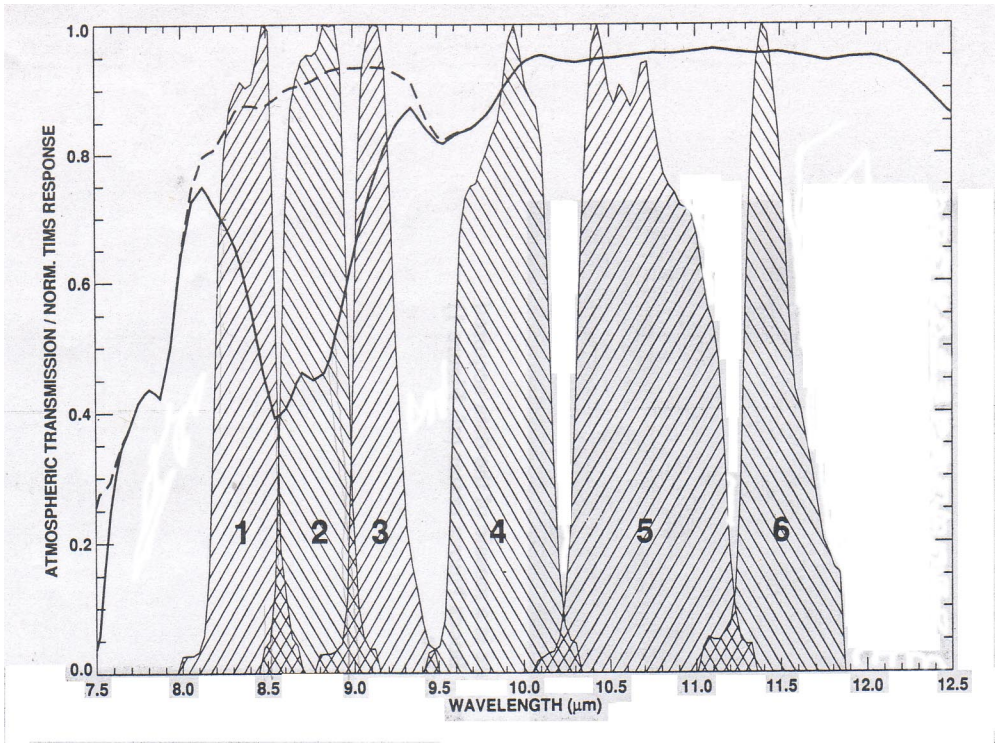

Figure 21. Atmospheric Transmission Profiles With and Without SO_2 (from Realmuto et al., Figure 2, p.483)

Often multispectral datasets exhibit high correlation and produce rather bland color images; however, a decorrelation stretch can be applied to produce a more colorful composite image, which could more effectively display information contained in the image by applying colors to specific bands of wavelengths. A decorrelation stretch requires three bands for input. The bands will be represented in the red, green, and blue (RGB) colors. (Research Systems, 2001, p. 580) With TIMS data, bands 5, 3, and 2 are often chosen to represent red, green, and blue respectively. The SO_2 will absorb the ground radiance in channel 2, implying that the blue color is absorbed in the image. This will create an image with the SO_2 plume displayed in shades of yellow and red. This decorrelation stretch technique is illustrated in Figure 22 with a TIMS image acquired over the East Rift Zone of Kilauea Volcano, Hawaii on September 30, 1988. (Realmuto et al., 1994, p. 482)

The SO_2 absorption feature is a function of all of the input parameters listed previously in Table 4. These parameters can all be determined through various ancillary sources. There are two additional parameters that influence the

Figure 22. Decorrelation Stretch Applied To TIMS Image Data (Realmuto et al., Figure 2, p. 15060)

existence of the SO_2 absorption feature that cannot be determined by ancillary sources: ground temperature and SO_2 concentration. SO_2 concentration is modeled as an atmospheric constituent in the MODTRAN code, and the ground temperature is estimated using the collected radiance data. There are many combinations of ground temperature and SO_2 concentration that will produce the same fit to a radiance spectrum, so the problem of quantifying the SO_2 absorption feature remains underdetermined at this point. Realmuto et al. (1994) uses a two-step process to produce a solution. (Realmuto et al., 1997, p.15061)

The first step involves using TIMS radiance data from channels 4, 5, and 6 to determine values for ground temperature. As is shown in Figure 21, these three channels are not affected by the presence of SO_2 in the atmosphere. Their "resilience" to the presence of SO_2 implies that the ground temperatures determined within these wavelengths should not fluctuate whether a plume is present or not. Several temperatures are estimated and used in the MODTRAN code with wavelengths corresponding to channels 4, 5, and 6. The SO_2 concentration is modeled as 0 gm^{-3}. The various MODTRAN radiance profile results are compared with the TIMS radiance profiles observed in channels 4, 5, and 6 until the model ground temperature that produces the best weighted least squares fit between the two radiance profiles is established. This model ground temperature is then used in the second step of the solution. (Realmuto et al., 1997, p.15061)

The second step involves using TIMS radiance data from channels 1, 2, and 3 to determine SO_2 concentration. The model ground temperature from the first step is used along with several estimated SO_2 concentrations. These are used in the MODTRAN code, and the radiance profile results are again compared with the TIMS radiance profiles. The results are compared until the SO_2 concentration that produces the best weighted least squares fit between the two is established. Channels 1 and 6, located near water vapor and CO_2 absorption bands respectively, are given less weight in both of the fitting processes. The SO_2 concentration determined in the second step can be multiplied by the plume thickness to produce an estimated SO_2 column abundance with units of gm^{-2}. (Realmuto et al., 1997, p.15061)

In addition to applying this estimation procedure to single pixels, it can also be applied to a line of pixels that transects the plume. This is similar to the way COSPEC collects data in straight-line distances perpendicular to the plume. Following the estimate of the column abundances for each pixel, the total SO_2 burden (gm^{-1}) can be integrated across the line of pixels for each transect. Multiplying the SO_2 burden by the wind velocity produces an estimated emission rate. An average of the estimated emission rates for each transect produces an emission rate for the day similar to the methods of COSPEC. (Realmuto et al., 1994, p. 485)

(2) Plume Mapping Procedure. In 1997, Realmuto et al. extended the SO_2 estimation procedure to develop a plume mapping procedure. The estimation procedure is based on data from individual pixels and the mapping procedure simply extends this to allow an estimation of SO_2 over blocks of adjacent pixels, creating a two-dimensional SO_2 plume map.

Realmuto et al. applied this mapping procedure to data acquired in an area of the East Rift Zone of Kilauea Volcano on September 30, 1988. Pu‘u‘O‘o was one of the active vents providing data in 1988, and it continues to be active today. Figure 23 illustrates a map of the ground temperature estimation step with a corresponding SO_2 column abundance estimation map for the Pu’u’O’o vent. The quantified results of SO_2 burden and emission rate for each transect of the plume are displayed in Table 5.

Realmuto et al., draws several conclusions about the scene by comparing the ground temperature and column abundance maps. The ground

temperature map indicates variations in the ground temperature beneath what appears to be a fairly constant SO_2 column abundance on the west edge of the plume. This anomaly

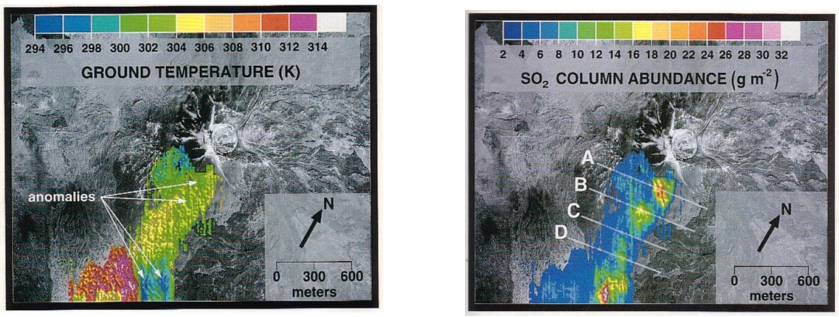

Figure 23. Estimation Maps of Ground Temperature and SO_2 Column Abundance Generated For Pu'u'O'o Vent Of Kilauea Volcano, Hawaii (after Realmuto et al., Figure 3 and Figure 4, p. 15061 – 15062)

Transect	Total SO2 Burden g/m	SO2 Emission Rate kg/s	t/d
A	5176	29.5	2549
B	3763	21.4	1849
C	1989	11.3	976
D	2505	14.3	1236

Table 5. Quantified TIMS Results Of Pu'u'O'o Data Collected On September 30, 1988 (After Realmuto et al., 1997, p. 15066)

was determined to be caused by the sensitivity of the ground temperature estimates to the different textures of lava in the scene. The rough surface of an aa flow allows aerodynamic cooling so that it is cooler than glassy pahoehoe flows in the ground temperature maps. Figure 24 displays these two common types of volcanic surface textures. (Realmuto et al., 1997, p.15064)

Figure 24. Typical Pahoehoe And Aa Lava Flows

The SO_2 abundance map indicates that there are small areas of the plume that were significantly denser than others. These areas are referred to as puffs

within the plume. A comparison between these puffs and the corresponding ground temperatures produces several anomalies indicated on the ground temperature map.

The northern puffs do not create the expected variation in ground temperature, although a small variation is present. It was determined that these northern ground temperature anomalies are more likely to have been produced by a small amount of water vapor in the puffs that was not accounted for in the estimation procedure. These ground temperature variations are not necessarily related to the apparent increase of SO_2 column abundance in the puffs. There is not sufficient evidence to invalidate either the ground temperature or column abundance results, so they are maintained and used in the final emission rate calculations for the vent. (Realmuto et al., 1997, p.15064-15065)

The southern puffs do appear to cause a significant variation in ground temperature. With the aid of data collected in visible wavelengths, it was determined that these puffs actually correspond to meteorological clouds that were present at the time of data collection. These puffs are therefore excluded from the final emission rate estimate. These examples stress the importance of comparing temperature and column abundance results in order to detect and validate any anomalies. (Realmuto et al., 1997, p. 15065)

(3) Comparison of TIMS Plume Mapping Procedure With COSPEC Results. The HVO Staff collected COSPEC data for the Pu'u'O'o vent using a tripod and the stationary ground collection technique on September 20, 1988, just 10 days before the collection of TIMS data used in producing Figure 23 and Table 5. COSPEC collected data for 29 transects over 3.5 hours, while TIMS collected data for 4 transects over 16 seconds. This difference in time required for data collections can have significant impacts on the measurement results as is discussed in a following paragraph. Table 6 is a comparison of these TIMS and COSPEC results collected over the Pu'u'O'o vent. (Realmuto et al., 1997, p. 15067-15069)

Although the emission rate is the standard reported COSPEC measurement, Realmuto et al. (1997) state that a comparison between the results of TIMS and COSPEC would be more appropriate using the SO_2 burdens of individual transects. Several reasons are given to support this statement. For both instruments, the emission rate is not directly measured. It is the result of multiplying the SO_2 burdens of the

Measurement Units	kg/s	t/d
Average Daily Emission Rate		
TIMS (Sept 30, 1988)	16.8 - 20.2	1449 - 1741
COSPEC (Sept 20, 1988)	7.6 - 11.6	661 - 1001
Average Yearly Emission Rate		
COSPEC (1988)	8.3 - 12.9	720 - 1120
Highest Emssion Rate For Year		
COSPC (1988)	14.5	1255

Table 6. Comparison of TIMS and COSPEC Results

transects by wind speed. As noted in an earlier chapter, wind speed is a large source of error in the COSPEC measurements. The SO_2 burdens of COSPEC's transects ranged from 1100 to 3000 gm-1. The TIMS SO_2 burdens ranged from 1900 to 5100 as seen in Table 5. This is a much closer comparison than that shown by the emission rates in Table 6, promoting the comparisons of SO_2 burdens vice emission rates.

Realmuto et al. (1997) suggest that the small difference that exists in the SO_2 burdens could stem from the puffs within the plume and the collection techniques of both instruments. The slow speed of COSPEC's ground stationary collection method and the low wind speeds might have allowed the puffs to be diluted within the measured profile. For TIMS collection, wind speed in the direction of flight was nearly negligible relative to the ground speed of the aircraft. This meant that the puffs would have appeared instantaneous to TIMS accounting for the higher SO_2 burdens in TIMS' transects A and B.

(4) Errors and Sensitivity of Estimation and Mapping Procedures. In 1997, Realmuto et al. determined an error budget of +/- 20% for the mapping procedure. This is considered a minimum error, as not all of the error sources can be quantified. The main sources of error noted by Realmuto et al. are: the accuracy of radiance measurements made by TIMS, approximations such as plume thickness and altitude that are made during the estimation procedure, and the description of the transfer of radiation from the ground to the sensor involving atmospheric conditions and ground emissivity. (Realmuto et al., 1997, p. 15067)

Several analyses have been conducted to determine the sensitivity of the mapping procedure to the various error sources. It is noted that the procedure is most sensitive to estimates in the plume altitude. Realmuto et al., (2000) suggest several methods to determine plume altitude when direct field observations cannot be made. An

assumption that the plume altitude is approximately equal to the elevation of the source vent is one of the simplest methods. Shadows cast by the plume may be used with the solar azimuth and elevation at the time of data collection as another method. Glaze et al. (1999) have developed a method based on photoclinometry, using the brightness of pixels to determine orientation of the corresponding surface to the sun. Regardless of the method used, the mapping procedure assumes that the plume is in thermal equilibrium with the troposphere and therefore defines the temperature contrast between the SO_2 plume and ground. As the altitude estimates increase, there is a corresponding increase in temperature contrast. The increased temperature contrast decreases the amount of SO_2 required to indicate absorption. Analysis determined that variances in plume altitude could cause errors as large as 12%. Variances in other sources caused errors on the order of 4% or less. Table 7 lists several error sources with corresponding results generated from various sensitivity analyses. (Realmuto et al., 1997, pp. 15066–15067)

Error Source	Variances Tested	Sensitivity Results
Plume Dimensions		
Plume Altitude	Variances of up to 50%	Decreases in SO2 column abundnaces up to 12%
Plume Thickness	Reductions of up to 60%	Decreases in SO2 column abundnace less than 4%
Atmospheric Profiles		
Relative Humidity	Increase of up to 100%	Decreases in SO2 column abundance less than 4.3%
Relative Humidity	Reduction of 50%	No change in SO2 column abundance
Model Atmospheres	Substituted MODTRAN model atmosphere for radiosonde data	Changes in SO2 column abundance less than 10%
Ground Emissivity	Assumed constant emissivity	Increases in SO2 column abundances less than 4%
Ground Elevation	Reductions of up to 24%	Decreases in SO2 column abundance less than 1.5%

Table 7. Sensitivity Analysis Results For SO_2 For Plume Mapping Procedure

2. Advanced Spaceborne Thermal Emission Reflection Radiometer (ASTER)

In 2000, Realmuto et al., extended the application of the SO_2 mapping procedure to data simulating satellite collection. For the collection simulation parameters, Realmuto chose to model the Moderate Resolution Imaging Spectroradiometer (MODIS) and Advanced Spaceborne Thermal Emission Reflection Radiometer (ASTER). These are two LWIR sensors employed on the Terra satellite that is part of NASA's Earth Observing System. ASTER has a spatial resolution of 90 meters, much finer than the 1 km resolution of MODIS. This paper will focus on the ASTER sensor, as its enhanced spatial resolution provides better comparisons between airborne and spaceborne sensors.

a. ASTER Description

ASTER is a cooperative effort between NASA and Japan's Ministry of Economy Trade and Industry (METI). It is an imaging sensor with a main mission of

collecting data for detailed maps of land surface temperature, emissivity, reflectance, and elevation. ASTER has a Visible and Near Infrared (VNIR) subsystem, a Shortwave Infrared (SWIR) subsystem, and a Thermal Infrared (TIR) subsystem. Each subsystem has its own telescope. Table 8 displays characteristics of each of these subsystems. The focus for this paper is the TIR subsystem.

Characteristic	VNIR	SWIR	TIR
Spectral Range (microns)	.52 - .86	1.6 - 2.36	8.125 - 11.65
Spectral Bands	3	6	5
Ground Resolution (m)	15	30	90
Data Rate (Mbps)	62	23	4.2
Cross-track Pointing (degrees)	+/- 24	+/- 8.55	+/- 8.55
Cross-track Pointing (km)	+/-318	+/-116	+/-116
Swath Width (km)	60	60	60
Detector Type	Si	PtSi-Si	HgCdTe
Quantization (bits)	8	8	12

Table 8. Characteristics of ASTER's Three Subsystems (after Hook, "Instrument")

The TIR subsystem is sensitive to a wavelength range of 8 – 11 microns. This range is spread over 5 spectral bands. The system response of each of these bands is illustrated in Figure 25. Each band has 10 HgCdTe detectors in a staggered array. These

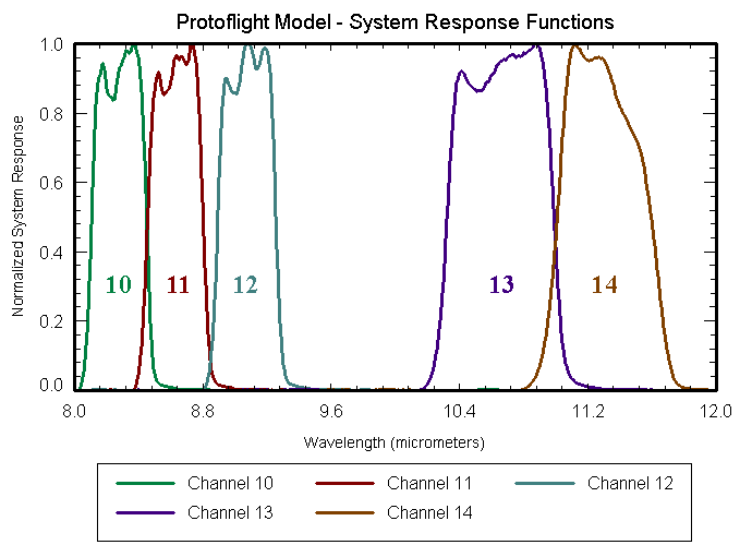

Figure 25. Spectral Response for ASTER's TIR Subsystem (from Hook, "Instrument")

detectors are maintained at a temperature of 80 degrees K by a split Sterling mechanical cooler. The NEΔT is less than .3 K for all bands. The sensor is calibrated with an

internal adjustable temperature black body. The TIR subsystem is fixed and requires a mirror to perform any scanning or pointing.

b. ASTER Simulation and Results

In the spaceborne simulation of the estimation and mapping procedures, two main differences emerge by moving the sensor's operating altitudes from 1- 20 km (TIMS) to 705 km (ASTER): the sensor's resolution is decreased and the longer path of travel through the atmosphere decreases the amount of radiance perceived by the sensor. Realmuto et al. chose to work with the same TIMS, September 30, 1988, Pu'u'O'o data discussed previously. In order to create an image as it might be viewed through ASTER, the TIMS data was resampled to a 90-meter spatial resolution. After the data was resampled, the estimation and mapping procedures were applied. Figure 26 is an image of the area used in the simulation with a decorrelation stretch applied. As previously discussed, this causes the SO_2 plume to appear in shades of yellow and red.

Figure 26. Simulation Data With A Decorrelation Stretch Applied (after Realmuto et al., Plate 1, p. 106)

The SO_2 abundance results of the simulation are displayed in Figure 27. ASTER proved to show favorable results when compared with TIMS. The decrease in ASTER's spatial resolution reduces or dilutes the column abundance estimates by increasing the area covered by each pixel. Although this effect did prohibit ASTER from producing some of the higher column abundances of the puffs that can be seen with TIMS, the dilution was not significant enough to cause the presence of the puffs within the plume to be completely overlooked. (Realmuto et al., 2000, p. 108)

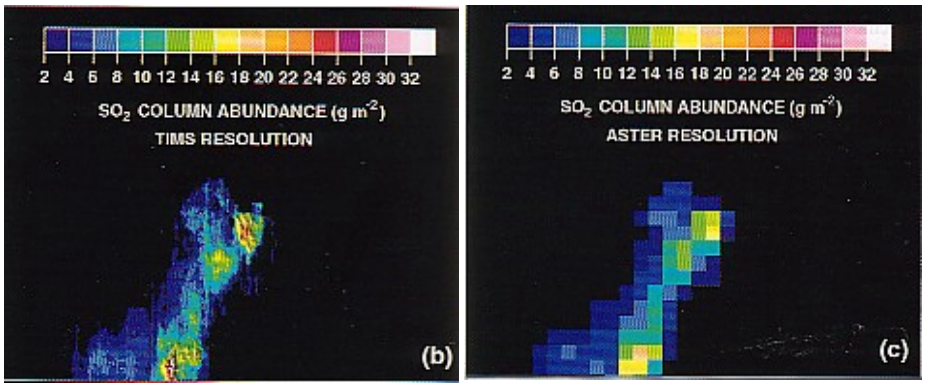

Figure 27. Comparison of Pu'u'O'o Plume Maps At Spatial Resolutions of TIMS and ASTER (After Realmuto et al., Plate 1, p.106)

With the concern of spatial resolution set aside, Realmuto et al. next addressed the concern of ASTER's sensitivity. Another simulation was run to determine the apparent reductions in ground temperature that a sensor operating at 705 km might detect by viewing the ground through the 1988 Pu'u'O'o plume. The simulated transmission path was generated through a combination of radiosonde data (0 - 10 km) and the MODTRAN tropical atmosphere model (10 – 705 km). The simulation results are displayed in Figure 28. The changes in temperature are derived from radiance spectra

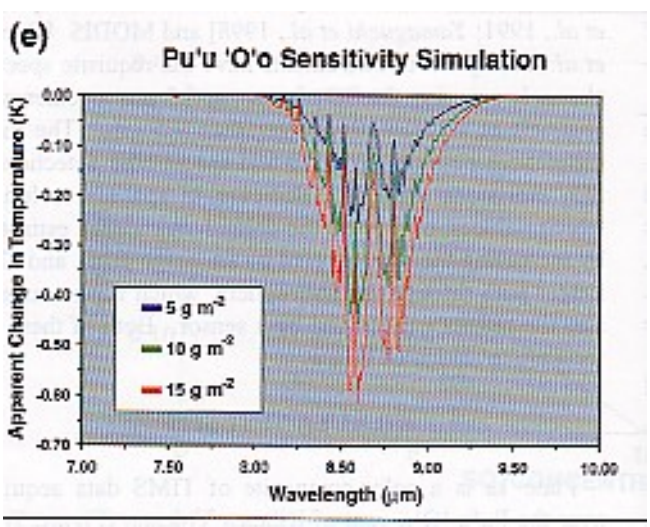

Figure 28. Results of ASTER's Sensitivity Simulation (After Realmuto et al., Plate 1, p.106)

calculated for an atmosphere that was free of SO_2 and for three additional atmospheres with different simulated plume abundances. As previously mentioned, ASTER's NEΔT is less than .3 Kelvin for each of its 5 spectral bands. The temperature differences

derived for the 10 gm^{-2} and 15 gm^{-2} plume abundances exceed this value and would be detected; however, the smaller 5 gm^{-2} plume abundance does not generate a large enough temperature difference for ASTER to detect. (Realmuto et al., 2000, p. 108)

With the promising results of the simulation, Realmuto et al. concluded that ASTER should be able to detect SO_2 plumes of similar size and characteristics to Pu'u'O'o. Realmuto et al. (2000) also suggest that ASTER could be used in conjunction with MODIS and TOMS (an ultraviolet spaceborne sensor) for many important large scale studies such as: establishing baseline emission rates and performing change detection for volcanoes around the world, mapping atmospheric products generated by volcanic eruptions, and documenting the life cycle of SO_2 through its development to H_2SO_4. (Realmuto et al., 2000, p. 112)

3. Airborne Hyperspectral Imager (AHI)

The University of Hawaii's Hawaii Institute of Geophysics and Planetology (HIGP) designed and built AHI as part of the Defense Advanced Research Projects Agency's (DARPA) Hyperspectral Mine Detection (HMD) program. The main goal of the program was to develop and demonstrate a hyperspectral infrared capability for remote buried mine detection. The program outlined several high level system and sensor requirements based on an extensive phenomenology measurement program that guided the design and construction of AHI. (Lucey et al., 1998, p. 36)

a. System Design

The HMD program established the following five high-level system design requirements (Lucey et al., 1998, p. 38)

- Must be airborne
- Must provide real-time detection of mines
- Must be demonstrated in a realistic scenario
- Must demonstrate a clear path to an operational system
- Must have the capability of serving as a phenomenology data collection platform

These requirements led to the development of the AHI system pictured in Figure 29. The system collects data through an infrared and visible sensor that are coupled with a real time processing system developed by Technical Research Associates, Inc. (TRA) and

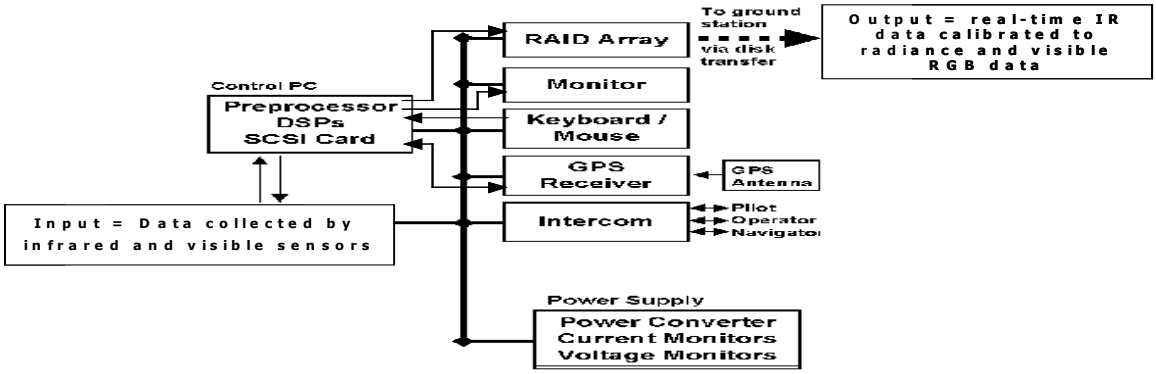

Figure 29. AHI System Components (after Lucey et al., Figure 3, p. 41)

Space Computer Corp. The processing system controls many important system functions. It performs sensor control, generation of calibration coefficients, geometric preprocessing, real time radiometric calibration, near real time detection algorithm processing, user interface control, and data recording. A Xilinx field programmable gate array (FPGA) and four Sharc digital signal processors (DSP) are the main components of the processing system. These components receive the raw 12-bit digital data from the sensors, spectrally bin the data, apply calibration components, compute principal components, apply the detection algorithm, and then pass the calibrated raw data and principal components to a Pentium PC and 12 Gigabyte Redundant Array of Independent Disks (RAID) for storage. A GPS receiver also collects and sends information to the RAID for storage. The visible and infrared data can also be displayed as it is collected in

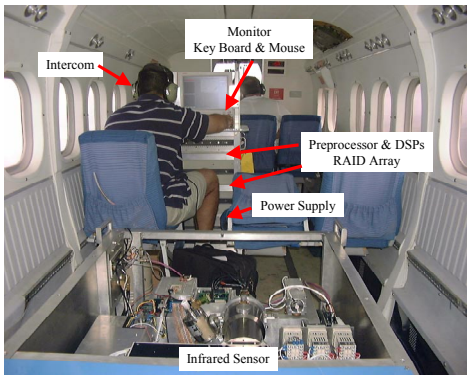

Figure 30. AHI System Mounted In A Twin Otter Fixed Wing Aircraft

waterfall plots on the system's monitor. Figure 30 displays the system as it is mounted in a twin otter fixed wing aircraft while Figure 31 is a snapshot of the monitor display during data collection. (Williams "Sensor Details")

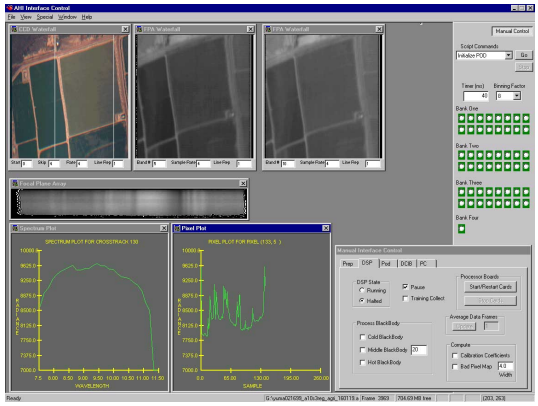

Figure 31. Snapshot of AHI's Monitor Display

b. Sensor Design

In addition to system requirements, DARPA's HMD program also outlined the following sensor requirements (Lucey et al., 1998, p. 38):

- Spectral Range: 8.3 – 11 microns
- Spectral Resolution: <32 wavenumbers
- Noise Equivalent Spectral Radiance (NESR): < 0.01 watt/m^2-micron-sr at 300 degrees Kelvin
- Pixels per target: >30

With these baseline requirements, the University of Hawaii's HIGP built a sensor that consists of the following four subsystems illustrated in Figure 32: telescope, spectrograph, background suppressor, and FPA with associated electronics. The telescope is a two-element diffraction limited transmission lens with a 111-micron focal length and 35 mm aperture. The spectrograph is an uncooled commercial reflective f/4 imaging spectrograph with gold-coated optics. It is a grating spectrograph that has a linear dispersion at the output. An uncooled spectrograph is possible due to the sensor's background suppressor. The background suppressor cools the FPA, a three-element transmission reimaging system, and a linear variable filter that are all housed in a vacuum

dewar. The FPA is a 256 by 256 Rockwell TCM2250 HgCdTe array sensitive to an LWIR band from 7.5 to 11.5 microns. It is cooled to 56 degrees Kelvin (K) by a 1.5 watt

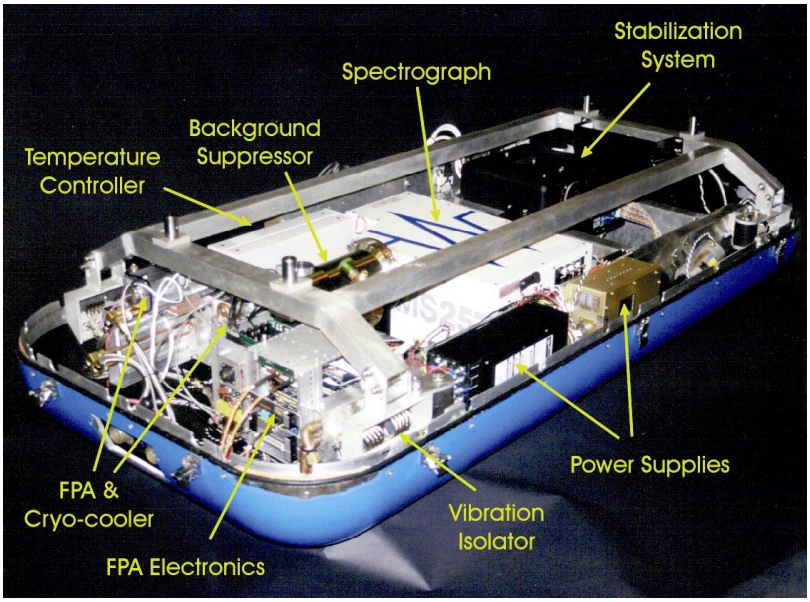

Figure 32. Main Subsystems of the Sensor Design (from Lucey et al., Figure 1, p. 37)

split Stirling mechanical cryocooler. At 56 K, the half power drop-off in sensitivity is at 11.5 microns. The array is operated at its maximum frame rate of 150 Hz with an integration time of 3 milliseconds in order to avoid saturation for scenes that may contain temperatures of 70 degrees Celsius. A separate 0.1 liter liquid nitrogen reservoir cools the sensor's optics. (Lucey et al., 1998, p. 40)

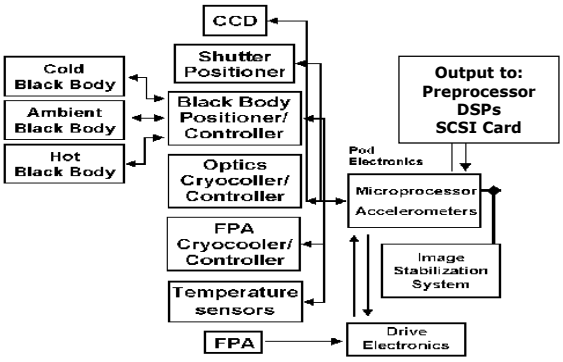

Figure 33. Main Components of Sensor Subsystems (after Lucey et al., Figure 3, p. 41)

The sensor also has an on-board adjustable temperature black body that provides information for real-time data calibration and conversion to radiance. In

addition to the LWIR capabilities, the sensor can also collect data in visible wavelengths through a 3-color CCD linescan camera. These major components of the sensor's subsystems are illustrated in the block diagram in Figure 33. (Lucey et al., 1998, p. 42)

AHI's on-board computer has custom software that controls and monitors several sensor functions such as: control of the pod environmental shutter, the black

Physical Specifications

Size (LWH in inches of imager only)	47 x 27 x 17
Imager Weight (pounds)	300
Control & Rec Module (pounds)	122
Power Requirements	1000 W (35 Amps @ 28 VDC)
Operating Environment	0 - 15,000 ft pressure altitude, -20 to +50 degrees C, Passive vibration isolation
FPA Cooler	Closed cycle sterling cooler - 56K

Detector Specifications

Imager	256 x 256 element Rockwell TCM2250 HgCdTe FPA
Spectral Coverage (microns)	7.5 - 11.5
Number of Spectral Bands	256 or 32

Optics Specifications

Spectral Resolution	125 nm (32 bands) or 100 nm (256 bands)
Angular Resolution (mrad)	.9 x 2
Focal Length (microns)	111
Slit (microns)	200
Aperture (mm)	35

Performance Specifications

Quantization	12 bit
Integration Time (ms)	3
Frame Rate (Hz)	150
Data Rate (Mbps)	10
Output Data Format	AHI convertible to ENVI image format
Display	Flight real time desplay, SVGA Monitor
Operating System	PC-based, Windows NT
Software	Custom software for data and image acquisition, post mission review and processing, archival support
Data Archive	8mm Exabyte tape or IDE hard disk
Data Storage	12 GB ~hot swappable
FOV	7 degrees cross track - pushbroom hyperspectral imager
Guidance Sensor	C-MIGITS II: heading, pictch, roll, lat, lon
Position Accuracy	< 10 m
NEDT	< .1 K @ 300 K
NESR	< .02 watts/m^2-sr-micron
Radiometric Calibration	NIST traceable
Ancillary Data	Color linescan CCD with twice the IR swath width

Table 9. Physical and Performance Specifications of the AHI System and Sensor

bodies, and the measurement modes. Several performance parameters of the sensor can be observed via plots such as noise and radiance histograms that can be displayed in real-time on the system's computer monitor. This is illustrated in Figure 31. Additional details on the system and sensor physical and performance specifications are found in Table 9. (Williams, "Sensor Specifications")

c. *Data Collection Techniques and Applications*

(1) Data Collection. AHI collects data in a pushbroom fashion. The focal plane array has 256 rows of 256 pixels each. The 7.5 – 11.5 micron band of wavelengths is spread over the 256 rows so that each row represents a narrow band within this broad LWIR region. AHI simultaneously obtains spectra for 256 points on the ground. As the focal plane array is pushed along the flight line, these rows will begin to overlap and form a hyperspectral data cube with 256 pixels along the x-axis, a number of pixels along the y-axis that is determined by the duration of collection along the flightline, and 256 x-y image planes in the z-axis, each representing one of the narrow bands of wavelengths within the 7.5 – 11.5 micron region. Figure34 illustrates this pushbroom concept using a hyperspectral FPA and the resulting hyperspectral data cube.

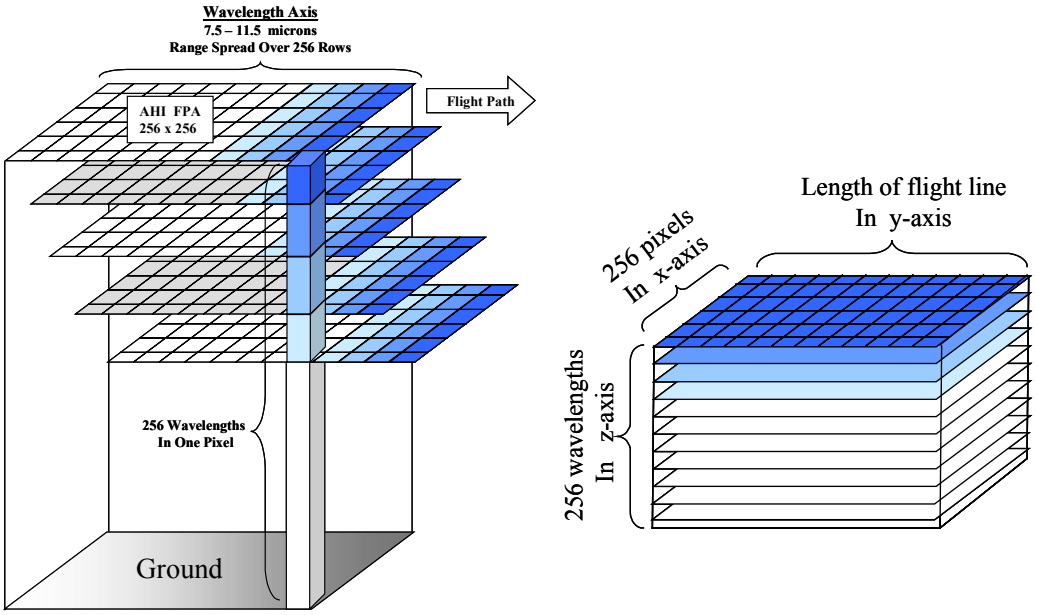

Figure 34. Pushbroom Hyperspectral Data Collection and Resulting Data Cube

Calibration is performed using the on-board adjustable temperature black body. High and low temperatures are chosen for the black body based upon the expected maximum and minimum temperatures to be imaged in the scene. A middle temperature for the black body is set near the average of the high and low temperatures. One hundred frames of data are collected at each temperature. The high and low temperatures are used to compute gains and offsets that are applied to data collected

using the middle temperature producing corresponding radiance data. Signal to noise is calculated over all the calibrated pixels for each wavelength so that spatial nonuniformity noise is included in the calculations. The black body data is also used to identify bad pixels in the focal plane array. A bad pixel is characterized as non-responsive, saturated, or "noisy" in the collection of the 100 frames of black body data. (Lucey et al., 2000, p. 34-35)

(2) Sensor Applications And Collection Platforms. AHI was originally designed for real-time mine detection. For this mission, the sensor operates in a pod mounted under a helicopter. Following successful demonstration of this mission, HIGP explored additional applications and collection platforms for AHI. AHI currently has three main collection platforms: helicopter, fixed wing Twin Otter or Navajo aircrafts, and various ground platforms. Figure 35 displays AHI operating from its three main collection platforms.

Figure 35. AHI Collection Platforms: Helicopter, Ground Based, and Fixed Wing Aircraft

To date, HIGP has demonstrated the following applications with AHI:

- Airborne detection of land mines
- Hyperspectral land mine phenomenology
- Concealed target detection and phenomenology
- Gas detection
- Active laser hyperspectral imaging
- Geologic mapping
- Coastal water temperature mapping
- Missile defense intercept test support
- Hyperspectral basic research data collection

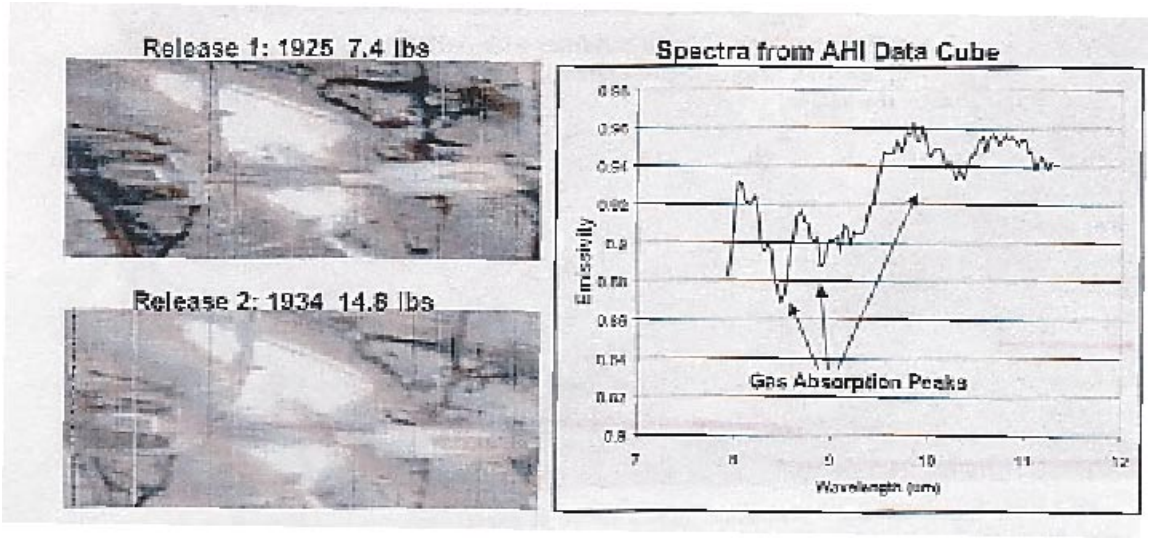

Figure 36. Single Band Images and Single Pixel Spectra Demonstrating AHI's Gas Detection Capability (from Lucey et al., 2000, p. 35)

This paper further explores AHI's application in gas detection. An initial experiment was conducted in which AHI flew over a site multiple times where different known quantities of gas were released. Single band images and a single pixel spectrum from this experiment are shown in Figure 36. Figure 37 illustrates the use of a matched filter on

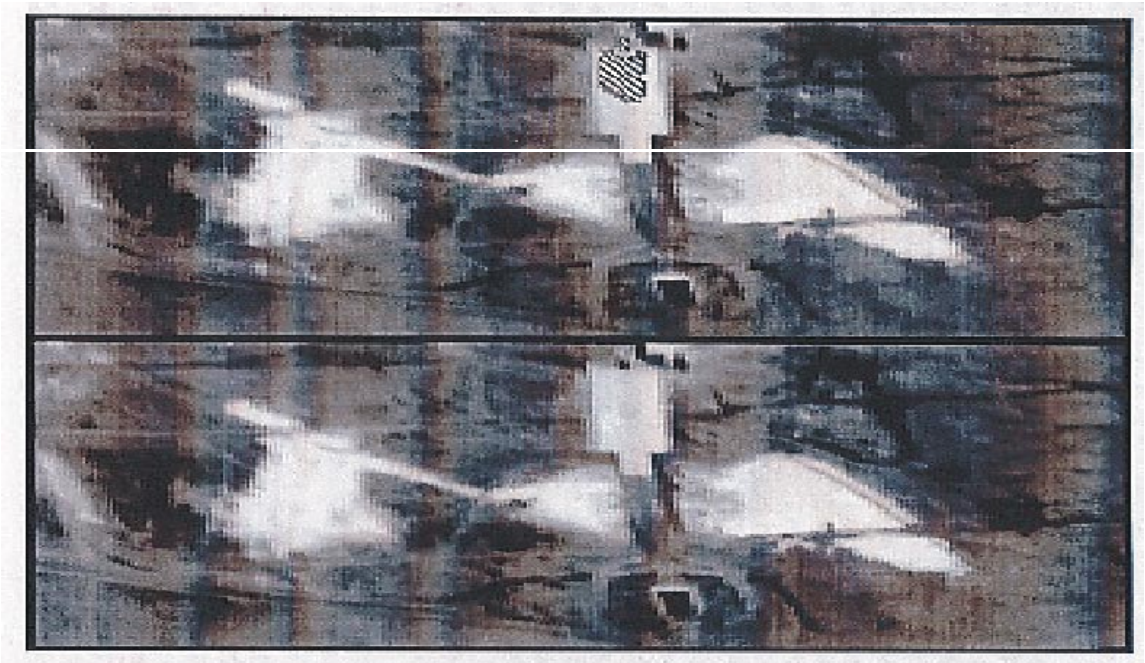

Figure 37. Using Matched Filter On Single Band Images Indicating Gas Detection In Hashed Area (from Lucey et al., 2000, p. 36)

this data and confirms AHI's ability to detect and characterize gases with broad spectral features. This paper extends AHI's ability beyond the basic gas detection and characterization to quantifying a gas concentration. In Chapter IV, data collected over Hawaii's volcanoes are used to demonstrate this extended capability through analysis of the volcanic SO_2 plumes.

B. SUMMARY OF IR DETECTION

Using COSPEC data analysis results as ground truth, Realmuto et al. successfully demonstrated the ability to detect and quantify SO_2 plumes using TIMS, NASA's airborne multispectral LWIR sensor. In 1994, Realmuto et al.'s estimation procedure, based on a least squares fit between radiance profiles generated by the LWIR sensor and MODTRAN simulations, produced ground temperatures and SO_2 column abundances for single pixels in a data set. In 1997, the application of the estimation procedure was expanded and applied to groups of adjacent pixels, developing the ability to produce a two-dimensional map of an SO_2 plume. Finally in 2000, Realmuto et al., simulated the application of these estimation and mapping procedures to data that might be generated by an LWIR sensor employed on a satellite. In each of these cases, the results produced by the LWIR sensor reasonably compared with analysis performed by COSPEC.

Although the LWIR sensors proved successful, Realmuto et al. did not suggest that they be used to replace COSPECs. It was suggested that a combination of LWIR and UV detection and quantification would be best. Using multiple regions of the electromagnetic spectrum and varying collection methods will compensate for the weaknesses noted in each, as well as compound their strengths. (Realmuto et al., 2000, p. 15071)

Realmuto et al.'s estimation and mapping procedure form a basis for data analysis techniques and methods to be applied to data collected by AHI in the following chapter. A new 2002 data set collected by both AHI and COSPEC over the Pu'u'O'o vent is used for comparison.

IV. DATA COLLECTION AND SO_2 DETECTION

A. DATA COLLECTION

A data collection experiment was conducted on April 18, 2002. Figure 38 displays two pictures of the Pu'u'O'o Vent of Kilauea Volcano in Hawaii. The picture on the left is a visible image of the vent taken from an aerial view looking west-southwest. The picture on the right is an LWIR image of the vent taken by AHI mounted on a twin-otter plane also looking west-southwest. Both images were taken on April 18, 2002. The AHI image is one of several that were collected for data in support of this paper.

Figure 38. Visible and Infrared Image of Pu'u'O'o Vent of Kilauea Volcano, Hawaii, Collected on April 18, 2002

COSPEC, FLYSPEC, and AHI collected data on the SO_2 plume of the Pu'u'O'o vent on the morning of April 18, 2002. The original plan involved all three sensors collecting concurrent and corresponding data sets; however, several timing, communication, and weather issues prevented this from happening.

1. Weather Conditions

The quality of data collected via remote sensing instruments is often at the mercy of Mother Nature and the weather. As discussed in Chapter II, clouds and wind are two

of the major weather concerns in the UV analysis of SO_2 plumes. Chapter III notes that all aspects of the atmospheric profile between the ground and the sensor impact the IR analysis of SO_2 plumes. In both cases, weather conditions are an important aspect of data analysis and must be noted.

COSPEC, FLYSPEC, and AHI collected data between the hours of 9:00 and 11:00 a.m. Weather observations for these two hours were obtained from the weather station at the Hilo Airport, approximately 37.5 km north of Pu‘u‘O‘o and at an elevation of 44 feet above mean sea level. Between these hours the station reported clear skies with a few scattered clouds, an average surface air temperature of 26.7 degrees Celsius, a relative humidity of 68 percent, and a barometric pressure of 1013.5534 millibars. The winds were very light and variable out of the east-southeast.

Most of these conditions were ideal with the exception of the winds. Ideal wind speeds and directions for data collection on the Pu’u’O’o plume are noted in Chapter II as northeasterly trade winds with a consistent speed of 5 m/s. These ideal wind conditions normally carry the plume from Pu’u’O’o down over the Chain of Craters Road. The east-southeast winds of April 18 carried the winds over Highway 11. The light and variable speeds prevented the analysis of an emission rate for the data collected, as a steady and consistent wind speed is one of the main variables in this calculation. A map of the routes covered by each of the sensors is displayed in Figure 39.

2. COSPEC and FLYSPEC Data Collection

Mounted on the same vehicle, COSPEC and FLYSPEC collected data on April 18 using the ground mobile technique. As the light and variable winds made the location of the plume somewhat unpredictable, the sensors made an initial collection down the Chain of Craters Road looking for any possible signs of SO_2. There were no indications of the plume along the Chain of Craters Road that morning.

Collections were then made along a portion of Crater Rim Drive and Highway 11. The sensors collected data for nearly 30 minutes (9:58–10:28 a.m.) traveling at a constant speed of approximately 30 mph in the northeast direction along Highway 11. A four-minute section of the data collected in this traverse indicates a portion of plume containing concentrations of SO_2 as high as 747 ppm-m. This 30-minute route was

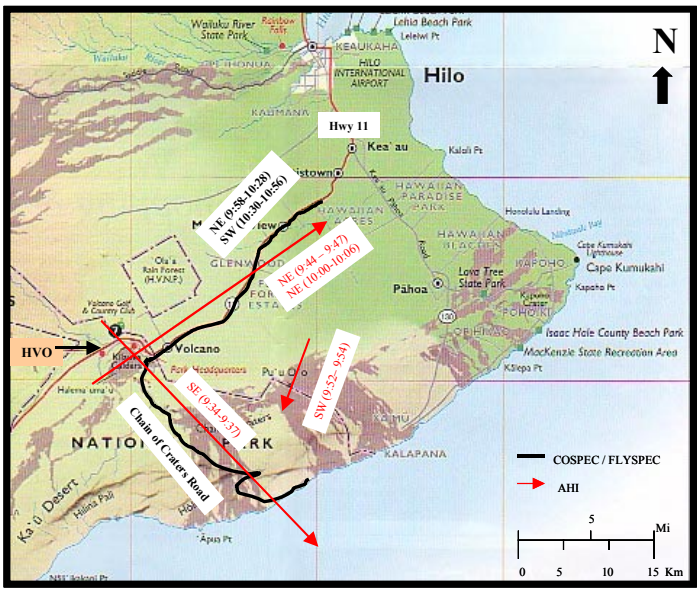

Figure 39. Routes of Data Collection for COSPEC, FLYSPEC, and AHI on April 18, 2002

retraced (10:30–10:56 a.m.) traveling approximately 30 mph in a southwest direction and produced another four-minute section of data indicating a section of plume with concentrations of SO_2 as high as 705 ppm-m. The routes covered by COSPEC and FLYSPEC are highlighted in black with black text indicating times and direction of travel in Figure 39. Additional details on the data analysis results are presented later in the chapter.

3. AHI Data Collection

AHI, mounted in a Piper Navaho plane flying between 4000 and 4500 feet above sea level, collected data over three main areas. Approximately 3 minutes (9:34-9:37 a.m.) of data was collected over the chain of craters road followed by 3 minutes (9:44-9:47 a.m.) of data along Highway 11. Two minutes (9:52-9:54) of data were collected over the Pu'u'O'o Vent followed by a final six-minute collection (10:00-10:06) over Highway 11. The routes covered by AHI are highlighted in red with red text indicating times and direction of travel in Figure 2.

During AHI's flight, multiple files of data were also collected imaging the on-board black body for calibration purposes. Black body temperatures covering a range from 25 to 50 degrees Celsius were imaged. These black body images were used to

convert the digital numbers registered by AHI to values of radiance with units of $W/m^2/sr/\mu$.

As the AHI data were calibrated, each of the runs was spatially segmented into smaller files to facilitate the analysis. The segments were also spectrally binned to reduce the number of bands from 256 to 205. Table 10 lists the four data collections, their associated run names, their corresponding segments, flight times, and image sizes. Each of the data collections will be referred to by its run name and the starting flight time of the appropriate segment from this point on (e.g. R1_A_093134).

Data Collection	Run Name	Segement	Starting Flight Time (hh:mm:ss in HST)	Image Size (samples x lines x bands)
Chain of Craters Road	R1_A	1	09:31:34	256 x 1499 x 205
		2	09:32:26	256 x 1499 x 205
		3	09:34:33	256 x 1499 x 205
		4	09:35:25	256 x 1499 x 205
		5	09:36:18	256 x 1499 x 205
		6	09:37:18	256 x 631 x 205
First Highway 11	R1_B	1	09:44:50	256 x 1499 x 205
		2	09:45:42	256 x 1499 x 205
		3	09:46:35	256 x 1499 x 205
Pu'u'O'o Vent	R1_C	1	09:52:58	256 x 1874 x 205
		2	09:53:49	256 x 1436 x 205
Second Highway 11	R2_B	1	10:00:30	256 x 1499 x 205
		2	10:01:21	256 x 1499 x 205
		3	10:02:13	256 x 1499 x 205
		4	10:03:12	256 x 1499 x 205
		5	10:04:03	256 x 1499 x 205
		6	10:04:55	256 x 1499 x 205
		7	10:05:49	256 x 1499 x 205

Table 10. Summary of Files Produced From AHI Data Collection

B. SO_2 DETECTION

The analysis of AHI's data was approached with two basic goals in mind. The first goal was to demonstrate AHI's ability to detect the presence of SO_2. The second goal was to attempt to quantify the amount of SO_2 detected. This chapter addresses SO_2 detection, while Chapter V addresses the quantification of SO_2.

The analysis performed to determine AHI's ability to detect SO_2 can be broken down into three main areas: initial detection, application of spectral classification tools, and the development of spectral libraries. The data were examined in both radiance and emissive space in each of these areas.

1. Initial Detection

The first area of analysis involved an initial display of the 18 segments of AHI data using the decorrelation stretch method applied by Realmuto et al. to TIMS data. As discussed in Chapter III, the decorrelation stretch is a transform that helps remove the high correlation between bands of a multispectral dataset. A false color RGB image can then be produced to highlight areas of interest. In Realmuto et al.'s specific application of this technique to SO_2 detection, the color blue is assigned to the TIMS Channel 2 (8.6 – 9.0 micron band) that corresponds to a prominent absorption feature of SO_2. Any SO_2 that is present in one of these false color radiance images appears in shades of yellow and red as the blue color representing the radiance in Channel 2 is absorbed.

Each of the AHI radiance images was spectrally resampled reducing the 205 bands to 6, simulating the six spectral bands of TIMS. A decorrelation stretch was applied to each of the simulated TIMS radiance images producing false color RGB images to be examined for any significant areas of yellow color. Appendix A includes the 18 false color RGB images created in this phase and their corresponding AHI radiance image. Only one image appears to have any significant yellow areas. The false

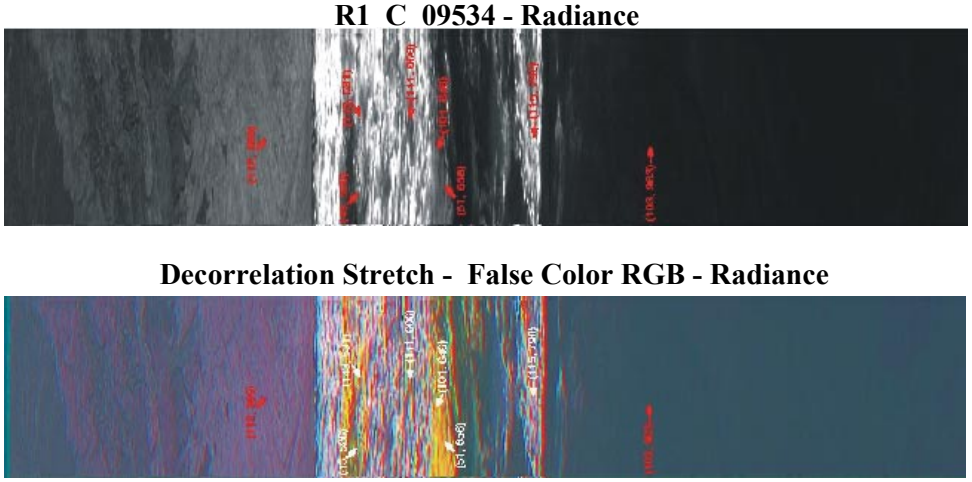

Figure 40. False Color RGB Radiance Image Generated by the Decorrelation Stretch Method

color RGB image of R1_C_095349, a segment of data collected over the Pu'u'O'o Vent, is pictured in Figure 40 with its corresponding AHI radiance image. Several radiance spectra of yellow pixels are compared with radiance spectra of non-yellow pixels in

Figure 41 in order to verify the presence of the SO_2 absorption feature in the yellow pixels. The locations of the pixels used for this verification are identified in Figure 40. R1_C_095349 is the main focus for the rest of the analysis.

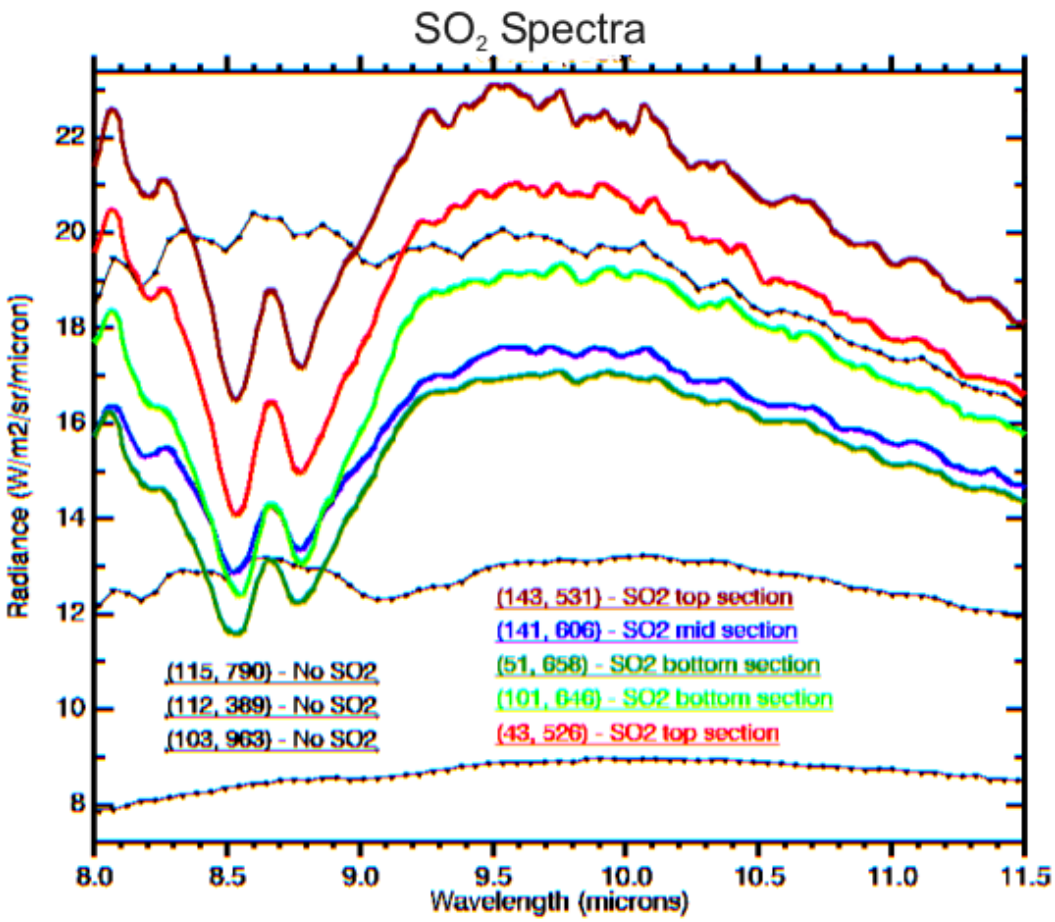

Figure 41. Radiance Spectra of Yellow Pixels Demonstrating the SO_2 Absorption Feature

2. Application of Spectral Classification Tools

The second area of analysis involved applying several different spectral analysis tools to R1_C_095349. The application of a Forward Principal Component Transform, Spectral Angle Mapper (SAM) Method, and Matched Filter (MF) Mapping Method to the image is discussed in the following paragraphs. Results produced by all of these spectral analysis tools are presented in both radiance and emissive space. Interesting comparisons are presented between not only the radiance and emissive spaces, but also between the analysis tools.

a. Conversion From Radiance to Emissive Space

In order to convert the AHI radiance image to an emissive image, the well-known problem of separating temperature and emissivity in thermal infrared data must be addressed. Kealy and Hook describe the spectral emissivity of a material as a measure of its ability to emit radiation compared to a blackbody. In Equation 4.1 emissivity is defined as the ratio of the radiance of a material that may be observed by AHI (L_{AHI}) to that of a blackbody at the same temperature. L_{AHI} can be fully described by the MODTRAN radiance equation described in Chapter III. Equation 4.2 is the Planck function that describes the radiance of a black body (L_{BB}) in terms of the temperature being imaged and the wavelength used for imaging. With remotely sensed data, there are two unknowns in Equation 4.1, the spectral emissivity and the temperature of the observed material. Several methods have been developed to try and solve this underdetermined problem. Kealy and Hook evaluate three of the most common methods

$$\varepsilon(\lambda) = \frac{L_{AHI}(\lambda, T_0)}{L_{BB}(\lambda, T_0)} \tag{4.1}$$

$\varepsilon(\lambda)$ = Spectral emissivity of material as a function of the wavelength used for imaging

$L_{AHI}(\lambda, T_0)$ = Radiance of material observed by AHI as a function of the wavelength used for imaging and the temperature of the material observed

$L_{BB}(\lambda, T_0)$ = Radiance of a black body as a function of the wavelength used for imaging and the assumed true temperature of the material being observed

$$L_{BB}(\lambda, T_0) = \frac{C_1}{\lambda^5 \pi \left[\exp\left(\frac{C_2}{\lambda T_0} \right) - 1 \right]} \tag{4.2}$$

C_1 = First radiation constant = 3.74151×10^{-16} Wm^2

C_2 = Second radiation constant = .0143879 mK

used and suggest that the emissivity normalization method is one of the more accurate methods to use particularly when working with scenes dominated by rocks and soils. (Kealy, P. and Hook, S., 1993, p.1163) Realmuto successfully demonstrated the application of this technique to mapping the basalt flows in Hawaii. Given this background, the emissivity normalization method was chosen to convert the AHI radiance image to emissive space.

The emissivity normalization method starts by assuming a constant value for emissivity. A value of .96 is commonly used and is chosen for this particular case. With L_{AHI} and the emissivity defined, Equation 4.1 can be arranged to solve for the temperature of the material being observed as seen in Equation 4.3. The temperature of each pixel is calculated for each of the 205 wavelengths, and the highest temperature calculated is chosen as the temperature of that pixel. This temperature is then used as a known value in Equation 4.1 to calculate the emissivity of the pixels at each wavelength.

$$T_\lambda = \frac{C_2}{\lambda \ \ln\left[\frac{\varepsilon_\lambda C_1}{L_{AHI}\ \lambda_s \pi} + 1\right]} \tag{4.3}$$

Figure 42 displays the emissivity and temperature images of R1_C_095349 calculated using this normalized emissivity approach.

As discussed in Chapter III, the observed ground temperature is one of the important unknowns in the underdetermined problem of solving for SO_2 plume concentration. The importance of the temperatures in this problem warranted developing a means to verify the results calculated using the normalized emissivity approach. Several random pixels from both the radiance and emissivity images of R1_C_095349 were chosen to verify the calculation. These pixels are annotated in Figure 42. Band 35, corresponding to a wavelength of 8.5344 μ and centered on the SO_2 absorption feature, is used to present the radiance and emissivity images in Figure 42. Apparent instrument artifacts are noted along the edges of the emissivity image.

The calculated temperature of each of the chosen pixels and an assumed emissivity value of .96 were reapplied to Equation (1), generating a simulated AHI black body radiance profile that does not include any atmospheric or SO_2 effects. This

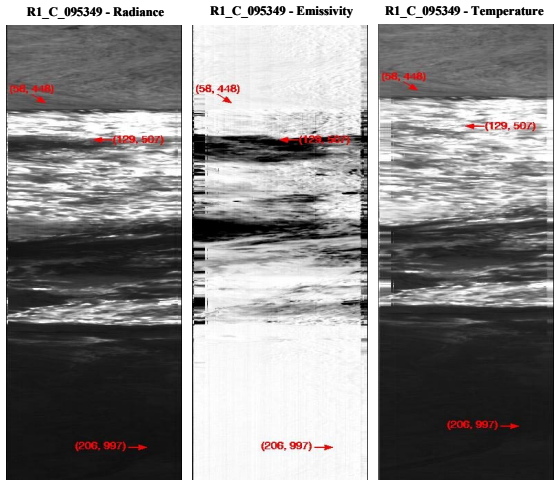

Figure 42. R1_C_095349 Emissivity and Temperature Images Generated By the Normalized Emissivity Method and the Corresponding Radiance Image

simulated black body profile was then plotted against the true AHI radiance profile for each pixel. Figure 43 displays both the radiance comparison and corresponding emissivity profiles generated for a 3 x 3 pixel average around the original pixels annotated in the images of Figure 42. The profiles representing AHI data are depicted with both a line and symbol whereas the simulated blackbody profiles are depicted with a solid line only. As discussed in Chapter III, the longer wavelengths (approximately the

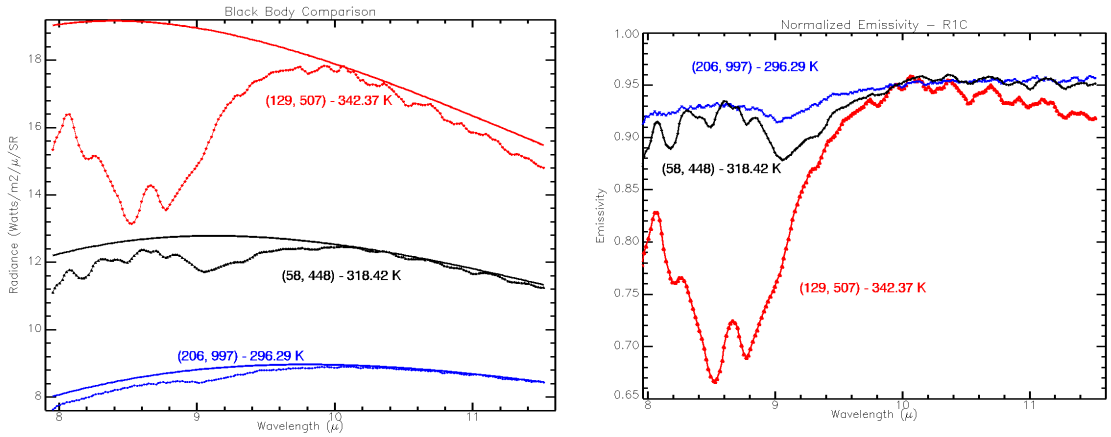

Figure 43. R1_C_095349 Black Body and AHI Radiance Comparison With Corresponding Emissivity Plot

9.5 to 11.5 μ range) are not as effected by the atmosphere and SO_2, so this is where a good fit of the two profiles is desired. Figure 43 demonstrates a reasonably good fit between the radiance profiles within these wavelengths.

The importance of understanding the effects of the method used to separate the temperature and emissivity was great enough to test an additional segment from the dataset. Figure R1_A_093718 was chosen due to the presence of water in the segment. As water has proven to act as a blackbody in LWIR wavelengths, the normalized emissivity method was applied to this segment with an assumed emissivity of 1.0. The resulting temperatures from several pixels of both water and lava were again used to compare the normalized emissivity results to those generated with a simulated AHI black body curve. Figure 44 displays the temperature and emissivity image results from the normalized emissivity method. Band 35, corresponding to a wavelength of 8.5344 μ and centered on the SO_2 absorption feature, is used to present the radiance and emissivity images. The pixels used for the black body comparison are annotated. Figure 45 displays the radiance comparison and emissivity profiles for the chosen lava pixels. The AHI data is again shown in symbols and lines while the simulated black body data is

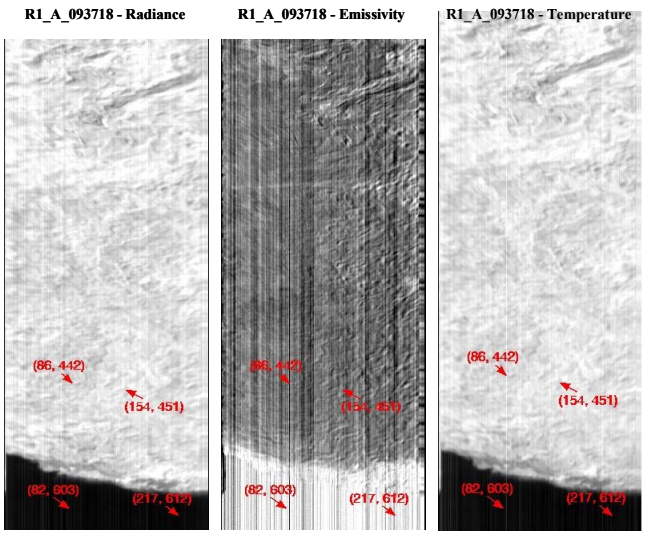

Figure 44. R1_A_093718 Emissivity and Temperature Images Generated By the Normalized Emissivity Method and the Corresponding Radiance Image

shown in a solid line only. In this case, the comparison produced some interesting results. One of the lava profiles (pixel 154, 451) demonstrated a reasonably good fit with the simulated black body, but the other profile (pixel 86, 442) clearly did not. This is a result of the fact that the normalized emissivity method chooses the temperature of a

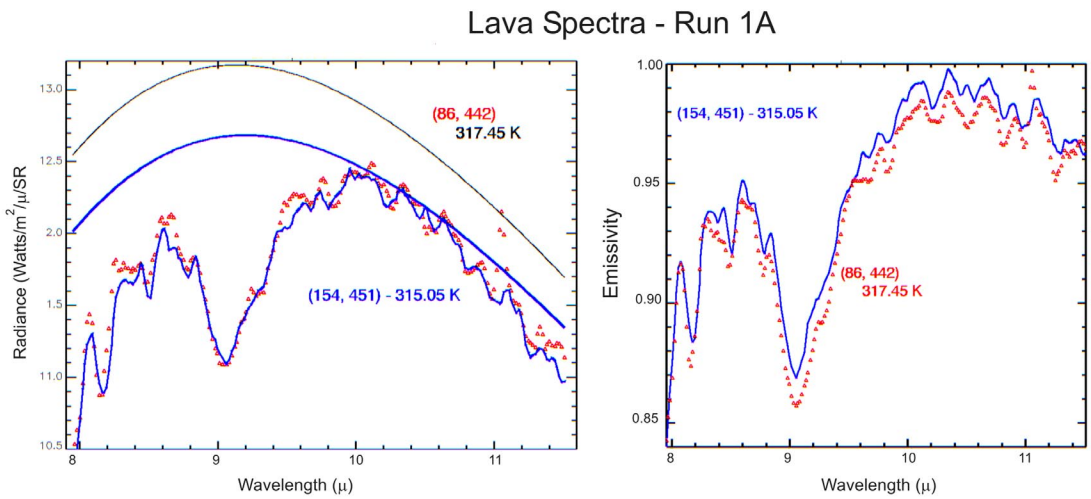

Figure 45. R1_A_093718 Black Body and AHI Radiance Comparison of Lava Pixels With Corresponding Emissivity Plot

pixel to be the highest temperature calculated in the method. There appear to be several anomalous data points near the 11 micron wavelength that force the temperature of the pixel to appear greater than it is in reality. The application of this falsely inflated temperature forces the blackbody profile to display significantly higher values than the data profile.

Figure 46 displays the radiance comparison profile for a 3 x 3 pixel average around the chosen water pixels. A similar effect of anomalous pixels is again readily seen in one of the profiles (pixel 217, 612). The anomaly of the second profile is

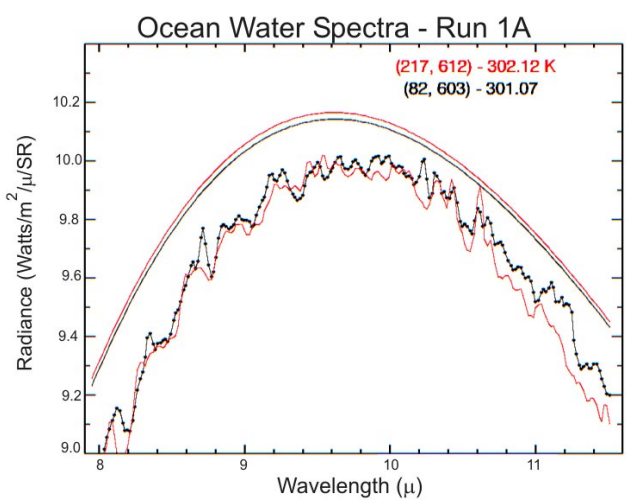

Figure 46. R1_A_093718 Black Body and AHI Radiance Comparison of Water Pixels

not as easily explained. Kealy and Hook do not recommend the normalized emissivity method for scenes which may contain a mixture of rocks/soils and vegetation/water. They conducted several experiments that showed the normalized emissivity method could be incorrect by as much as 2.02 degrees K in a case such as this one. (Kealy, P. and Hook, S., 1993, p. 1163) Some of the anomalies seen may be a direct result of the method used.

These comparisons provided additional insight to the effects of applying the normalized emissivity method to calculate the temperature and emissivity of the data segments. In general, it proved to be a reliable method for the R1_C_095349 image; however, it did not prove to be without fault. Keeping the possibility of anomalies in mind, the analysis of the data set was continued using the temperature and emissivity results generated by the normalized emissivity method.

b. Application of Spectral Classification Tools

The next area of analysis was to further develop knowledge gained from applying the decorrelation stretch to both the radiance and emissivity images. The goal was to use a spectral mapping tool to locate and map the other pixels within the images that displayed the SO_2 absorption feature. Two different mapping tools were applied in both radiance and emissive space: the Spectral Angle Mapper (SAM) and the Matched Filter (MF).

A principal component analysis (PCA) was applied to both the radiance and emissivity images before applying either the SAM or MF. A PCA is a very common method of decorrelating data that requires no *a priori* knowledge of the scene. The application of a forward principal component rotation produces a user-defined number of new image bands called principal components (PCs). These new bands generally do not have any real physical meaning, but represent linear combinations of the original spectral bands with enhanced contrast and variance. (Stefanou, M., 1997, p.48) Eight ROI's were selected using both the newly transformed PC image and the false color RGB TIMS image. These ROI's included pixels that were believed to be SO_2 and those that were not and are shown in the radiance image in Figure 47. These ROI's were used as endmember spectra for both the SAM and MF analysis.

The first algorithm which was then applied was the Spectral Angle Mapper (SAM), which operates by taking the dot product of each spectrum with a sequence of reference spectra. In this case, the reference spectra are defined by the ROI's

R1_C_095439 - ROI's

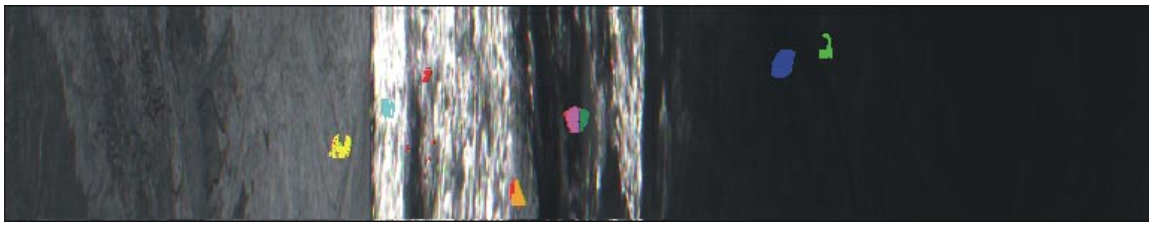

Figure 47. Regions of Interest Used in the Application of Spectral Mapping Tools

chosen from the PC images. These reference spectra and the image pixels are treated as vectors. The SAM compares the angle between these two vectors in a space with dimensionality equal to the number of image bands. If the angle between the vectors is small, the vectors are considered matched and of a similar class. A threshold angle can be chosen, and if the pixel vector does not fall within this angle in comparison to any of the reference vectors, the pixel will not be classified. (Research Systems Inc, 2001, p. 511)

The output of the SAM includes an all-encompassing color image that is classified according to the all of the chosen reference spectra and a number of gray-scale rule images that correspond to each of the individual reference spectra. The SAM, with a threshold angle of .10 radians, was applied to both the radiance and emissivity R1_C_095349 images employing the same eight ROI's for each. Figure 48 displays the classification images for radiance and emissivity. The black strips on the edges correspond to the anomalous pixel regions found in the emissivity displays illustrated above. In much of the analysis proceeding from this point, processing was restricted to an 800-line subset of the run, since there was no SO_2 outside this region. The red and orange areas in the classification results correspond to two classes of SO_2 and will be the primary focus for additional analysis. The other colors in the image correspond to regions with no obvious SO_2 signature. There are slight differences in the SAM results from the two versions of the data.

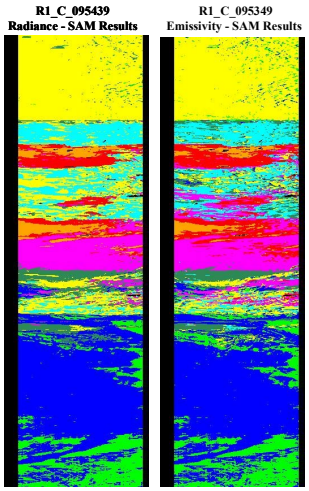

Figure 48. Initial SAM Results in Radiance and Emissive Space

Figure 49 displays the spectral angle in gray-scale form for the red and orange classes. The red class images are scaled from 0 to .11 radians (white to black) and

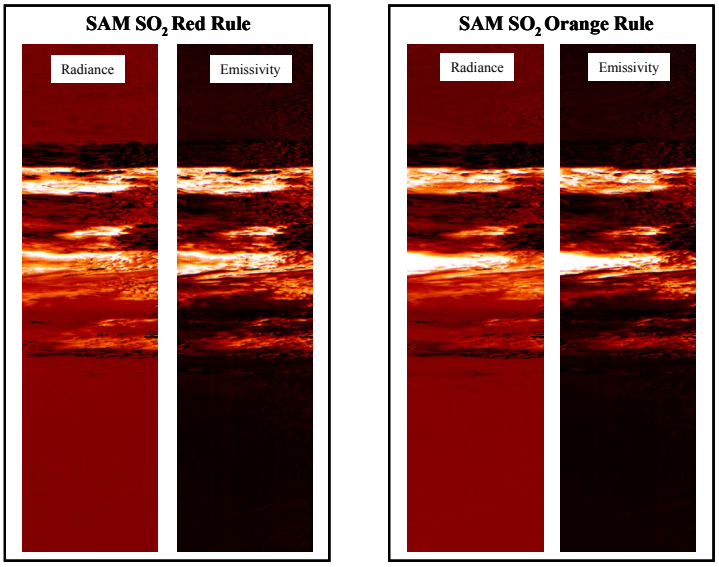

Figure 49. SAM Rule Images for Red and Orange SO2 Classes in Radiance and Emissive Space

the orange class images are scaled from 0 to .15 radians (white to black). Bright or white areas represent the presence of SO_2. Slight differences do appear in the rule images for both classes of SO_2. Scatter plots comparing the red and orange SO_2 rule image results in radiance and emissive space are displayed in Figure 50. The x and y axis are in units of spectral angles and represent the results for the radiance and emissive spaces

respectively. The smaller spectral angles represent good matches for that particular class of SO_2. The color contours of the plot represent the number of occurrences in each of the color areas. A first order linear fit is applied to the data points to show the relationship between the two spaces. A correlation factor is also calculated for the data. Although there are slight differences in the images, the results show a good linear relationship, and the correlation factor calculated for both classes is relatively high. As temperature plays a significant role in the SO_2 signature, these differences may stem from anomalies created

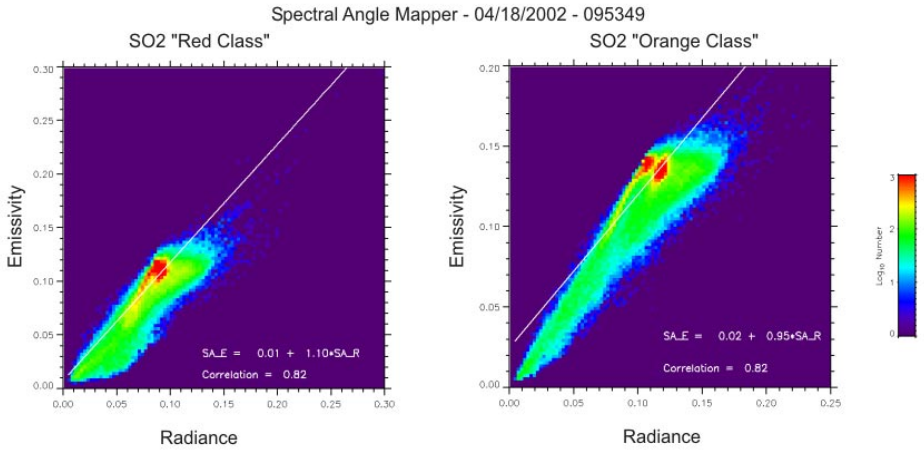

Figure 50. Scatter Plots of SAM SO_2 Rules in Radiance and Emissive Space for the Red and Orange SO_2 Classes, Correlation Coefficient For Both Classes = .82, Red Class Slope = 1.10, Intercept = .01, Orange Class Slope = .95, Intercept = .02

by the emissivity and temperature separation discussed earlier. The differences could also be an artifact of the classification tool used.

A second classifier, the Matched Filter (MF), was applied to see what sorts of dependence the above results had on the type of classifier being used. The technique is a vector projection method that uses the scene statistics, and a projection operator to distinguish the desired spectrum from the background. It is commonly used in the signal processing application. (Stefanou, M., 1997, p.87)

In this case, the MF is used to find matches in the scene for the eight ROI's employed in the SAM analysis. Each of the image pixels is compared to the reference ROI spectrum and a relative degree of match is assigned to each pixel. A perfect match is given the value of 1. The results for the red and orange classes are shown in Figure 51. Again, the classifier results have been scaled from dark to light,

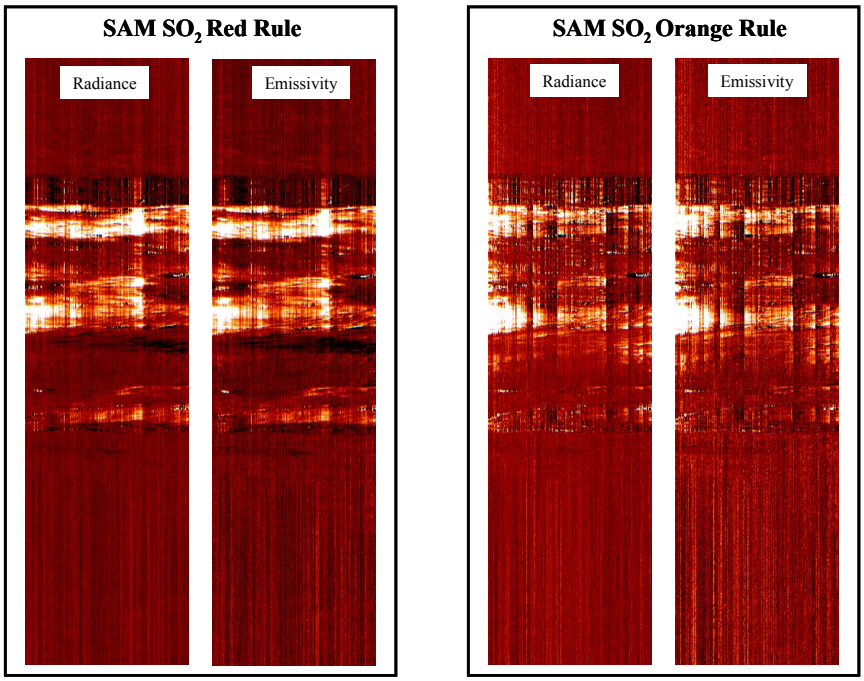

Figure 51. MF Gray-Scale Images for Orange and Red Classes of SO_2 in Radiance and Emissive Space

with high probability corresponding to white. The noticeable differences seen in the images between the radiance and emissive spaces using the SAM do not readily appear in the MF. The scatter plots displayed in Figure 52 support the apparent similarities

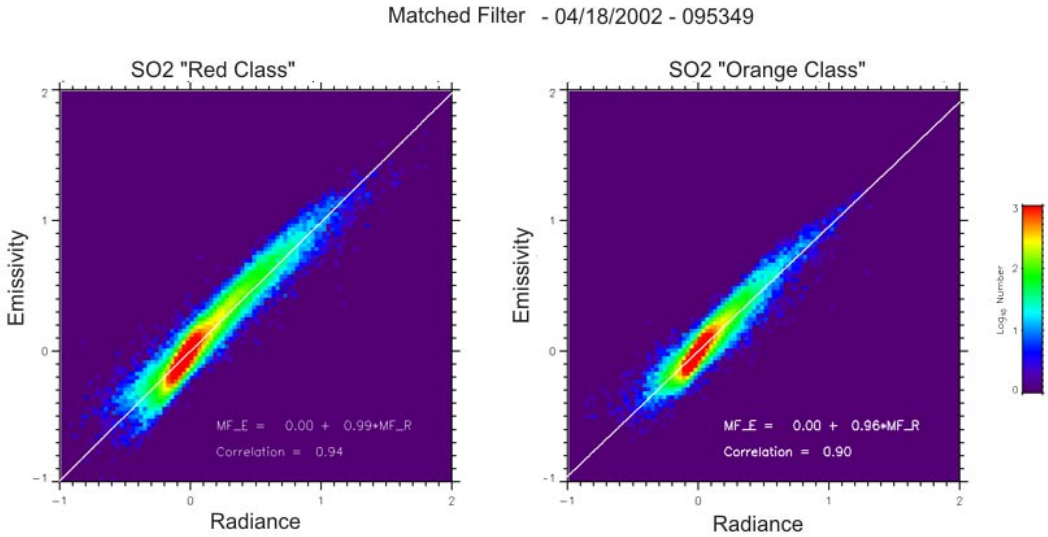

Figure 52. Scatter Plots of MF SO_2 Results in Radiance and Emissive Space for the Red and Orange SO_2 Classes, Red Class Correlation Coefficient = 0.94, Slope = 0.99, Intercept = 0, Orange Class Correlation Coefficient = .90, Slope = 0.96, Intercept = 0

between the classifications in radiance and emissive spaces using the MF. The x and y axis of the scatter plots are in units of "relative match" with 1 representing the best match to the orange or red class SO_2 reference spectra. The data show a strong linear relationship between the radiance and emissive space with a correlation factor that is almost 10% greater than that of the SAM results.

A final set of scatter plots are displayed to help directly compare and visualize this apparent difference in the performances of the two spectral mapping tools. The SO_2 SAM Rule results are plotted against the SO_2 MF results for both the radiance and emissive spaces. Figure 53 displays the scatter plots for both SO_2 classes in radiance

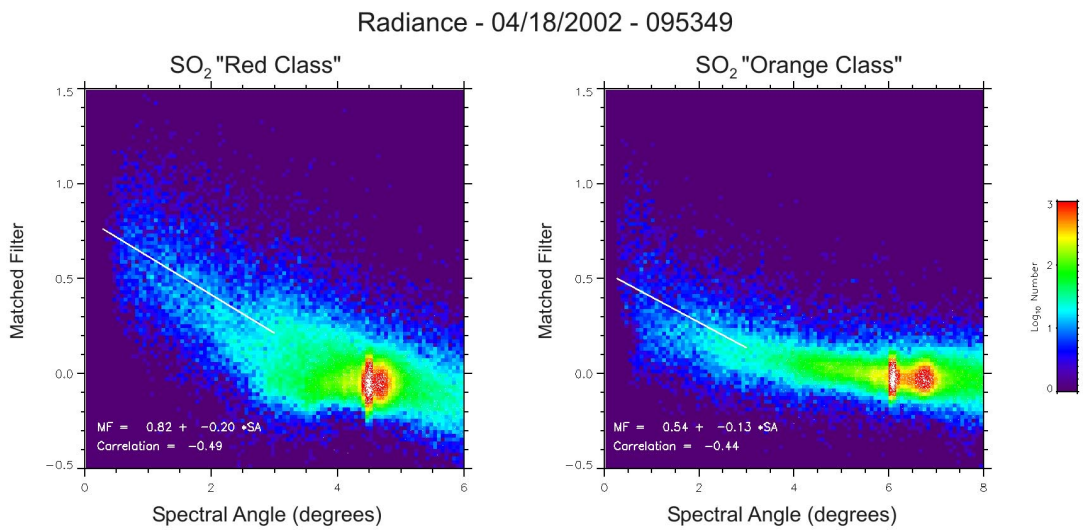

Figure 53. Scatter Plot of SAM and MF Results for SO_2 Classes in Radiance Space, Red Class Correlation Coefficient = -0.49, Slope = -0.20, Intercept = 0.82, Orange Class Correlation Coefficient = -0.44, Slope = -0.13, Intercept = 0.54

space. The best matches for SO_2 form the diagonal feature in the left portion of the scatter plot. These pixels are closest to 1 on the MF scale and have the smaller angles on the SAM scale. The color contours of the plot again indicate the number of occurrences within each of the color areas. The dense clusters on the right side of the plot are all of the occurrences of pixels not containing any SO_2. A first order linear fit is applied to the SO_2 pixels on the left side of the plot to determine the relationship between the SAM and

MF results. Although the data for both classes does maintain somewhat of a linear trend, the correlation factors are only at -.49 and -.44. It is also interesting to note the difference between the red and orange classes. These results support the differences in correlation factors between the radiance and emissive spaces in the earlier plots.

Figure 54 displays the scatter plot of SAM and MF results in emissive space for both the red and orange classes of SO_2. A first order linear fit is applied to the SO_2 pixels on the left side of the plot to describe the relationship between the SAM and MF results. The data shows somewhat of a linear trend, although the correlation factor is lower than it was in radiance space at -.37 and -.39. It is again interesting to note the differences between the two classes. The red class consistently produces higher correlation factors in each of the scatter plots. The differences seen in the spectral mapping of the red and orange classes encouraged additional analysis of the SO_2 class results.

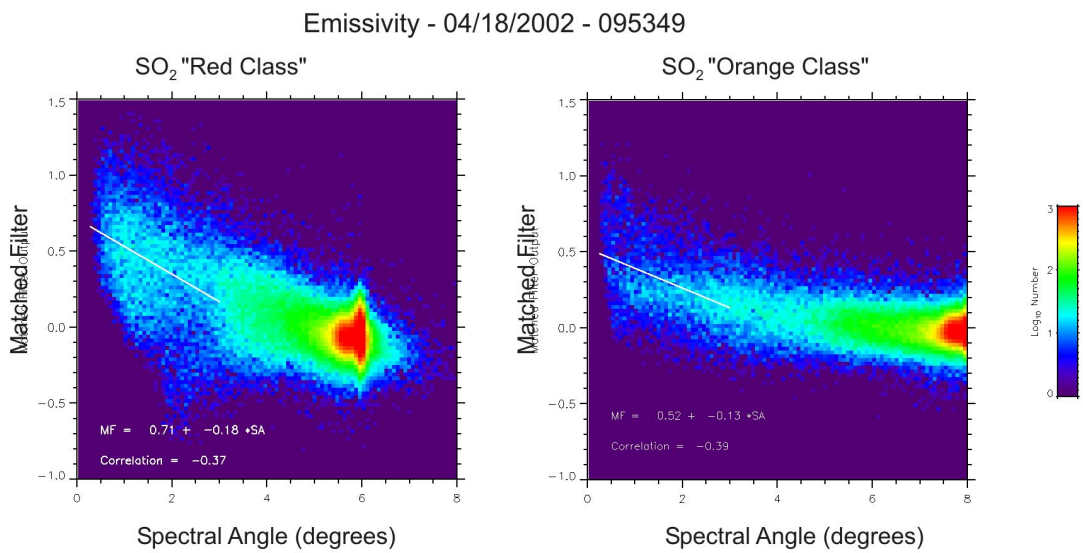

Figure 54. Scatter Plot of SAM and MF Results for SO_2 Classes in Emissive Space, Red Class Correlation Coefficient = -0.37, Slope = -0.18 Orange Class Correlation Coefficient = -0.39, Slope = -0.13, Intercept = 0.52

3. Development of Spectral Libraries.

In addition to using the spectral classification tools, the red and orange SO_2 classes are examined in Environment for Visualizing Images' (ENVI's) n-Dimenaional

(n-D) Visualizer with hopes of improving the understanding of the differences made apparent in the SAM and MF analysis. The n-D Visualizer allows a user to create scatter plots of selected data in n-dimensions where "n" is the number of bands. The user can interactively rotate selected data in n-Dimensions gaining new insight to the composition of the data, with the opportunity of refining selected classes or ROI's.

The initial red and orange SO_2 classes were examined in both radiance and emissive space. Using the PC band radiance and emissivity images, the red and orange SAM SO_2 ROI data were exported to the n-D Visualizer. Six spectrally distinct classes of SO_2 were developed. Each class was assigned a different color and had different numbers of pixels that belonged to them. Table 11 is a summary of the different classes and states how many pixels were assigned to each through the analysis process.

Figure 55 is a 2-D scatter plot using PC bands 1 and 2 in radiance space. The x-axis of the scatter plot, corresponding to PC band 1, represents average brightness with brightest pixels in the ROI on the right. The upper left hand corner shows a cluster of blue pixels representing the coolest and darkest class of SO_2 pixels in the scene. The green and cyan pixels on the right end of the scatter plot represent the warmest and brightest classes of SO_2 pixels in the scene.

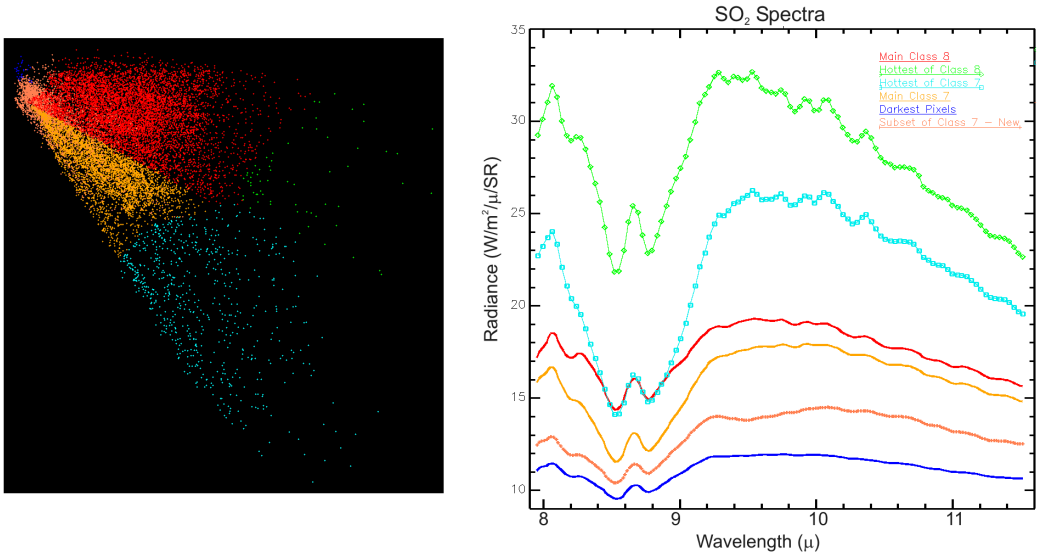

Figure 55. 2-D Scatter Plot of SO2 Classes in Radiance Space Using PC Bands 1 and 2 and the Corresponding Radiance Spectral Library of the SO_2 Classes

A spectral library was generated from these six classes of SO_2. The spectral library helps illustrate the differences between the classes in numeric form and maintain records for future analysis. The profiles for the SO_2 radiance spectral library are displayed in Figure 55. The profiles reinforce the fact that there is clear separation between each of the classes. The brightest or warmest pixels display radiance values as high as 25 to 33 $W/m^2/sr/\mu$ while the darkest or coolest pixels display radiance values between 11 and 13 $W/m^2/sr/\mu$.

Figure 56 is a 5-D scatter plot using the first five PC bands in emissivity space. The distinction between the classes is more difficult to make using the n-D Visualizer in emissivity space; however, the spectral library profiles, also displayed in Figure 56, again demonstrate a clear separation of the SO_2 classes. It is interesting to note where the classes of pixels fall in the emissivity space. The warmest and coolest classes in radiance space also fall at either end of the emissivity plot. However, the middle region displays information worth noting. In radiance space, the green class of

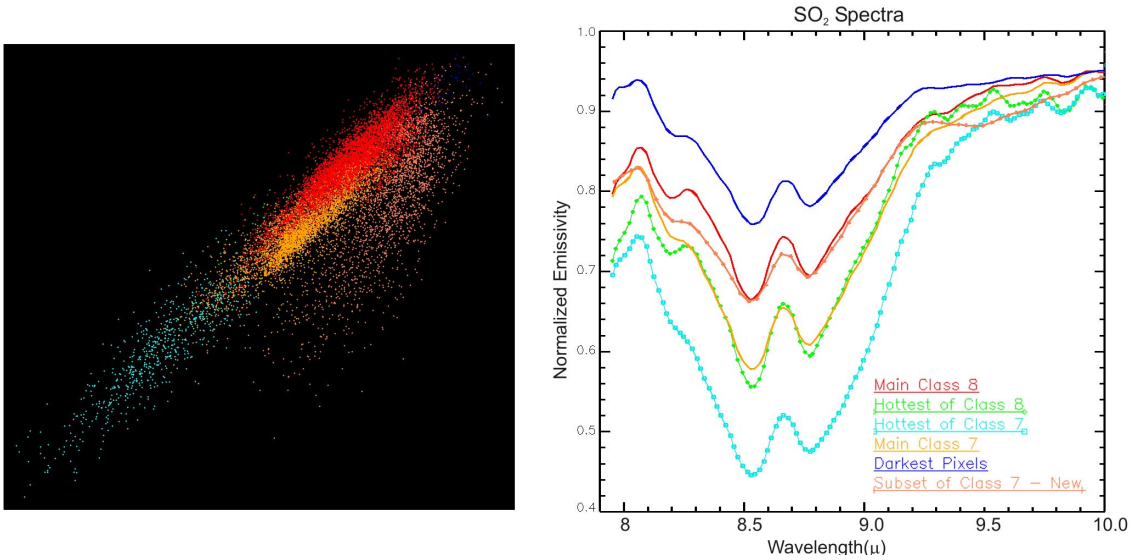

Figure 56. 5-D Scatter Plot of SO2 Classes in Emissivity Space Using the First Five PC Bands and the Corresponding Emissivity Spectral Library of the SO_2 Classes

pixels appear to be a warmer subset of the red class. In emissivity space, the green class appears to have emissive characteristics similar to the orange class. The coral class

appears to be a subset of the orange class in radiance space. While in emissive space, it takes on characteristics similar to the red class.

In both emissive and radiance space, the prominent difference noted between the classes is a y-axis offset from one another. This offset is partially explained in temperature differences. The six ROI classes were applied to the R1_C_095349 temperature image and statistics were computed for each class. These statistics are compiled in Table 11. Although there is some overlap in temperature ranges between the

Class Color	Class Size (points)	Min Temp (K)	Max Temp (K)	Mean Temp (K)	Stdev
Green	64	384.41	425.41	398.84	12.01
Cyan	649	357.12	425.80	380.02	13.71
Red	7226	318.81	398.07	350.08	14.62
Orange	4083	319.72	377.34	345.09	11.64
Orchid	1911	314.28	373.10	329.07	11.30
Blue	32	311.80	319.11	315.19	1.99

Table 11. SO_2 Class Temperature Statistics

classes, each class has a distinct mean. The orange and red classes show the smallest difference between classes with a 5-degree separation between their temperature means. The red class displays the largest range of temperatures and largest standard deviation,

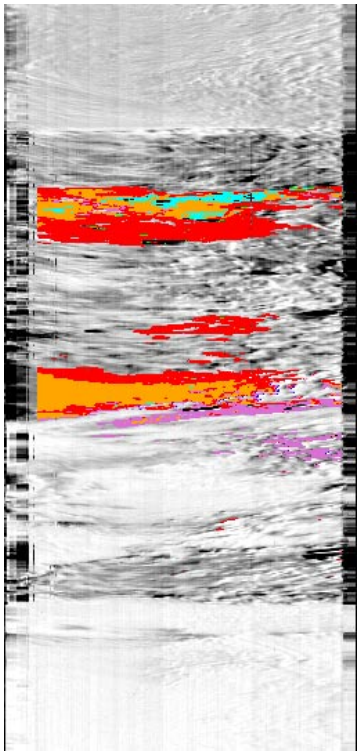

Figure 57. R1_C_095349 Radiance Image With Final SO_2 Classes Annotated

while the blue class displays the smallest temperature range and smallest standard deviation. These results further emphasize the importance of the temperature and emissivity determination. The temperature has a significant impact on the spectra observed when SO_2 is present. Finally Figure 57 displays the six SO_2 classes on a radiance image of R1_C_095349. It should be noted that the coral class described in the spectral library figures is annotated as orchid in Figure 57 and in all future analysis. Figure 57 is the summary figure for the first goal of the AHI data analysis displaying the results of the SO_2 detection. These six classes are used as a starting point for the second goal of attempting to quantify the amount of SO_2 detected.

C. SUMMARY OF SO_2 DETECTION

In summary, the three areas of SO_2 detection included: initial detection, applying spectral classification analysis tools, and developing a spectral library of SO_2 profiles. SO_2 was initially detected by applying a decorrelation stretch to AHI data that was resampled to create a simulated TIMS image. This produced a false color RGB image in which any presence of SO_2 was identified by yellow colored pixels. The decorrelation stretch image was used as a visual aid to select several ROI's in the image chosen for analysis. Some ROI's included SO_2 while others did not. Applying the SAM and MF to the ROI's created two distinct classes of SO_2 represented in colors of orange and red. The red and orange classes were then further analyzed in ENVI's n-D Visualizer resulting in six final classes of SO_2 that are used as a starting point for the second goal of attempting to quantify the amount of SO_2 detected.

V. QUANTIFICATION OF SO_2 DETECTIONS

As stated in Chapter IV, the analysis of AHI data was approached with two goals in mind. The first goal, addressed in Chapter IV, detected an SO2 plume in one of the images collected and classified the plume into six spectrally distinct classes of SO2. The second goal, to be addressed in this chapter, is to quantify the amount of SO2 in these SO2 classes. While detection was performed in both radiance and emissive space, radiance space is the primary focus for quantification.

As discussed in Chapter III, the process used by Realmuto et al. to determine the amount of SO_2 in the plume is based on an underdetermined radiance equation. The equation is given in Chapter III and has two unknown variables of temperature and SO_2 concentration. The method used to solve this equation for the AHI data is similar to the method used by Realmuto in that it is based on a comparison of the sensor generated radiance profiles and radiance profiles generated by MODTRAN. Details of the method are discussed in the following paragraphs.

A. MODTRAN

1. Inputs

The basic inputs for the MODTRAN code consist of four main "cards" or lines of FORTRAN code. Each card defines a different portion of the radiance equation. The first card addresses the atmospheric conditions. MODTRAN has six model atmospheric profiles that can be used for inputs. They are specified according to latitudinal sections of the globe and season of the year. Users can also define their own atmospheric profile for a specific situation. A combination of these two options is used in the AHI data analysis. The first card also contains an input for the ground surface temperature that has significant impact on the analysis problem. The temperatures determined by the normalized emissivity method are the temperatures initially applied to this variable for analysis.

The second card allows the user to define an atmospheric profile. A number of layers for the user-defined profile are chosen, and each layer is described according to temperature, pressure, relative humidity, and atmospheric constituents, which include

SO_2. For the AHI data analysis, four layers were developed. The initial layer is developed from the ground to the altitude of the top of the plume. The temperature, pressure, and relative humidity of this layer are taken from the weather reports from the Hilo weather station during the hours of collection. This is also the layer where the SO_2 concentration of the plume is defined. Two important assumptions relating to the SO_2 plume are made in the development of this layer. First, an assumption is made regarding the altitude and the thickness of the plume. As R1_C_095349 is an image collected directly over the vent, it is assumed that the altitude of the plume is at the surface of the vent or the very bottom layer in the atmospheric profile. As no direct measurements on the thickness of the plume were collected, an estimate of 150 m is used. Second, it is assumed that the temperature of the plume is in thermal equilibrium with the particular layer of the atmosphere in which it is described. The remaining three layers of the model are divided between the top of the plume and the altitude of the sensor. The standard atmospheric model is used to define the temperature, pressure, relative humidity, and atmospheric constituents of these layers. An example set of cards with all of the input parameters used in the AHI data analysis is found in Appendix B.

2. Outputs

MODTRAN generates several output files detailing the model inputs and the solution to the radiance equation from the ground to the sensor. The output file describing the radiation observed at the model sensor is used for the comparison to the AHI data. This output file consists of the range of operating wavelengths for the model sensor and the corresponding radiance seen at each of the wavelengths. The first output generated with the model used for the AHI analysis is displayed in Figure 58. It is the default atmospheric radiance profile with a ground surface temperature of 288 K and no SO_2 applied.

3. MODTRAN Model Examples

Prior to starting any comparisons with AHI data, several test models were run modifying the general input parameters to be used in analysis. Many of the variances and sensitivities tested are described in Chapter III such as plume altitude, plume thickness, and model atmospheres. There were no significant differences in the sensitivity results of the model to report.

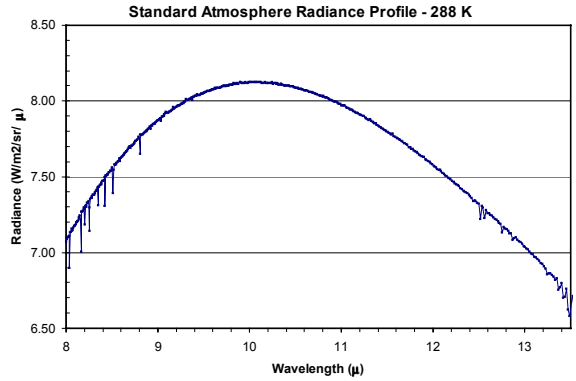

Figure 58. MODTRAN Standard Atmospheric Profile

During analysis, the only two input parameters of the MODTRAN code that are modified are the ground surface temperature and the SO_2 concentration. Several test runs were conducted varying the SO_2 concentrations for two ground surface temperatures (350 K and 380 K) chosen from the mean temperature statistics of the six SO_2 classes identified in Table 11. SO_2 concentrations from 0 to 1600 ppm in intervals of 400 ppm were applied to both temperatures. The results for both temperatures are displayed in Figure 59. The resolution of the general MODTRAN model is much higher than the resolution of AHI. The individual data points are included in the figures; however, a

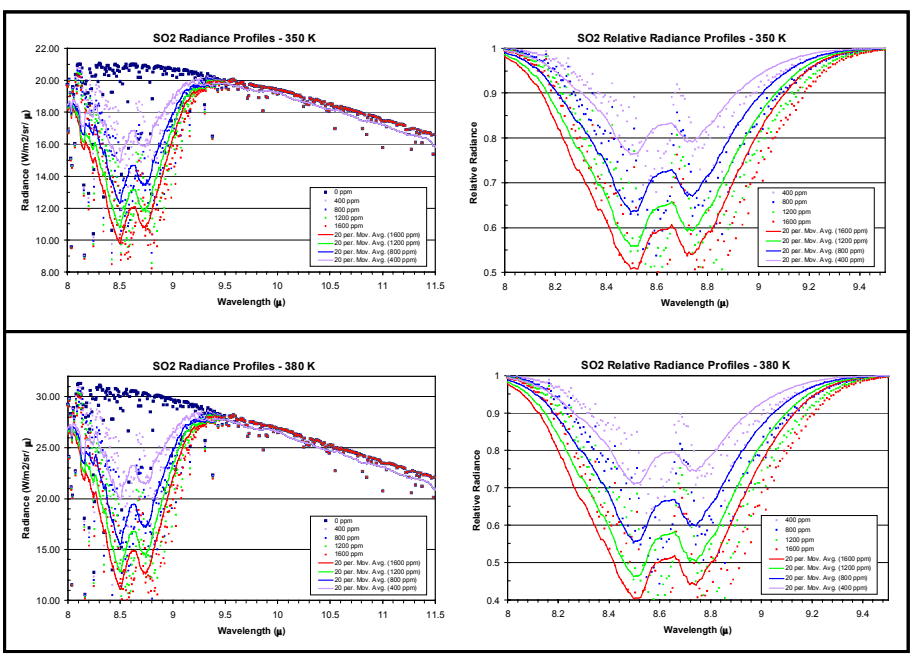

Figure 59. MODTRAN Radiance and Relative Radiance Model Profiles for Multiple Concentrations of SO_2 at 350 K and 380 K

running average, displayed as a solid line, is applied to each of the profiles in order to simplify the display and discussion of the data. In addition to the general radiance profile, dividing each of the profiles containing SO_2 by the SO_2 free profile also generated relative radiance profiles. It is interesting to compare the relative radiance profiles for the two ground temperatures. The higher temperature of 380 K produces relative radiances of 5 to 10 percent lower than the temperature of 350 K with equivalent concentrations of SO_2. In other words, with higher ground temperatures, less SO_2 is required to produce the same amount of absorption seen at lower ground temperatures. This is a direct demonstration that reemphasizes the importance of the ground temperature and emissivity separation conducted earlier in the analysis process. This exercise also improves the understanding of the model and its sensitivities to the varying input parameters, and establishes a reference point for the beginning analysis.

B. AHI DATA CHOSEN FOR ANALYSIS

Several pixel block areas from each of the six classes of SO_2 were chosen for analysis. Initially, individual pixels were chosen based on ground temperature and location. The determined ground temperatures of the chosen pixels are within one standard deviation of the mean for the class, according to the statistics calculated in Table 11. They are also located in an area where they are surrounded by pixels of the same class. This provided the opportunity to form blocks of same class pixels to be used in generating a pixel averaged radiance profile. These pixel averaged radiance profiles are used in the analysis comparison with the MODTRAN radiance profiles. Table 12 lists the pixel blocks chosen for analysis, along with the individual pixels' temperature determined through the normailized emissivity temperature and emissivity separation analysis method in Chapter IV. The individual pixels' temperatures provided a starting point for the MODTRAN analysis. Figure 60 displays a spatially subsetted image of R1_C_095349 focusing on the six classes of SO_2 in the plume. The corner x-y coordinates of the chosen pixel blocks are annotated.

A MODTRAN profile was generated using the pixel ground temperatures and an estimated SO_2 concentration. The MODTRAN output was plotted against the AHI pixel block profiles. The profiles were initially examined for fit in the longer wavelength region (9.5 – 11.5 μ). This region is unaffected by SO_2 and can be used to examine the

profile in terms of temperature. Adjustments to the ground surface temperature input were made if an ideal fit was not observed. After a proper fit was established in the

Class Color	Class Size (points)	Pixel Block Size	Pixel Block Location	Class Mean Temp	Emiss Norm Temp (K)
Red	7226	5 x 5	87, 534	350.08	350.98
Red	7226	5 x 5	161, 603	350.08	350.56
Red	7226	5 x 5	52, 635	350.08	350.33
Red	7226	5 x 5	51, 660	350.08	348.40
Red	7226	5 x 5	88, 638	350.08	346.49
Red	7226	5 x 5	154, 637	350.08	337.72
Red	7226	5 x 5	39, 528	350.08	345.00
Red	7226	5 x 5	115, 534	350.08	367.61
Red	7226	5 x 5	166, 528	350.08	364.59
Orange	4083	5 x 5	60, 503	345.09	350.47
Orange	4083	5 x 5	141, 513	345.09	344.38
Orange	4083	5 x 5	98, 513	345.09	344.95
Orange	4083	5 x 5	66, 648	345.09	344.72
Orange	4083	5 x 5	103, 646	345.09	352.89
Orange	4083	5 x 5	81, 646	345.09	354.34
Orange	4083	5 x 5	35, 646	345.09	356.48
Orchid	1911	6 x 3	140, 664	329.07	329.77
Orchid	1911	6 x 3	210, 687	329.07	329.73
Orchid	1911	6 x 3	84, 671	329.07	318.47
Cyan	649	6 x 3	38, 517	380.02	380.27
Cyan	649	6 x 3	145, 511	380.02	382.28
Cyan	649	6 x 3	137, 521	380.02	388.63
Green	64	4 x 1	83, 522	398.84	403.11
Green	64	8 x 1	212, 503	398.84	396.81
Blue	32	2 x 1	184, 653	315.19	315.04
Blue	32	2 x 1	199, 649	315.19	313.34
Blue	32	1 x 1	99, 660	315.19	317.74

Table 12. AHI Pixel Data Chosen for Analysis

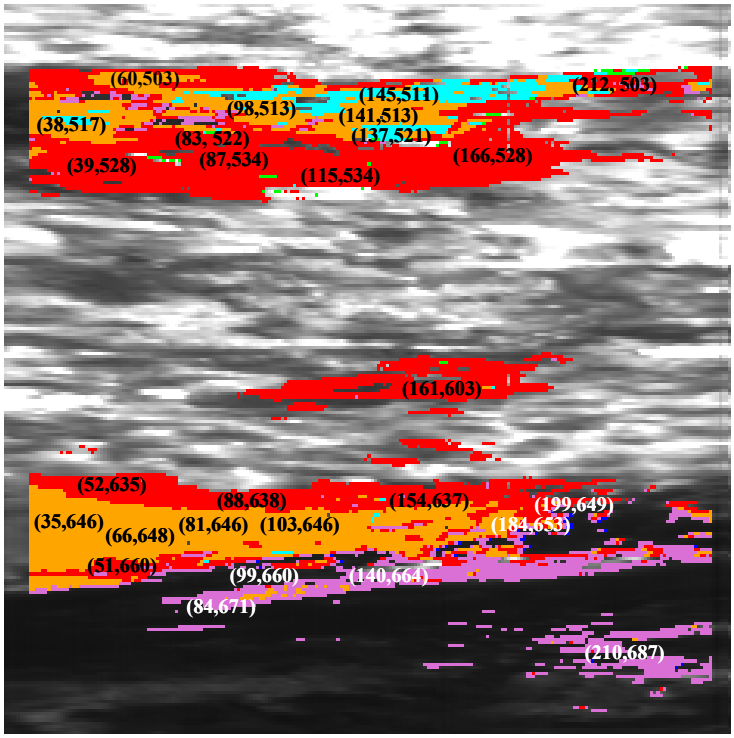

Figure 60. X-Y Coordinates of Pixel Blocks in the Plume Chosen for Analysis

longer wavelengths, the SO_2 concentration was adjusted to develop the best fit to the SO_2 signature seen in the AHI data. Comparison plots were generated for each of the pixel locations indicated in Table 12.

C. AHI DATA ANALYSIS RESULTS

As shown in Figure 60, there are two main sections of SO_2. They are referred to as the upper and lower plume in the analysis discussion. The analysis results provide interesting comparisons both within and between the classes. The results are initially presented by class. A table highlighting maximums and minimums is presented in the individual sections along with a portion of the comparison plots that were generated. The MODTRAN model has a much higher spectral resolution than the AHI data so a 20-point running average is applied to all of the MODTRAN results. This is believed to contribute to a small leftward offset observed between the two datasets. A summary table and figure at the end of this section provides a combined numeric overview of all of the class results. A full collection of all of the plot results is found in Appendix C.

1. SO_2 Class Results

a. Red Class

As the red class is the largest of the six classes, nine blocks of pixels were chosen for analysis. Each of the blocks is a 5 x 5 average of pixels. The red class is

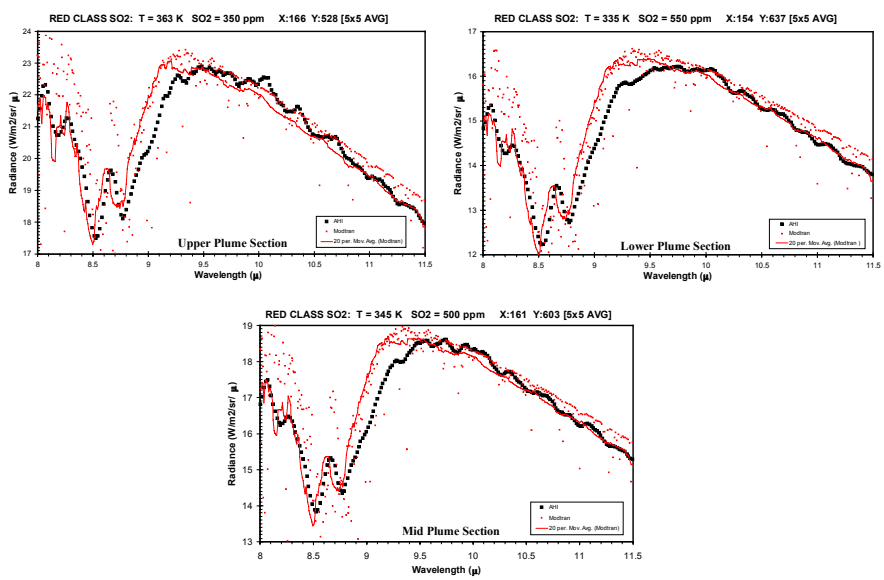

Figure 61. Upper, Lower, and Mid Plume Section AHI – MODTRAN Comparison Plots for the Red Class, Black = AHI data, Red = Modtran Model With 20 Point Running Average Applied

found in both the upper and lower sections of the plume. It also comprises a majority of a small mid section of the plume. The nine pixel blocks chosen for analysis are dispersed throughout these three sections of plume. Plot results from three of the blocks (one from each section of the plume) are displayed in Figure 61. The plots demonstrated a reasonably good fit between the MODTRAN model and AHI data. Table 13 lists the maximum and minimum ground temperatures found in the red class and the sections of the plume in which they are found. All of the red class temperatures analyzed fall within one standard deviation

Red Class SO2	deg K or ppm	Plume Section
Max Temp	363 K	Upper
Min Temp	335 K	Lower
Max SO2	725 ppm	Lower
Min SO2	325 ppm	Lower

Table 13. Maximum and Minimum Temperature and SO_2 Results for the Red Class

of the class mean according to the statistics computed earlier. Although a large range of temperatures is created by the maximum and minimum results, a majority of the temperatures actually fell between 345 and 355 K. The ground temperatures in the upper plume appeared slightly higher than those in the lower section of plume. There did not appear to be a particular trend with the SO_2 in either section of the plume. The SO_2 found in the red class cover ranges spanning 300 to 400 ppm in the upper and lower sections of the plume respectively. Comparing all of the class results, the red class displays the lowest values in SO_2 concentration.

b. Orange Class

The orange class is roughly half the size of the red class and has a large presence in both the upper and lower sections of the plume. Seven pixel blocks, each 5 x 5 pixel averages, were plotted against the MODTRAN model. One plot from each section of the plume is displayed in Figure 62. The plots show reasonably good agreement with the MODTRAN model. Table 14 gives the maximum and minimum ground temperature and SO_2 results for the class. All of the temperatures analyzed fall within one standard deviation of the mean temperature calculated in earlier statistics.

Although smaller than the red class, the orange class is at least twice the size of the other classes, and it displayed a much smaller

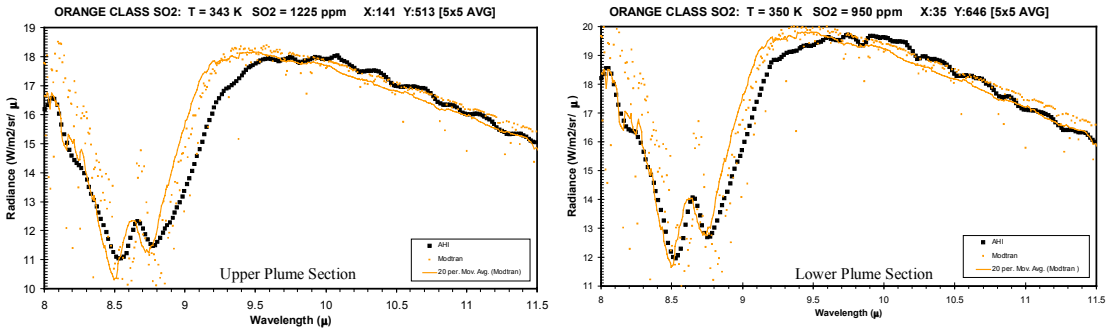

Figure 62. Upper and Lower Plume Section AHI – MODTRAN Comparison Plots for the Orange Class, Black = AHI Data, Orange = Modtran Model Data with 20 Point Running Average Applied

variance in ground temperatures than the red class. Temperatures appear slightly lower in the upper section of plume, while the SO_2 results are significantly lower in the lower portion of the plume. Overall the SO_2 results also displayed a smaller variance than the red class with ranges spanning only 100 to 200 ppm in the lower and upper plume sections respectively.

Orange Class SO2	deg K or ppm	Plume Section
Max Temp	350 K	Lower
Min Temp	343 K	Upper
Max SO2	1400 ppm	Upper
Min SO2	850 ppm	Lower

Table 14. Maximum and Minimum Temperature and SO_2 Results for the Orange Class

c. Orchid Class

As noted in the initial development of the classes, the orchid class appears

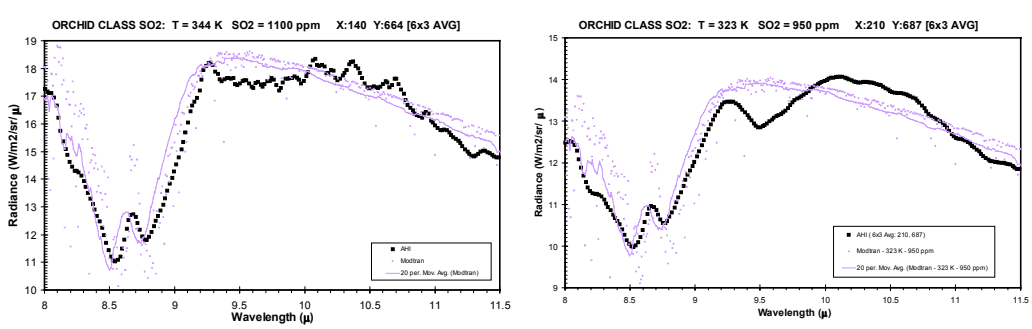

Figure 63. Lower Plume Section AHI – MODTRAN Comparison Plots for the Orchid Class

to be a cooler or darker subset of the orange class. The orchid class is roughly half the size of the orange class and is only found in the lower plume section. Three pixel block averages, each 6 x 3 pixel averages, were compared with the MODTRAN model and show a reasonably good fit. Two of the comparison plots are displayed in Figure 63. The orchid class shows a large ground temperature range in the results just as the red class did. The maximum and minimum temperature and SO_2 results are listed in Table 15. Although all of the ground temperature results fall within the maximum and minimum temperature range calculated in the statistics, the maximum temperature result is slightly outside of one standard deviation of the mean calculated for the class. Two of the three orchid plots display lower ground temperatures than both the red and orange classes within the lower section of the plume. All of the plots display higher SO_2 results

Orchid Class SO2	deg K or ppm	Plume Section
Max Temp	344 K	Lower
Min Temp	317 K	Lower
Max SO2	1275 ppm	Lower
Min SO2	950 ppm	Lower

Table 15. Maximum and Minimum Temperature and SO_2 Results for the Orchid Class

than the red and orange classes. The SO_2 results are closer in value to the orange class results in the upper plume section. This similarity reflects the fact that it initially evolved as a subset of the orange class.

d. Cyan Class

The cyan class initially evolved as a hotter or brighter subset of the orange class. The cyan class is a third of the size of the orchid class and is only located in the

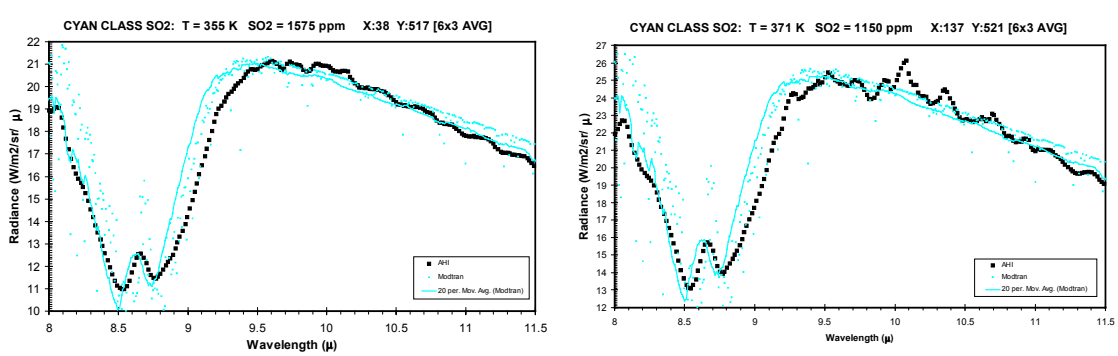

Figure 64. Upper Plume Section AHI – MODTRAN Comparison Plots for the Cyan Class

upper plume section. Three pixel block averages, each 6 x 3 pixel averages, are compared with the MODTRAN model and show a reasonably good fit. Two of the comparison plots are displayed in Figure 64. The cyan class has a substantially higher mean ground temperature than the other classes. However the range of ground temperatures in the results is moderate in comparison with the other classes. The maximum and minimum temperature and SO_2 results are displayed in Table 16. The temperatures of the chosen pixel blocks all fall at least 10 degrees below the calculated mean temperature but are still higher than those found in the orange class. The SO_2 results display the highest values seen in all of the classes and are again on the order of those seen in the orange class reinforcing the fact that it evolved as a subset of the orange class.

Cyan Class SO2	deg K or ppm	Plume Section
Max Temp	371 K	Upper
Min Temp	355 K	Upper
Max SO2	1600 ppm	Upper
Min SO2	1150 ppm	Upper

Table 16. Maximum and Minimum Temperature and SO_2 Results for the Cyan Class

e. Green and Blue Classes

The green and blue classes are very small classes in comparison to the others and hence are presented together. The green class is found mainly in the upper plume section, while the blue class is found mainly in the lower plume section. They both appear randomly in their respective plume sections in groups of pixels numbering as large as eight and as small as one.

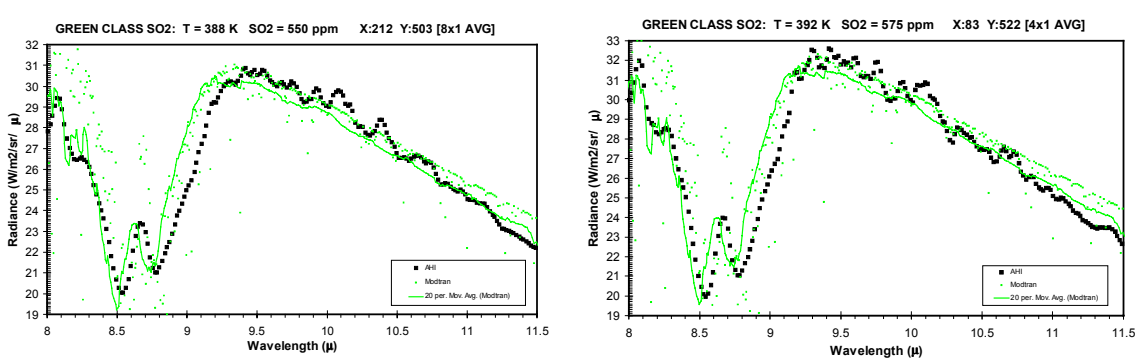

Figure 65. Upper Plume Section AHI – MODTRAN Comparison Plots for the Green Class

The green class initially evolved as a subsection of the hottest and brightest pixels in the red class. Only two pixel block comparisons are made with the MODTRAN model and both demonstrate reasonably good fits. These plots are displayed in Figure 65. The temperatures are within one standard deviation of the mean temperature calculated in the statistics. The green class displays the highest ground temperature values seen in all of the classes. The SO_2 results are closer to those of the red class reinforcing its evolution from that class. The maximum and minimum ground temperature and SO_2 results for the green class are given in Table 17.

Green Class SO2	deg K or ppm	Plume Section
Max Temp	392 K	Upper
Min Temp	388 K	Upper
Max SO2	575 ppm	Upper
Min SO2	550 ppm	Upper

Table 17. Maximum and Minimum Temperature and SO_2 Results for the Green Class

The blue class is the smallest of all classes and originally evolved as the very coolest or darkest pixels in the scene. This is verified with the comparison plots. Three pixel blocks are plotted against the MODTRAN model and two of them are displayed in Figure 66. The comparison shows a reasonably good fit between the model

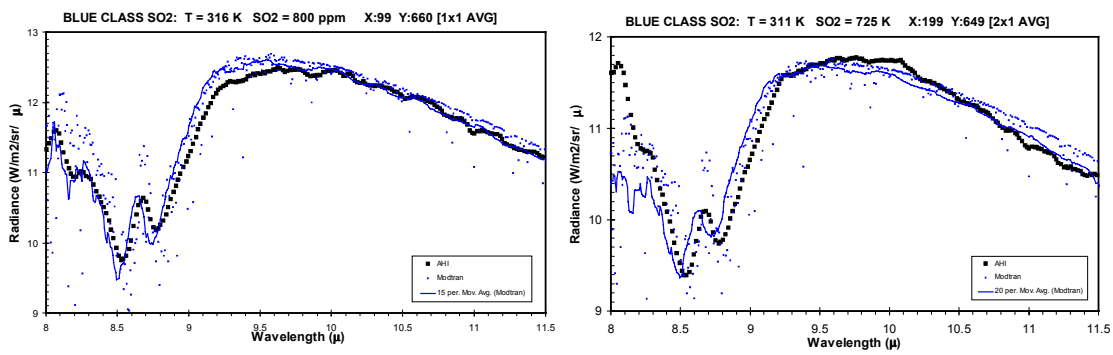

Figure 66. Lower Plume Section AHI – MODTRAN Comparison Plots for the Blue Class

and the data. The temperature range calculated in the statistics is very small and all of the results are within this range, but only one of them is within one standard deviation of the mean. The ground temperature results are the lowest of all the classes. The SO_2 results fall roughly between the red and orange classes. Although not quite as high, they appear

closer in value to those of the orange class. The maximum and minimum ground temperature and SO_2 results for the blue class are given in Table 18.

Blue Class SO2	deg K or ppm	Plume Section
Max Temp	316 K	Lower
Min Temp	311 K	Lower
Max SO2	800 ppm	Lower
Min SO2	725 ppm	Lower

Table 18. Maximum and Minimum Temperature and SO_2 Results for the Blue Class

f. Class Summary

Figure 67 is a summary of all of the class results. It is the same picture shown earlier with the X-Y coordinates of the pixel blocks, but in this case, the coordinates are the ground surface temperature and SO_2 concentration inputs that produced the best fitting MODTRAN model to the data profile at each of the pixel block points. These results are also summarized in a table format in Table 19.

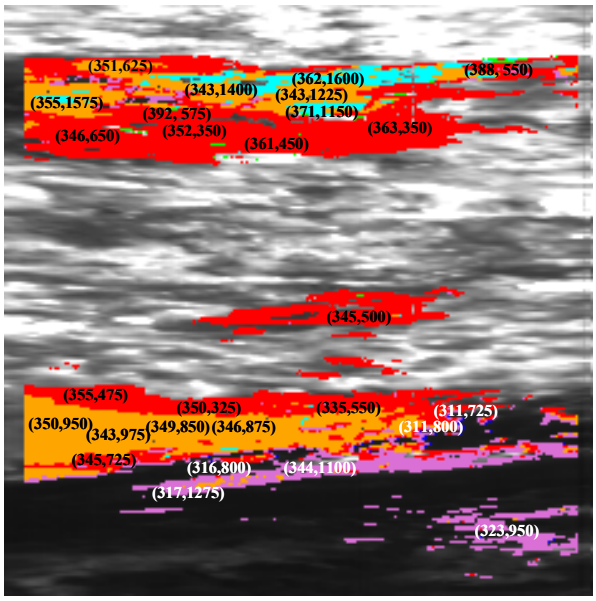

Figure 67. Summary of MODTRAN Ground Surface Temperatures and SO_2 Concentrations Producing the Best Fit to Corresponding AHI Data

As all of the results are visualized as a whole, it appears that the upper plume section has warmer ground surface temperatures and has higher SO_2 values than the lower section. The red class appears to maintain relatively consistent ground temperatures and SO_2 values in all sections of the plume; however this is not the case with the orange class. It is interesting to note that while the orange class maintains very

consistent ground temperatures, there appears to be a large difference in the SO_2 values between the upper and lower plume sections.

Several different theories might explain the wide range in ground temperatures and SO_2 values seen in the data. These values may largely be an artifact of directly imaging the vent source. It is apparent from the visible image in the beginning of the chapter that the plume thickness and density is quite variable at the source. The fact that there was little to no wind on the day of collection increases this effect. Realmuto et al. saw some of this phenomenon in their studies and labeled it "puffing" within the

Class Color	Class Size (points)	Pixel Block Size	Pixel Block Location	Plume Section	Class Mean Temp (K)	Emiss Norm Temp (K)	Modtran Temp (K)	Modtran SO2 (ppmv)
Red	7226	5 x 5	87, 534	Upper	350.08	350.98	352	350
Red	7226	5 x 5	161, 603	Mid	350.08	350.56	345	500
Red	7226	5 x 5	52, 635	Lower	350.08	350.33	355	475
Red	7226	5 x 5	51, 660	Lower	350.08	348.40	345	725
Red	7226	5 x 5	88, 638	Lower	350.08	346.49	350	325
Red	7226	5 x 5	154, 637	Lower	350.08	337.72	335	550
Red	7226	5 x 5	39, 528	Upper	350.08	345.00	346	650
Red	7226	5 x 5	115, 534	Upper	350.08	367.61	361	450
Red	7226	5 x 5	166, 528	Upper	350.08	364.59	363	350
Orange	4083	5 x 5	60, 503	Upper	345.09	350.47	351	625
Orange	4083	5 x 5	141, 513	Upper	345.09	344.38	343	1225
Orange	4083	5 x 5	98, 513	Upper	345.09	344.95	343	1400
Orange	4083	5 x 5	66, 648	Lower	345.09	344.72	343	975
Orange	4083	5 x 5	103, 646	Lower	345.09	352.89	346	875
Orange	4083	5 x 5	81, 646	Lower	345.09	354.34	349	850
Orange	4083	5 x 5	35, 646	Lower	345.09	356.48	350	950
Orchid	1911	6 x 3	140, 664	Lower	329.07	329.77	344	1100
Orchid	1911	6 x 3	210, 687	Lower	329.07	329.73	323	950
Orchid	1911	6 x 3	84, 671	Lower	329.07	318.47	317	1275
Cyan	649	6 x 3	38, 517	Upper	380.02	380.27	355	1575
Cyan	649	6 x 3	145, 511	Upper	380.02	382.28	362	1600
Cyan	649	6 x 3	137, 521	Upper	380.02	388.63	371	1150
Green	64	4 x 1	83, 522	Upper	398.84	403.11	392	575
Green	64	8 x 1	212, 503	Upper	398.84	396.81	388	550
Blue	32	2 x 1	184, 653	Lower	315.19	315.04	311	800
Blue	32	2 x 1	199, 649	Lower	315.19	313.34	311	725
Blue	32	1 x 1	99, 660	Lower	315.19	317.74	316	800

Table 19. Summary of MODTRAN Ground Surface Temperatures and SO_2 Concentrations Producing the Best Fit to Corresponding AHI Data

plume. It is an artifact of being able to image a large area of the plume instantaneously. The large variation in ground temperatures could be attributed to large variations in surface composition. Without any additional data over the source or ground truth to compare, it is difficult to come to any additional conclusions.

2. COSPEC / FLYSPEC Results

Without any data collected in similar areas at similar times using similar methods, it is difficult to compare the IR and UV results. The absence of proper wind conditions denied the ability to generate any emission rates that would be worthy of documentation.

While no direct comparisons are drawn between the IR and UV data, the COSPEC and FLYSPEC results from the data collections along Hwy 11 (described in an earlier section of the chapter) are presented in Figures 68 and 69. It is worthy of noting a comparison between these two instruments for a second time. Figure 68 shows two plots of the data collected as COSPEC and FLYSPEC simultaneously traveled Highway 11 in a northeast direction. The plots are of SO_2 path concentration versus time. The figure on the left displays the data collected for the entire traverse. Some anomalies are observed in the

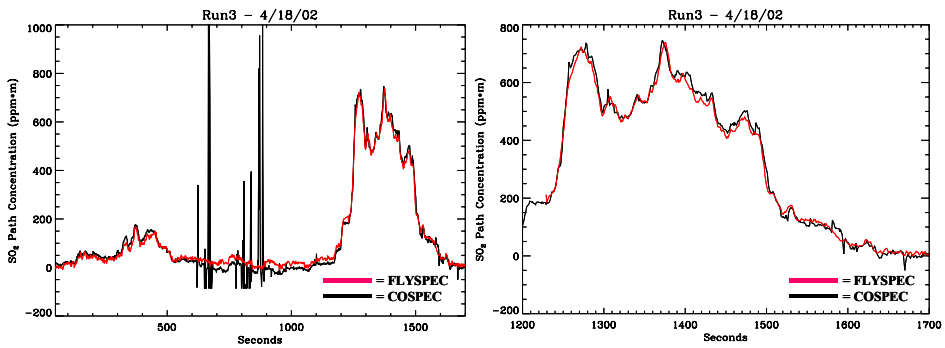

Figure 68. Plots of Data Collected Simultaneously by COSPEC and FLYSPEC Traveling Northeast on Highway 11 from 0958 to 1028 on April 18, 2002

COSPEC data due to saturation of the sensor when passing under trees. The FLYSPEC data is the original data with a 3-point smooth applied. The image on the right is an expanded version of the same data shown on the left between 1200 and 1700 seconds. Figure 69 is a plot of data collected as COSPEC and FLYSPEC retraced their path along Highway 11 traveling in the northwest direction.

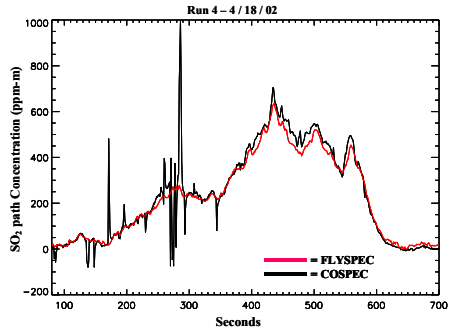

Figure 69. Plot of Data Collected Simultaneously by COSPEC and FLYSPEC Traveling Southwest on Highway 11 from 1030 to 1056 on April 18, 2002

As first demonstrated in Chapter II, FLYSPEC again displays a notable ability to produce results similar to COSPEC. FLYSPEC's results in Figures 68 and 69 were

generated on the move as data was being collected. Instead of watching data unfold on a mechanical plotter as done in collecting data with COSPEC, the collection output is viewed on the screen of a laptop. This comparison reemphasizes that the same product being generated over the years with COSPEC can now be generated equally well with the upgraded technology of FLYSPEC without losing the ability to maintain the consistency of any long running datasets.

D. SUMMARY

The detection and quantification of SO_2 plumes in the LWIR portion of the electromagnetic spectrum looking down from the air or space is not a trivial problem. The analysis is greatly affected by two very important underdetermined problems relating to the received radiation at the sensor. The first underdetermined problem is the separation of ground surface temperature and emissivity that generate the radiation seen at each pixel in the scene. The second underdetermined problem is finding the combination of the unknown ground temperature and SO_2 concentration that produces the radiation seen at each pixel in the scene. To complicate matters, the results of one underdetermined problem are used to solve the other. There are endless possible combinations of ground temperature and SO_2 concentrations that produce similar radiance profiles. As difficult as the problem appears, the methods described in this chapter have been developed to solve it.

THIS PAGE INTENTIONALLY LEFT BLANK

VI. SUMMARY AND CONCLUSIONS

This thesis examines the detection and quantification of volcanic SO_2 plumes via the study of UV and LWIR radiation. Discussion began with the work done in the UV region of the electromagnetic spectrum; as ground based UV sensors have a 30-year history of detection and quantification of SO_2 plumes. Work done with the University of Hawaii's FLYSPEC was conducted in the traditional manner, and high sensitivity to SO_2 was found, with good agreement between FLYSPEC and the COSPEC sensors.

Analysis of SO_2 data collected by the UH sensor, AHI, was presented next. AHI was flown over the area surrounding the Pu'u'O'o Vent of Kilauea Volcano in Hawaii to provide the data for analysis. COSPEC and FLYSPEC also participated in the experiment to provide ground truth.

The analysis is broken into two sections: the detection of SO_2 and the quantification of the SO_2 detected. The detection problem was approached using two main spectral classification and mapping tools: the SAM and the MF. Both tools were applied to data in both radiance and emissive space. Similar results were obtained. The SAM results were used to partition the data in the quantification analysis which followed, thus exploiting the redundant character of hyperspectral imagery.

The emissivity normalization method was applied to separate temperature and emissivity. The emissivity and temperature results generated using this method are then used to help solve the second underdetermined radiance equation in which the two unknown variables are ground temperature and SO_2 concentration.

MODTRAN was used to help solve this second underdetermined radiance equation by modeling the atmosphere between the ground and the sensor. Specific variables describing the SO_2 plume such as plume altitude, plume thickness, and meteorological conditions on the day of collection were used to develop a number of atmospheric layers describing the path traveled by radiation in the model. Specific inputs for the sensor such as operating altitude and operating wavelengths were also required. The two unspecified variables in the model were ground temperature and SO_2

concentration. The model was used to generate a spectral library of radiance profiles containing numerous variations on combinations of different ground temperatures and SO_2 concentrations. These MODTRAN profiles were then plotted against the AHI radiance profiles to determine a best fit.

AHI reported significantly higher SO_2 concentration path lengths than the UV sensors, about 100 times higher. Unfortunately, the results of AHI's IR data and FLYSPEC's UV data are not directly compared due to several location, weather, and timing factors. There is a significant difference in the physical locations of the IR and UV data collections that produced SO_2 signatures. AHI detected SO_2 directly over the vent while FLYSPEC detected SO_2 several kilometers away from the vent along the highway. The lack of wind causes the drift of the plume from the vent to be very unpredictable. It is not unreasonable to expect a decline in the density of several orders of magnitude over the distances spanned by the data set.

Appendix A displays several data collections by AHI over the same road that FLYSPEC and COSPEC detected the SO_2 plume. There is no apparent SO_2 in the AHI data. There could be several explanations for this. The time of the AHI data collection over the road was slightly different than FLYSPEC and COSPEC. The unpredictable plume drift due to lack of wind makes it difficult to come to a definite conclusion as to whether the plume was present on the road at the time of the AHI data collection. Another explanation may be found in the sensitivity of the sensor. As seen in Figure 59 of Chapter V, there appears to be a lower limit of detection for a down-looking IR sensor of 100 to 200 ppm. These values are multiplied by the model's plume thickness to generate concentration path lengths of 15,000 to 30,000 ppm-m. These values are much greater than any seen by FLYSEPEC or COSPEC along the road.

Overall, AHI successfully demonstrated the ability to detect and quantify a volcanic SO_2 plume. It is believed that if the experiment would be rerun on a day with more ideal weather conditions that may produce data sets that are better geographically correlated, a strong comparison of the results could be produced using the methods described above. With additional data collections and comparisons with COSPEC and FLYSPEC results, AHI could prove to be a valuable addition to the sensors that are

currently used to monitor SO_2 plumes. The airborne aspect allows collection of data during times that may not be safe for COSPEC or FLYSPEC to collect. It also allows a visualization of a large area of the plume nearly instantaneously. With multiple passes over a plume, this is could prove beneficial in monitoring the behavior of the plume under different weather conditions. The infrared nature of AHI provides the additional benefit of monitoring the thermal aspects of the volcano such as active lava flows and determining various emissivities of the basaltic rock. Finally, the hyperspectral nature of AHI must not be overlooked. A detailed classification of materials, whether it is vegetation, rocks, or an SO_2 plume cannot be accomplished without this.

THIS PAGE INTENTIONALLY LEFT BLANK

APPENDIX A. FALSE COLOR SIMULATED TIMS IMAGES WITH DECORRELATION STRETCH APPLIED

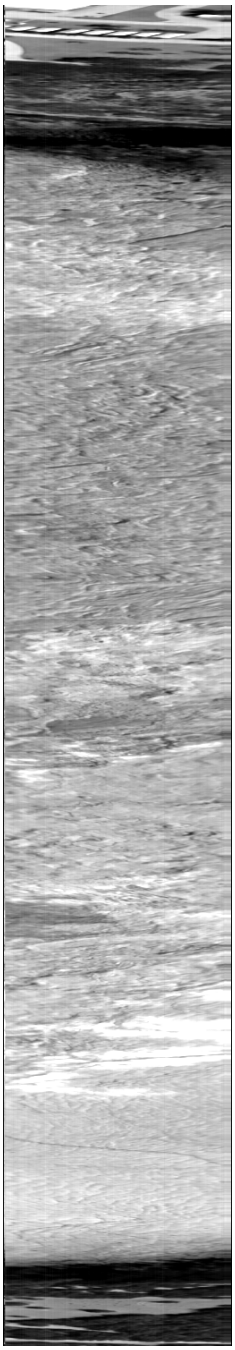

Radiance Image

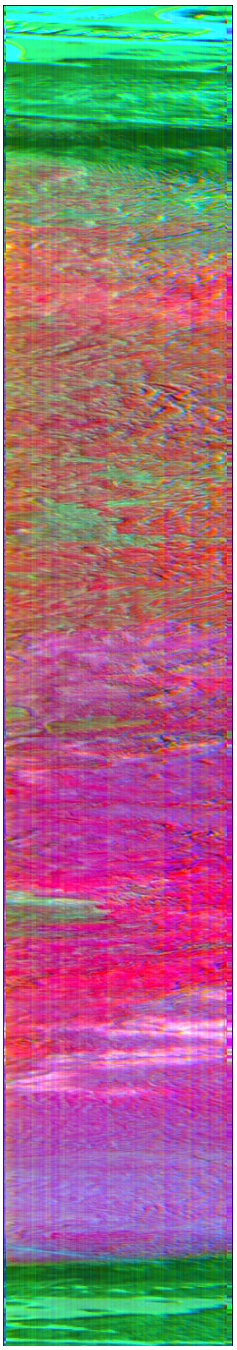

False Color Decorrelation Stretch Image

Figure 70. Decorrelation Stretch Applied to Simulated TIMS Image of R1_A_093134

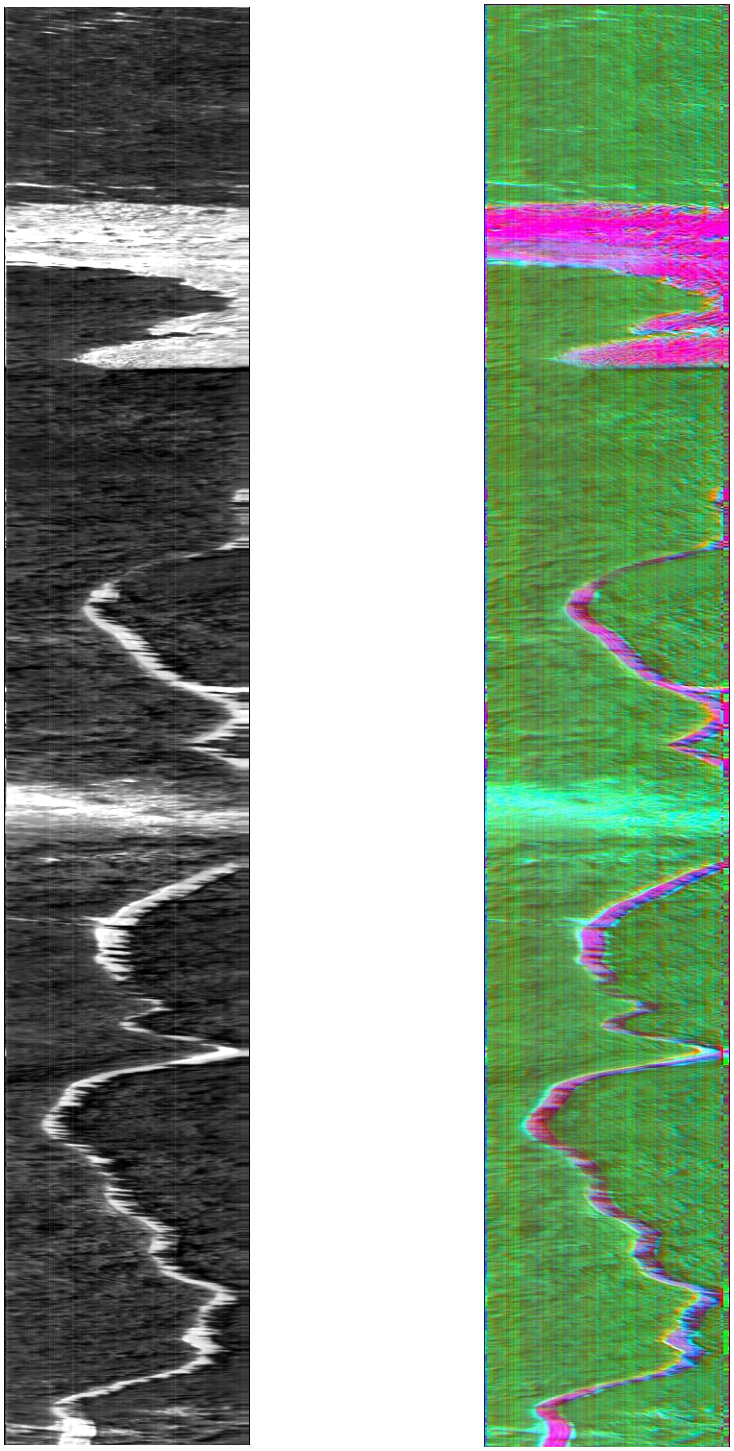

Radiance Image False Color Decorrelation Stretch Image

Figure 71. Decorrelation Stretch Applied to Simulated TIMS Image of R1_A_093226

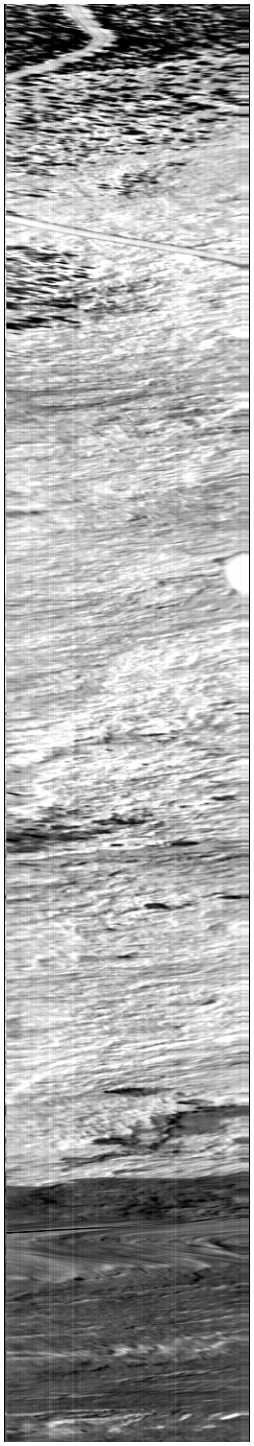

Radiance Image

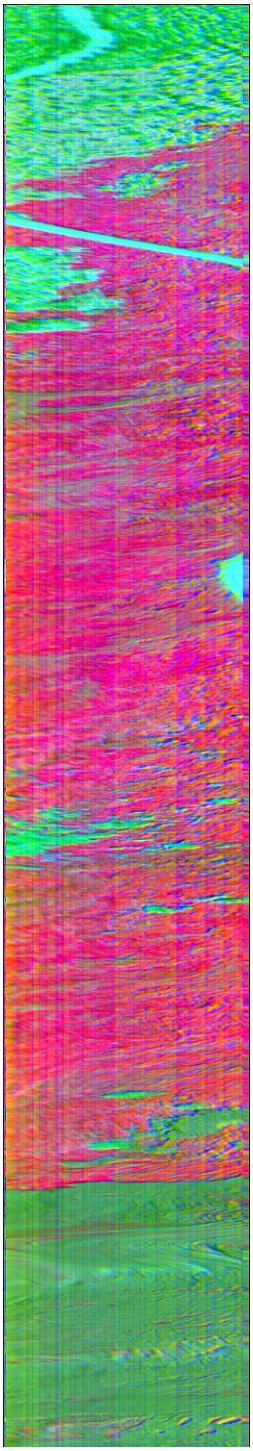

False Color Decorrelation Stretch Image

Figure 72. Decorrelation Stretch Applied to Simulated TIMS Image of R1_A_093433

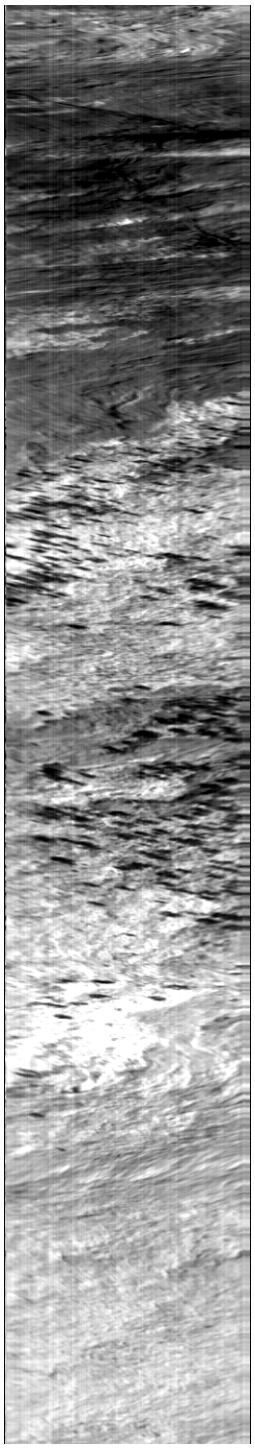

Radiance Image

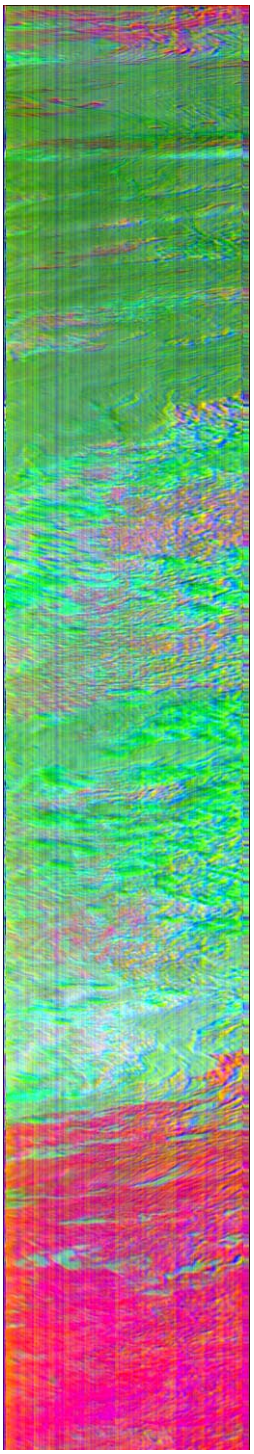

False Color Decorrelation Stretch Image

Figure 73. Decorrelation Stretch Applied to Simulated TIMS Image of R1_A_093525

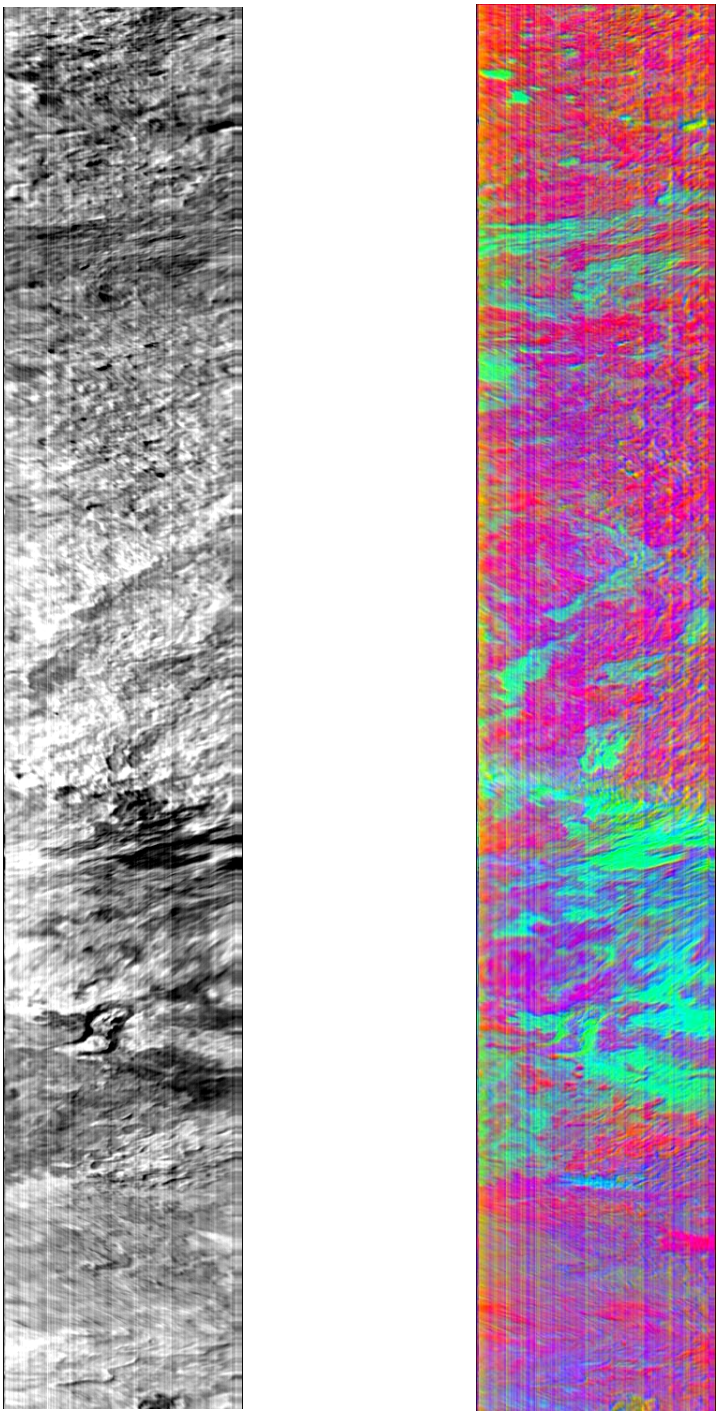

Radiance Image False Color Decorrelation Stretch Image

Figure 74. Decorrelation Stretch Applied to Simulated TIMS Image of R1_A_093618

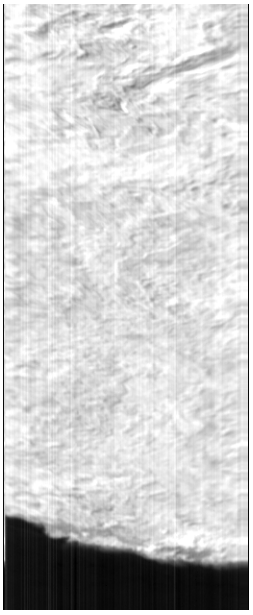

Radiance Image
(Image only 800 lines)

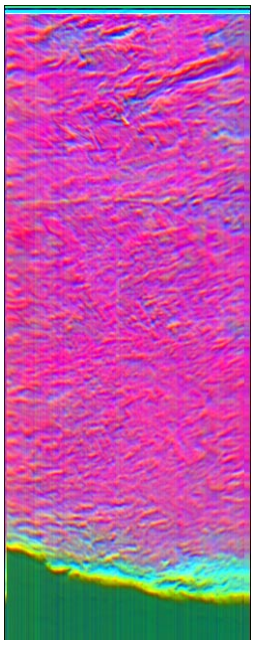

False Color Decorrelation Stretch Image
(Image only 800 lines)

Figure 75. Decorrelation Stretch Applied to Simulated TIMS Image of R1_A_093718

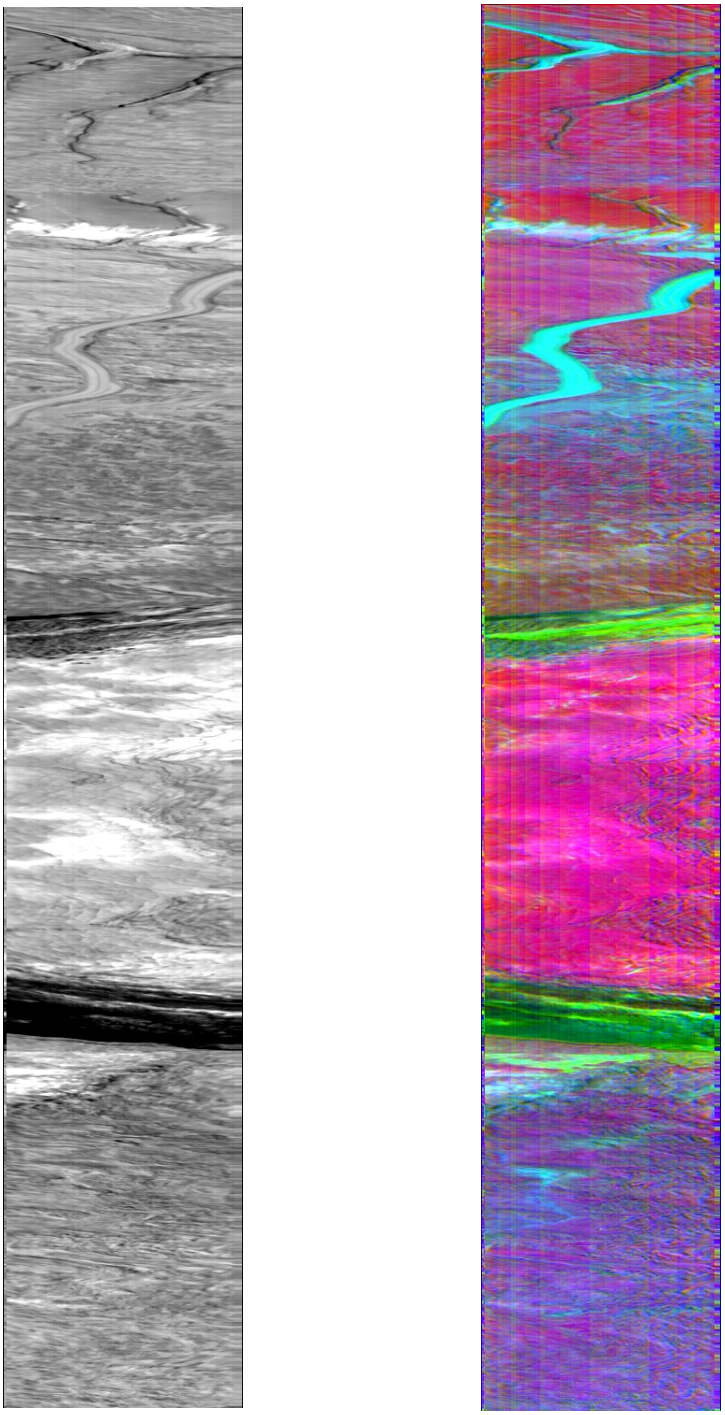

Radiance Image False Color Decorrelation Stretch Image

Figure 76. Decorrelation Stretch Applied to Simulated TIMS Image of R1_B_094450

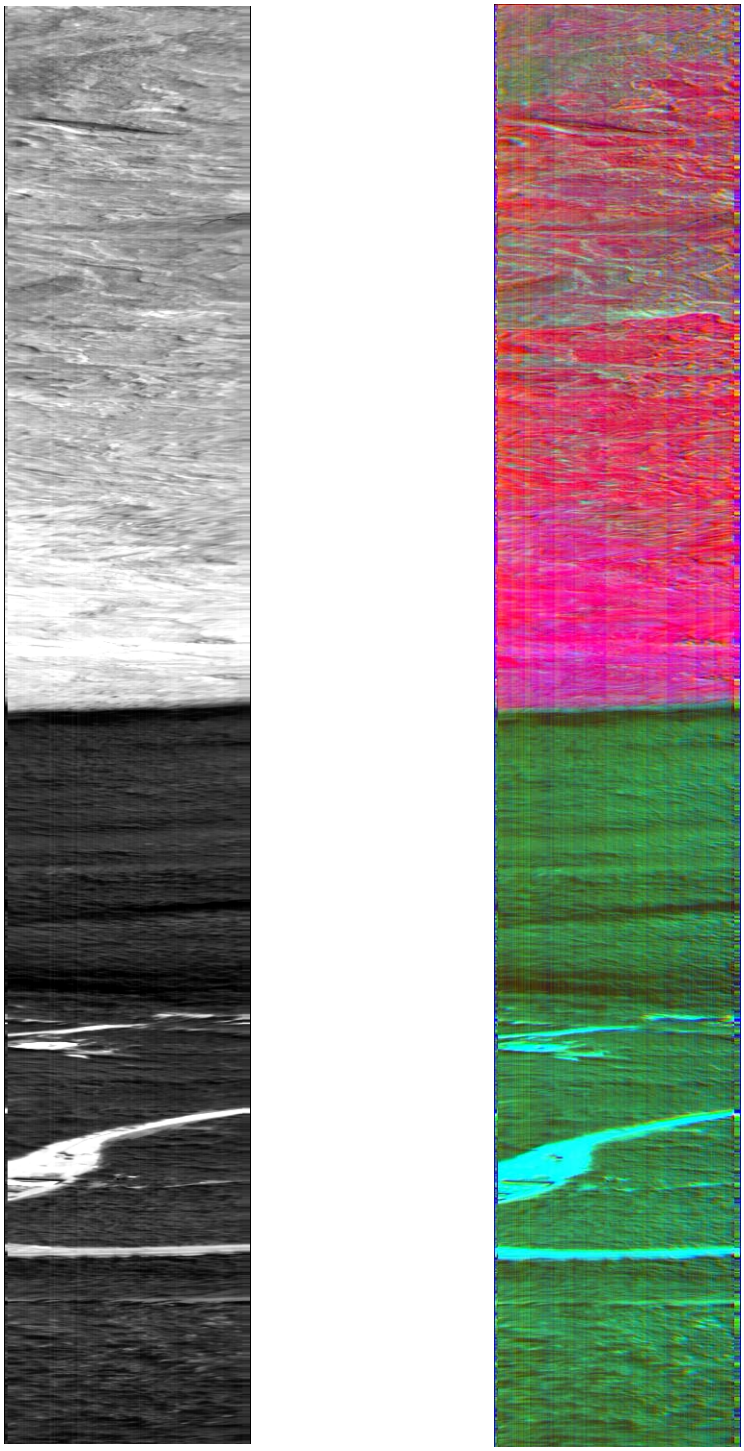

Radiance Image False Color Decorrelation Stretch Image

Figure 77. Decorrelation Stretch Applied to Simulated TIMS Image of R1_B_094542

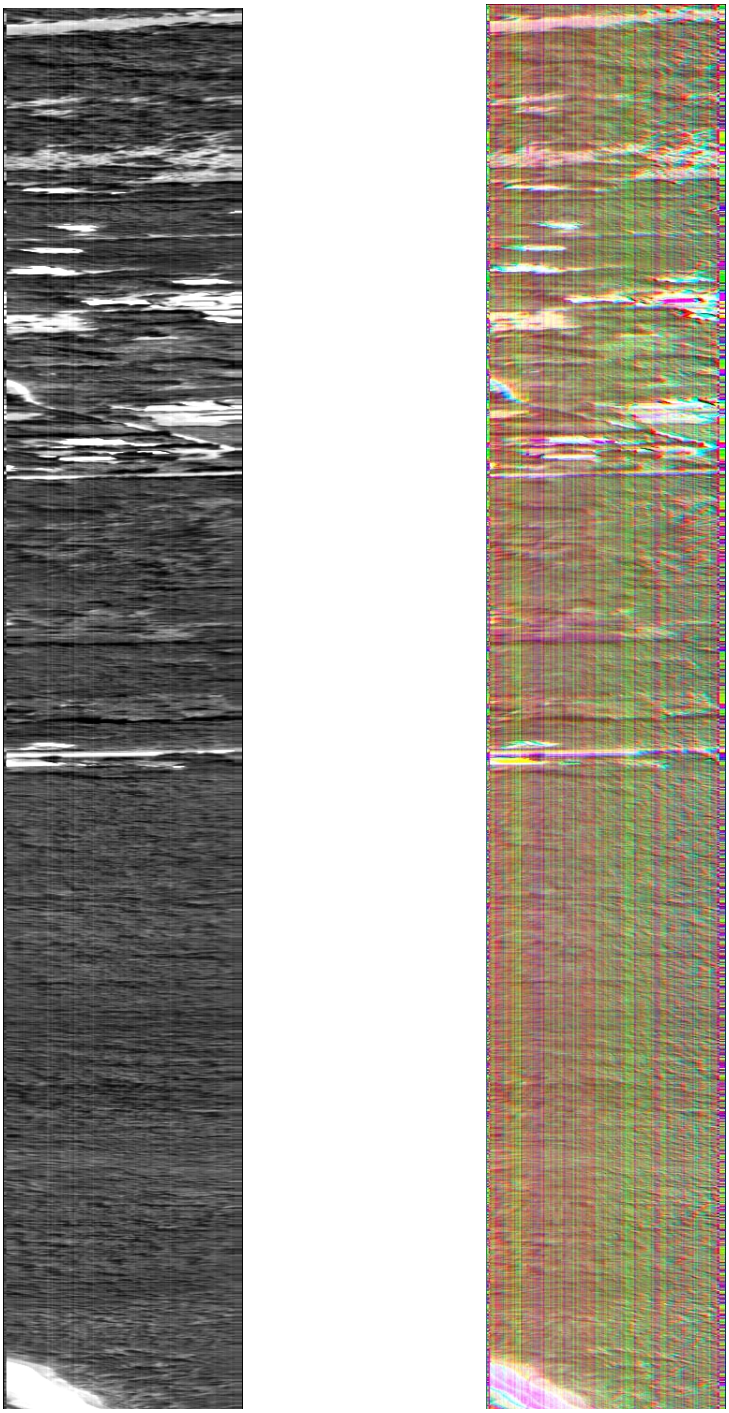

Radiance Image False Color Decorrelation Stretch Image

Figure 78. Decorrelation Stretch Applied to Simulated TIMS Image of R1_B_094635

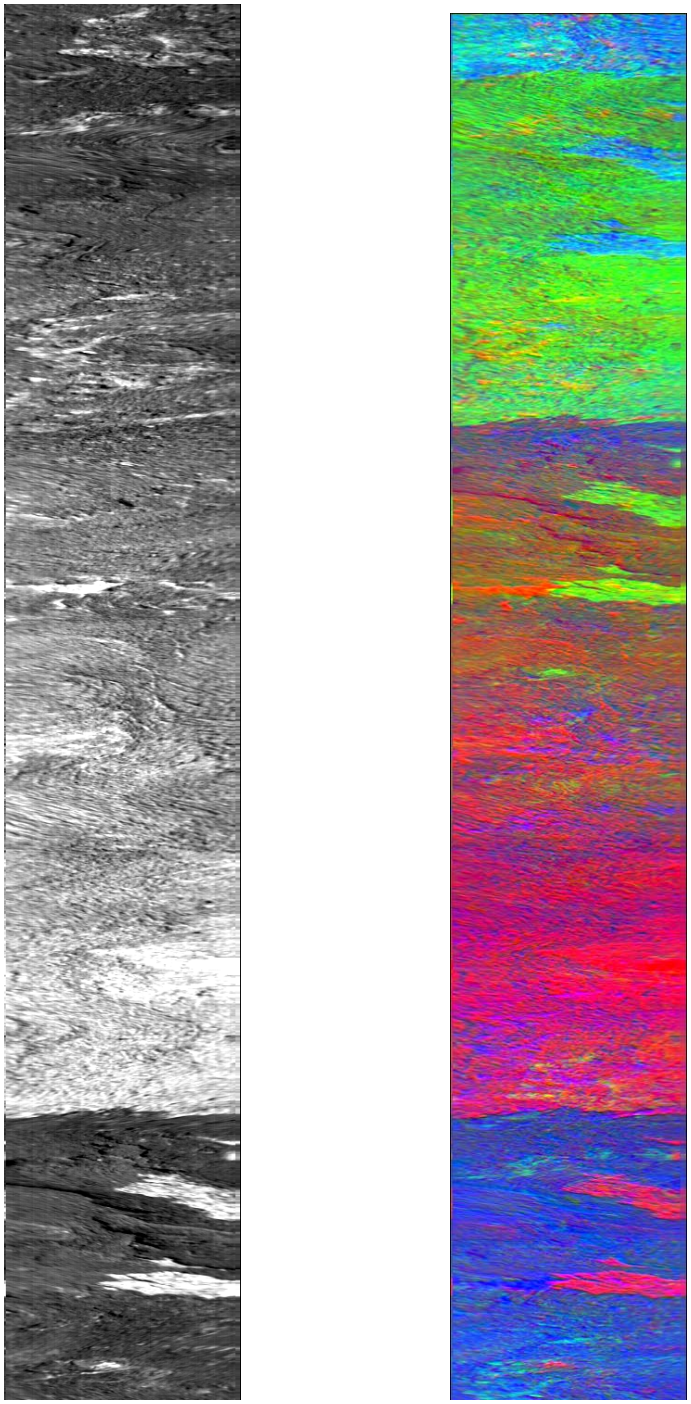

Radiance Image False Color Decorrelation Stretch Image

Figure 79. Decorrelation Stretch Applied to Simulated TIMS Image of R1_C_095258

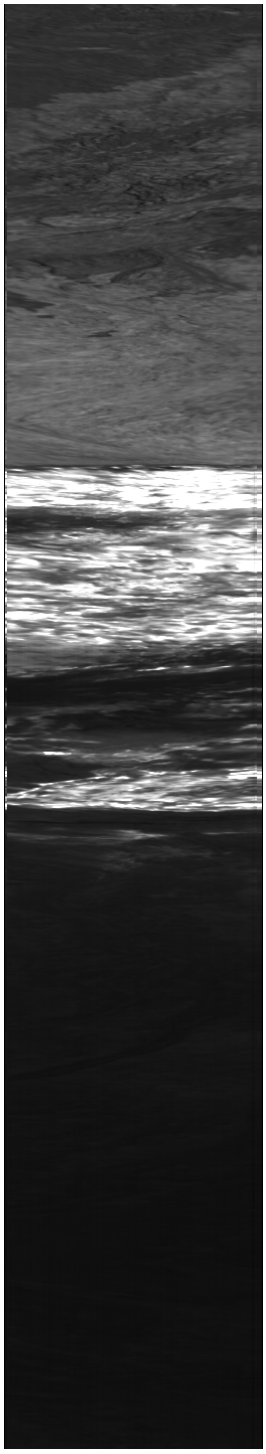

Radiance Image

False Color Decorrelation Stretch Image

Figure 80. Decorrelation Stretch Applied to Simulated TIMS Image of R1_C_095349

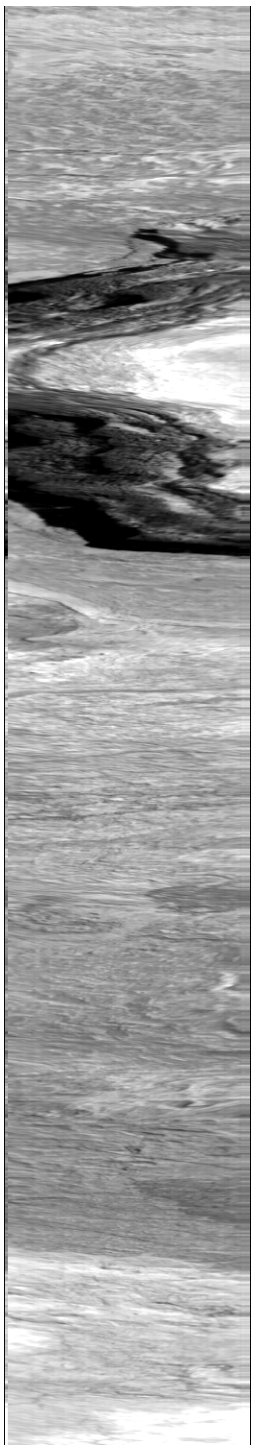

Radiance Image

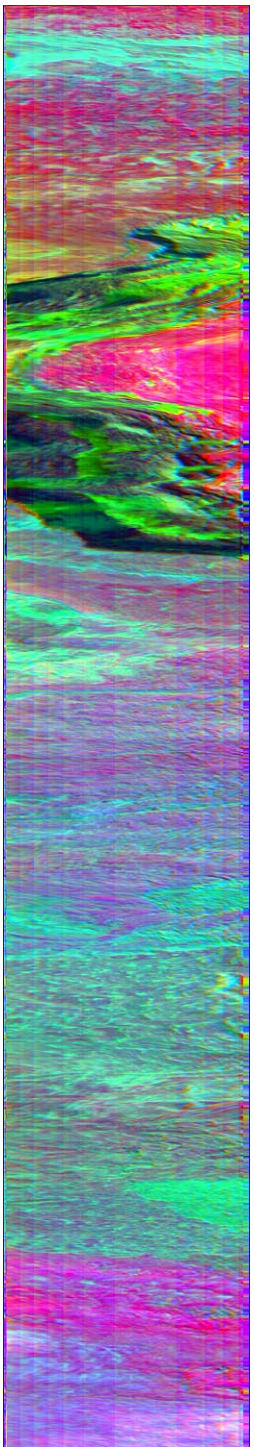

False Color Decorrelation Stretch Image

Figure 81. Decorrelation Stretch Applied to Simulated TIMS Image of R2_B_100030

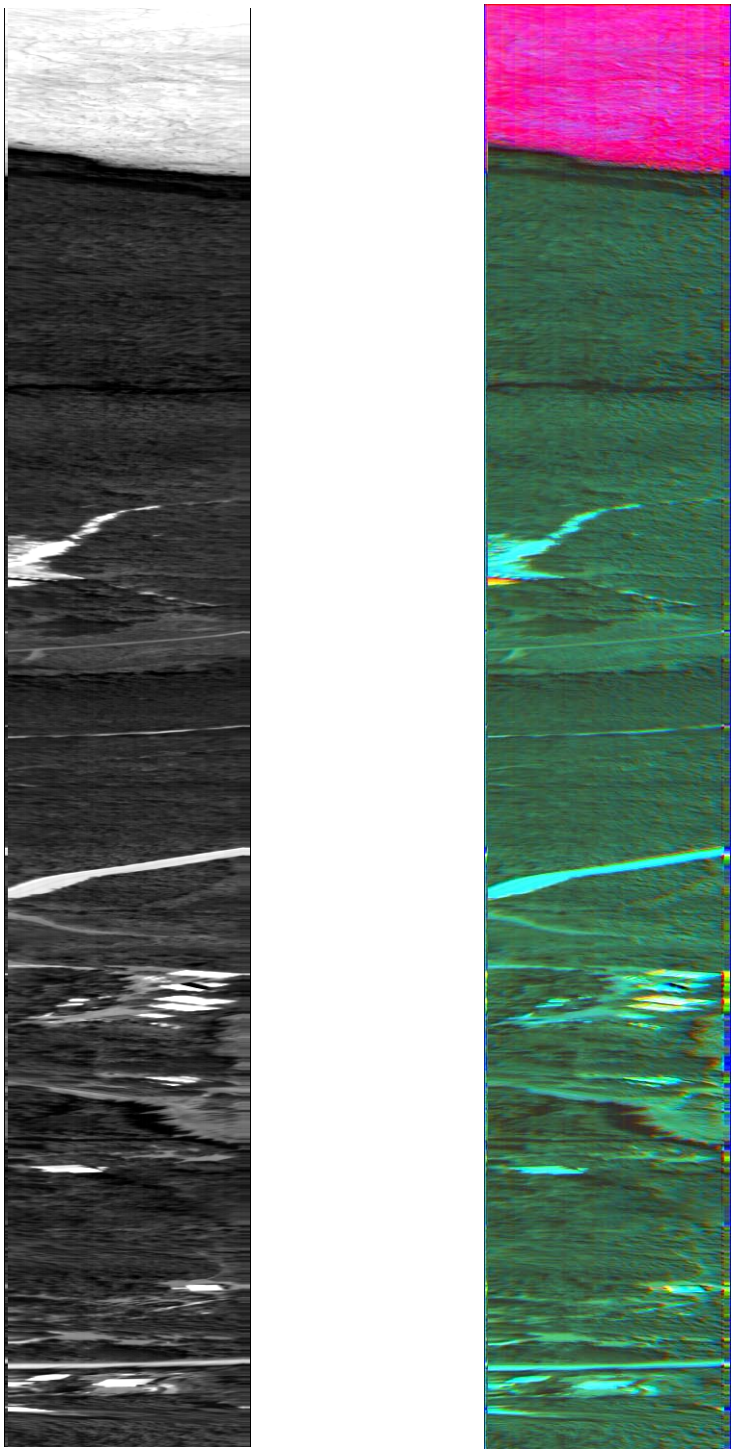

Radiance Image False Color Decorrelation Stretch Image

Figure 82. Decorrelation Stretch Applied to Simulated TIMS Image of R2_B_100121

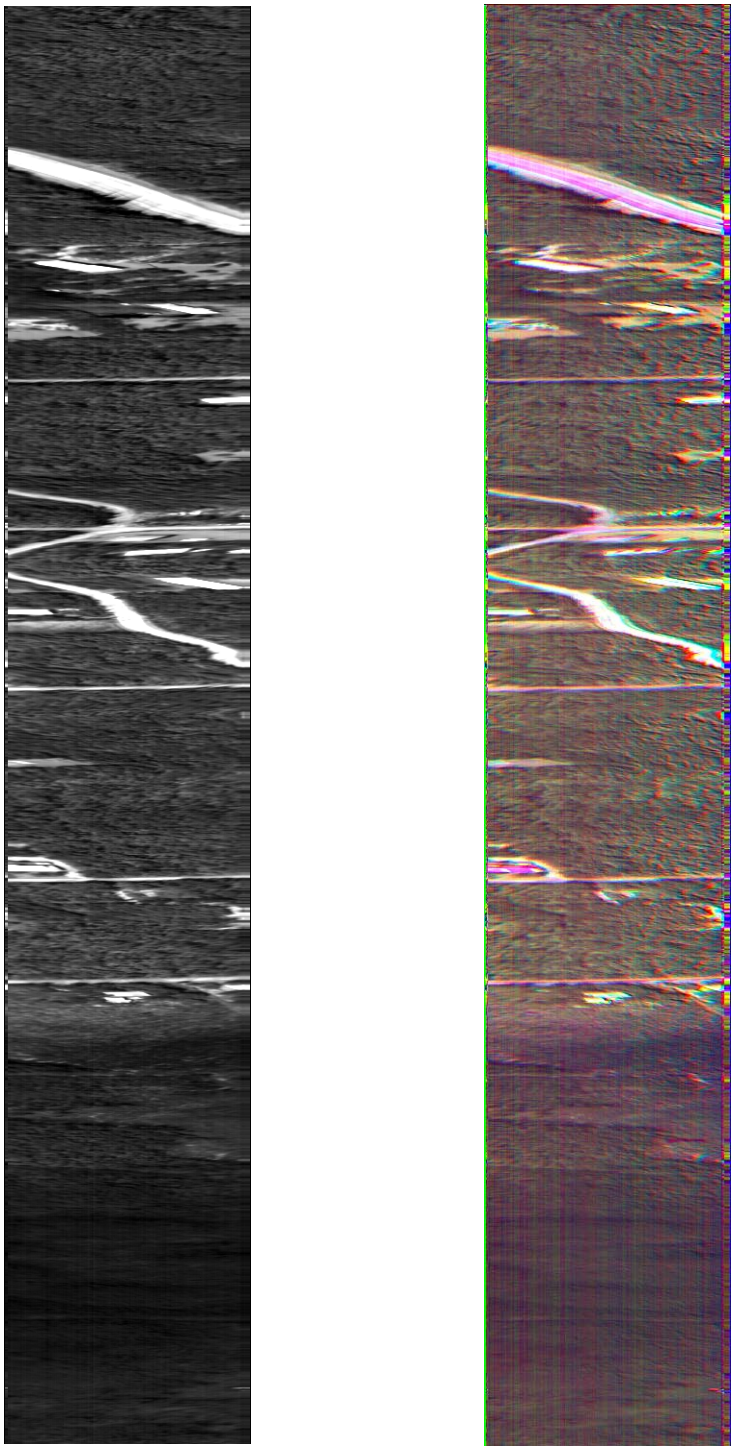

Radiance Image False Color Decorrelation Stretch Image

Figure 83. Decorrelation Stretch Applied to Simulated TIMS Image of R2_B_100213

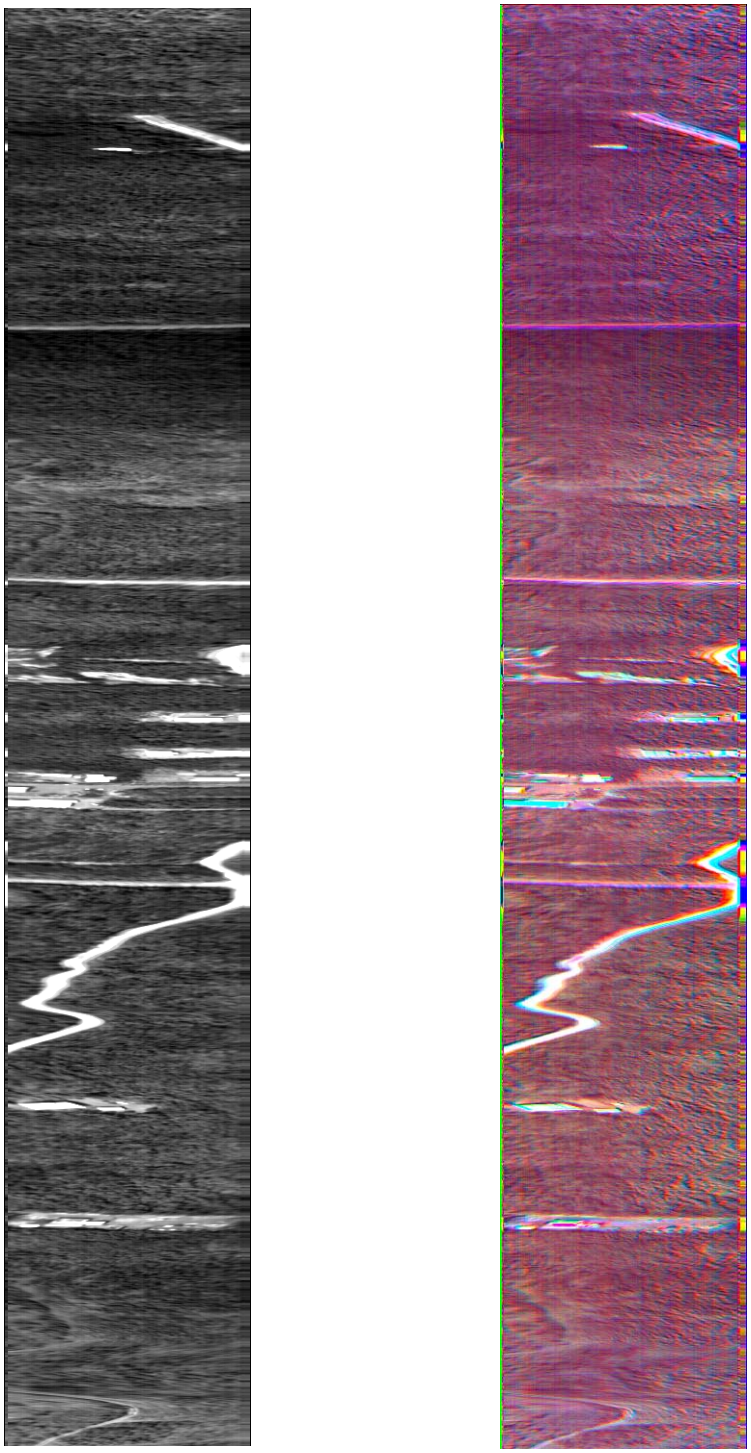

Radiance Image False Color Decorrelation Stretch Image

Figure 84. Decorrelation Stretch Applied to Simulated TIMS Image of R2_B_100312

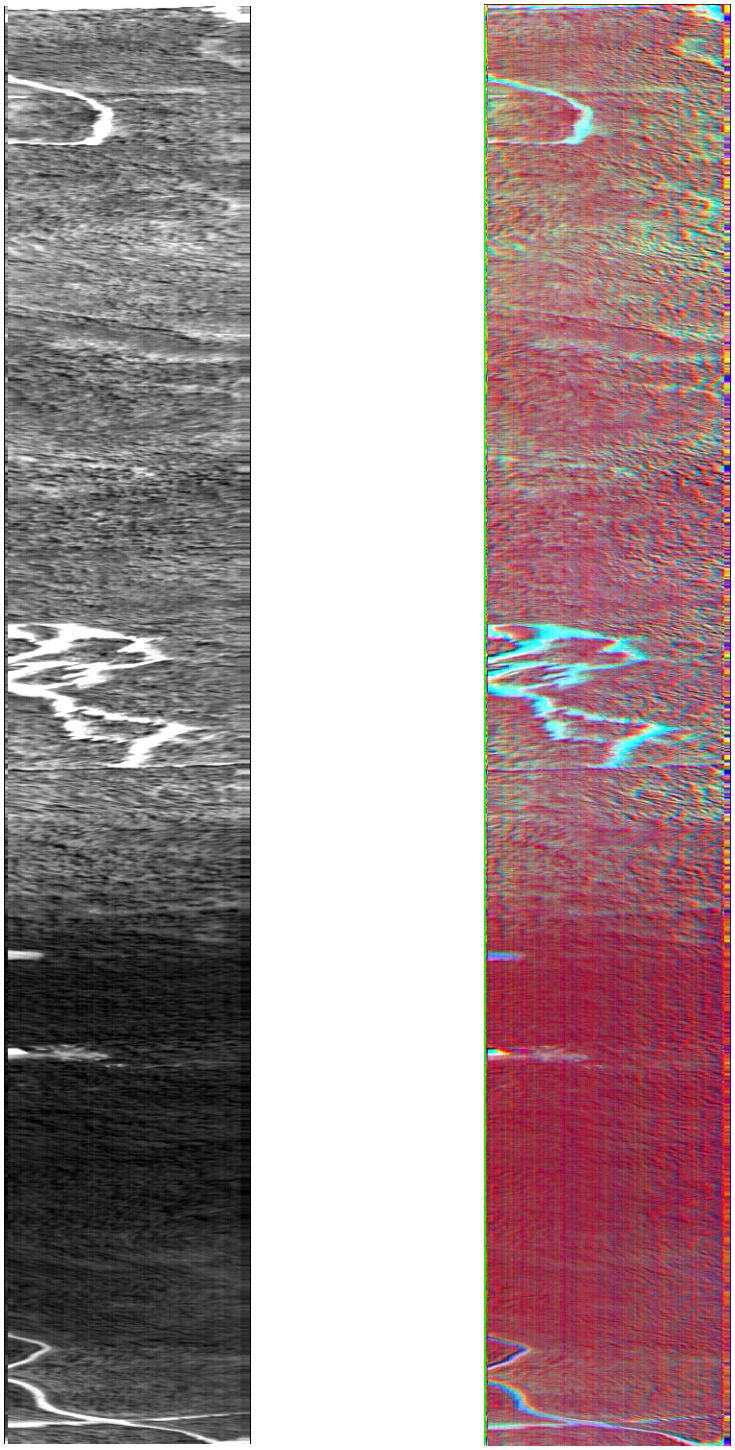

Radiance Image False Color Decorrelation Stretch Image

Figure 85. Decorrelation Stretch Applied to Simulated TIMS Image of R2_B_100403

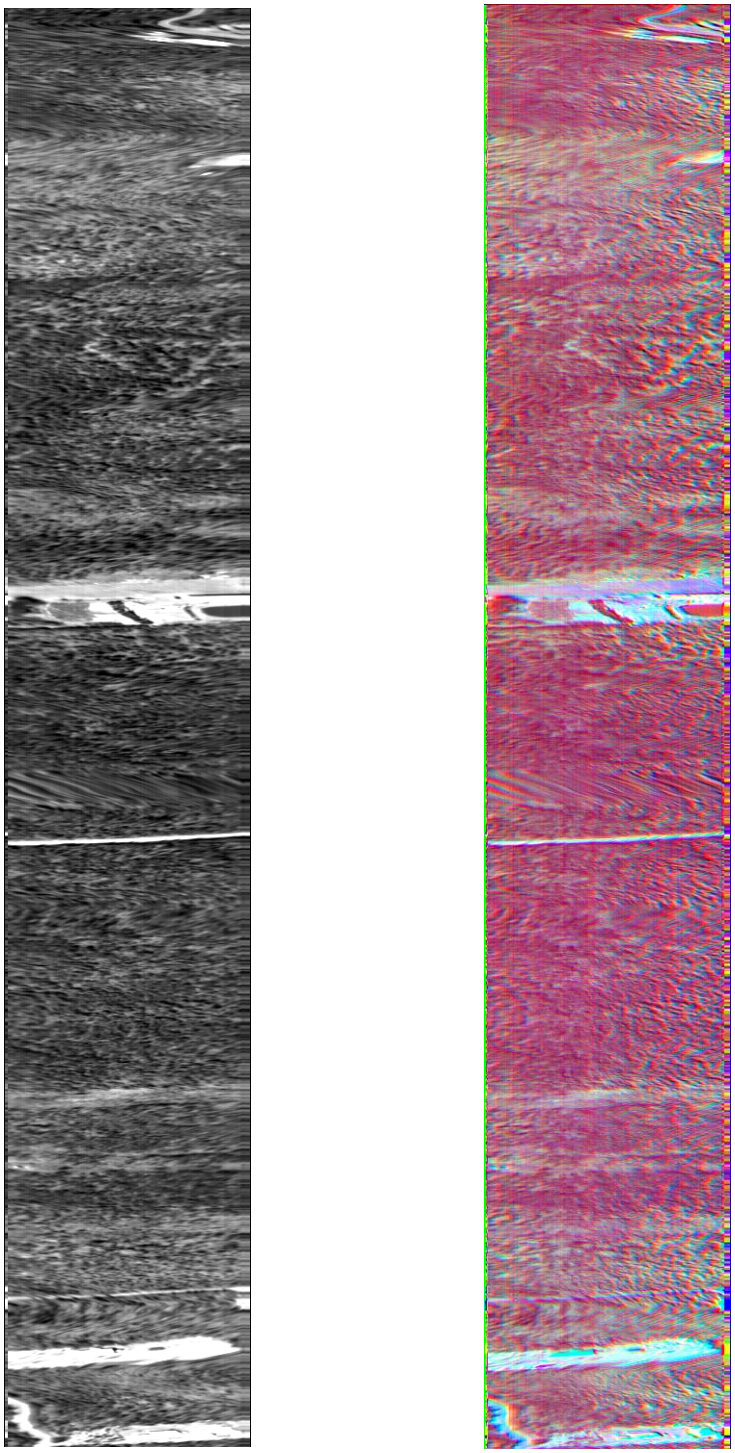

Radiance Image False Color Decorrelation Stretch Image

Figure 86. Decorrelation Stretch Applied to Simulated TIMS Image of R2_B_100455

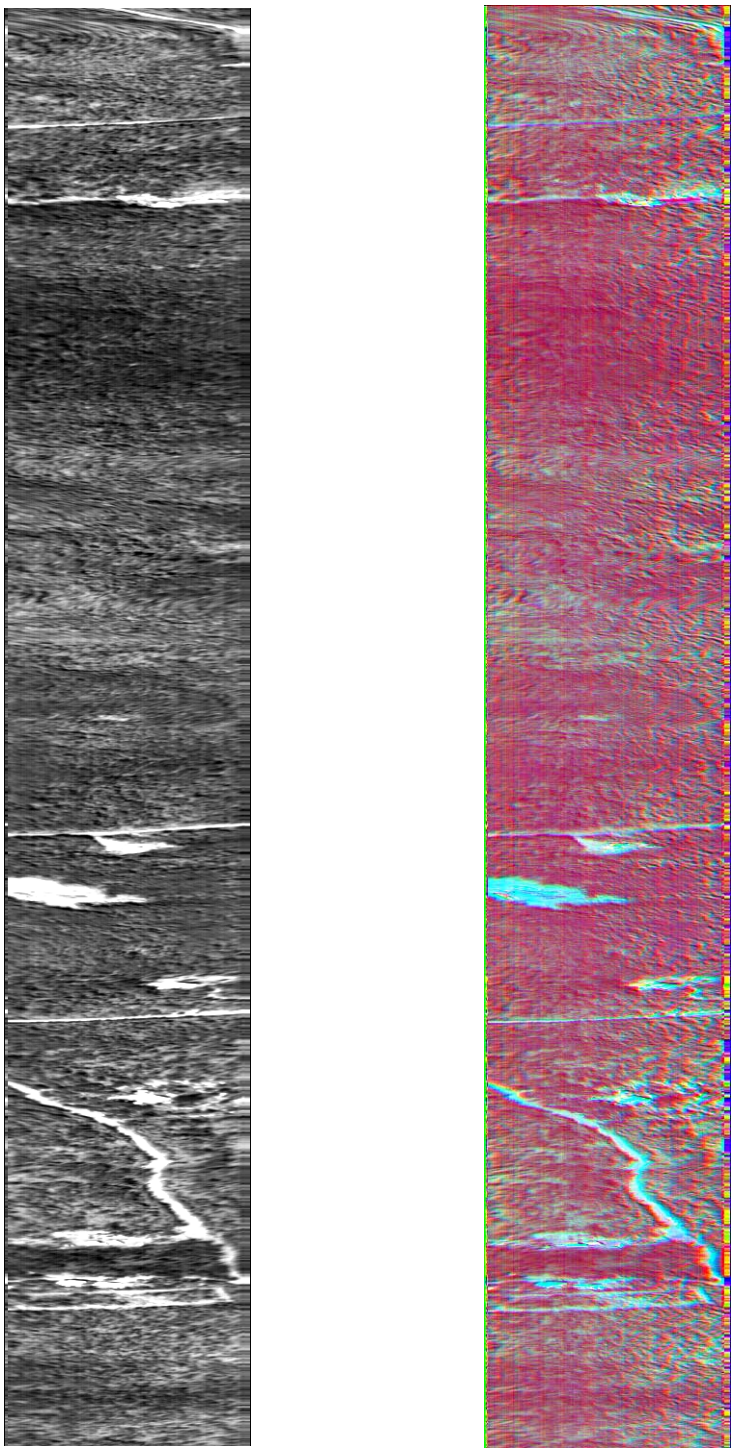

Radiance Image False Color Decorrelation Stretch Image

Figure 87. Decorrelation Stretch Applied to Simulated TIMS Image of R2_B_100549

APPENDIX B. MODTRAN CODE

```
M   7    2    1    0    0    0    0    0    0    0    0    1   -1 360.000    .00
f   0f   0   330.000   1.00000   1.00000 f t f
DATA/BMP99_01.BIN
    1    0    0    0    0    0      .000      .000      .000      .000      .000
    4    1    0TEST
  .000E+00 1.014E+03 2.670E+01 6.700E+01  .000E+00  .000E+00ABH6666666A6666
0.000E+00 0.000E+00 0.000E+00 0.000E+00 0.000E+00 1.600E+03 0.000E+00 0.000E+00
0.000E+00
  .150E+00 6.000E+00 6.000E+00 6.000E+00 6.000e+00 6.000E+00666666666666666
0.000E+00 0.000E+00 0.000E+00 0.000E+00 0.000E+00 0.000E+00 0.000E+00 0.000E+00
0.000E+00
 0.350E+00 6.000E+00 6.000E+00 6.000E+00 6.000E+00 6.000E+00666666666666666
0.000E+00 0.000E+00 0.000E+00 0.000E+00 0.000E+00 0.000E+00 0.000E+00 0.000E+00
0.000E+00
 0.610E+00 6.000E+00 6.000E+00 6.000E+00 6.000E+00 6.000E+00666666666666666
0.000E+00 0.000E+00 0.000E+00 0.000E+00 0.000E+00 0.000E+00 0.000E+00 0.000E+00
0.000E+00
     0.800      .000   180.000      .000      .000      .000    0        0.00000
       740      1250         1         2rm        w1aa
    0
```

Figure 88. MODTRAN Code Used for AHI Data Analysis

THIS PAGE INTENTIONALLY LEFT BLANK

APPENDIX C. MODTRAN AND AHI RADIANCE PROFILE COMPARISONS

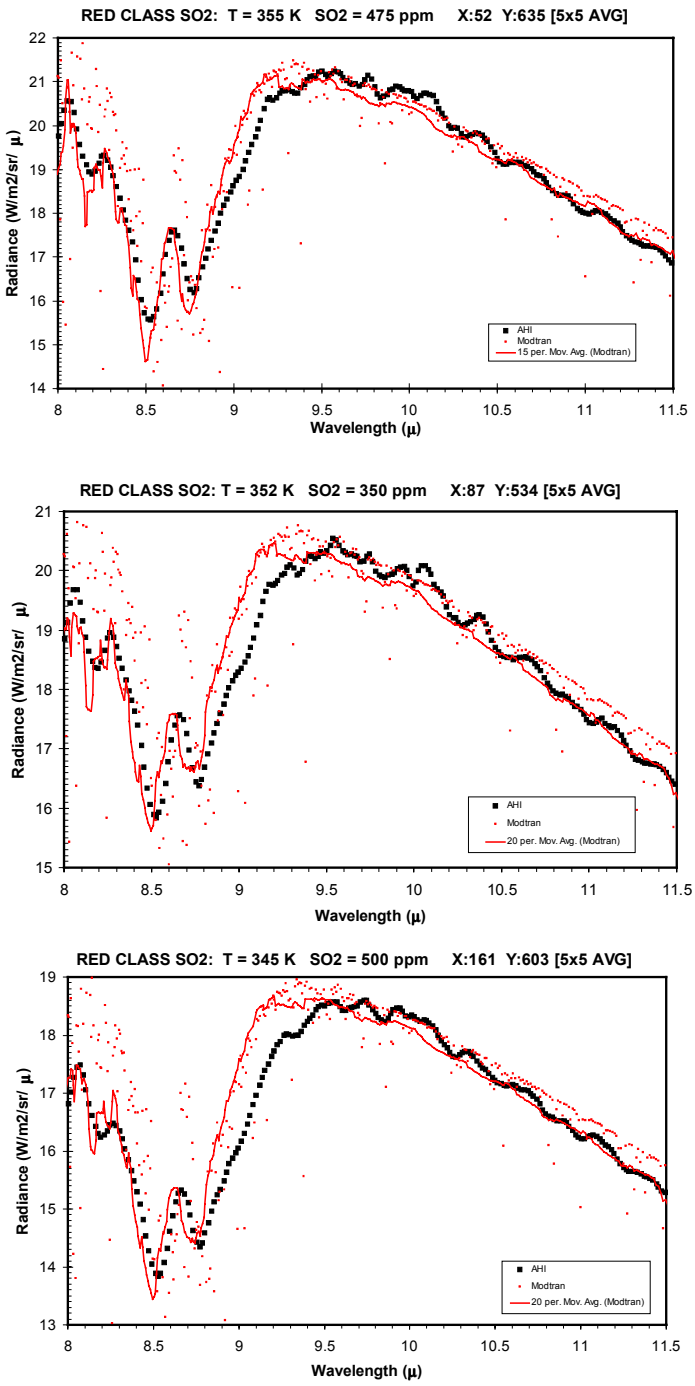

Figure 89. MODTRAN and AHI Radiance Profile Comparison for Pixels of the Red SO_2 Class

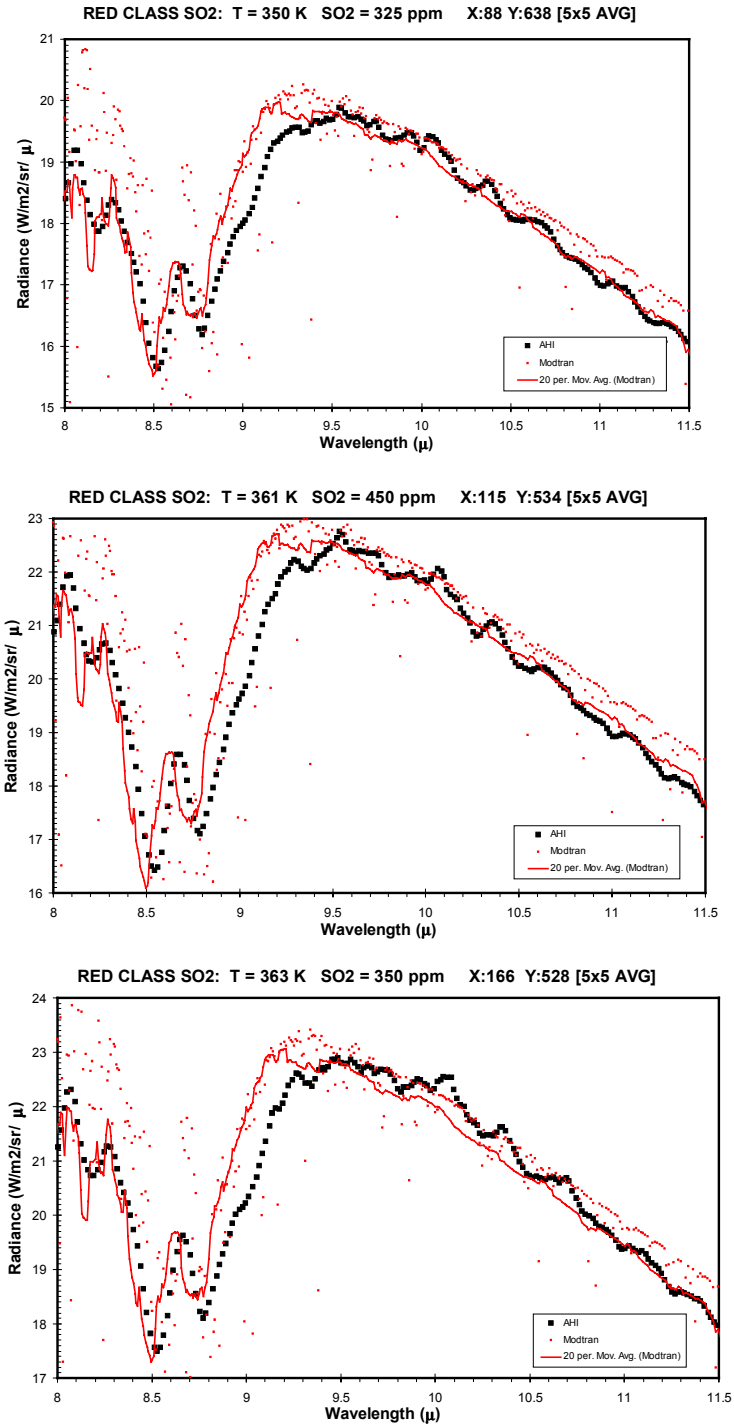

Figure 90. MODTRAN and AHI Radiance Profile Comparison for Pixels of the Red SO_2 Class Continued

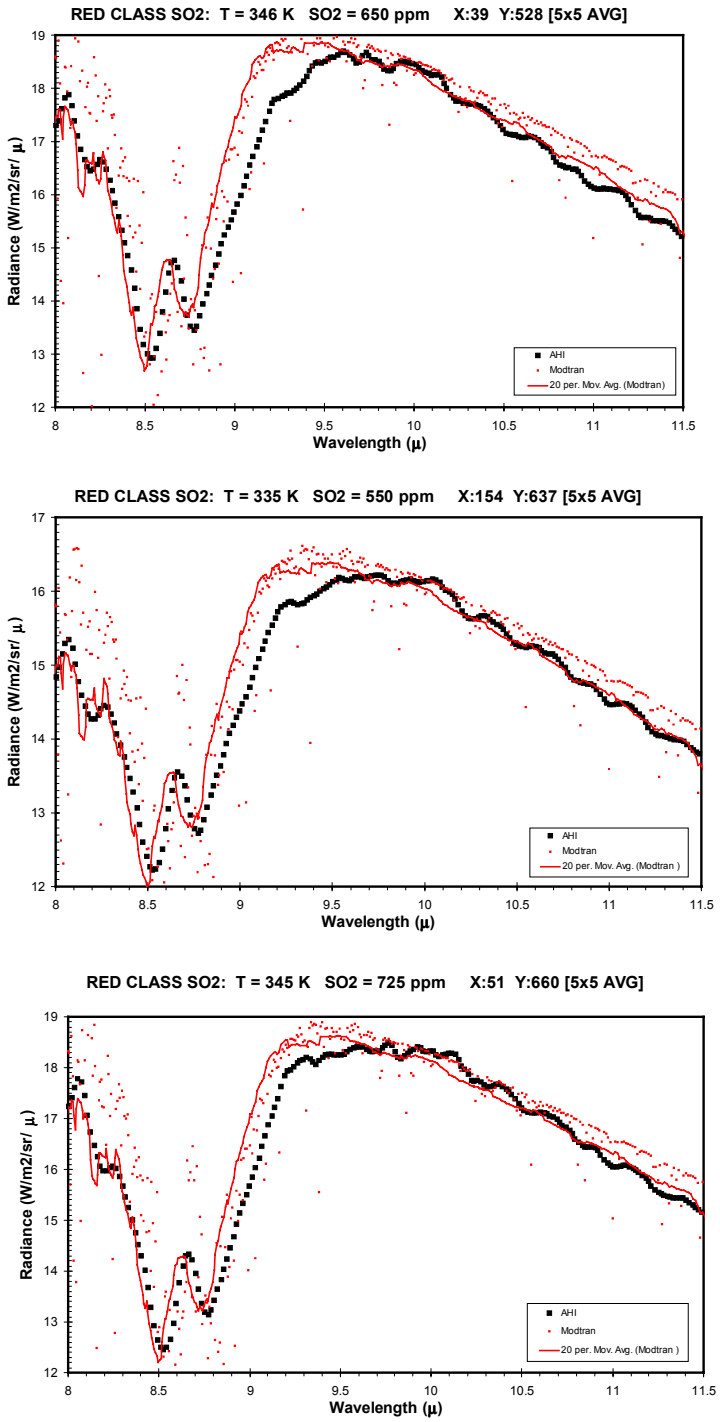

Figure 91. MODTRAN and AHI Radiance Profile Comparison for Pixels of the Red SO_2 Class End

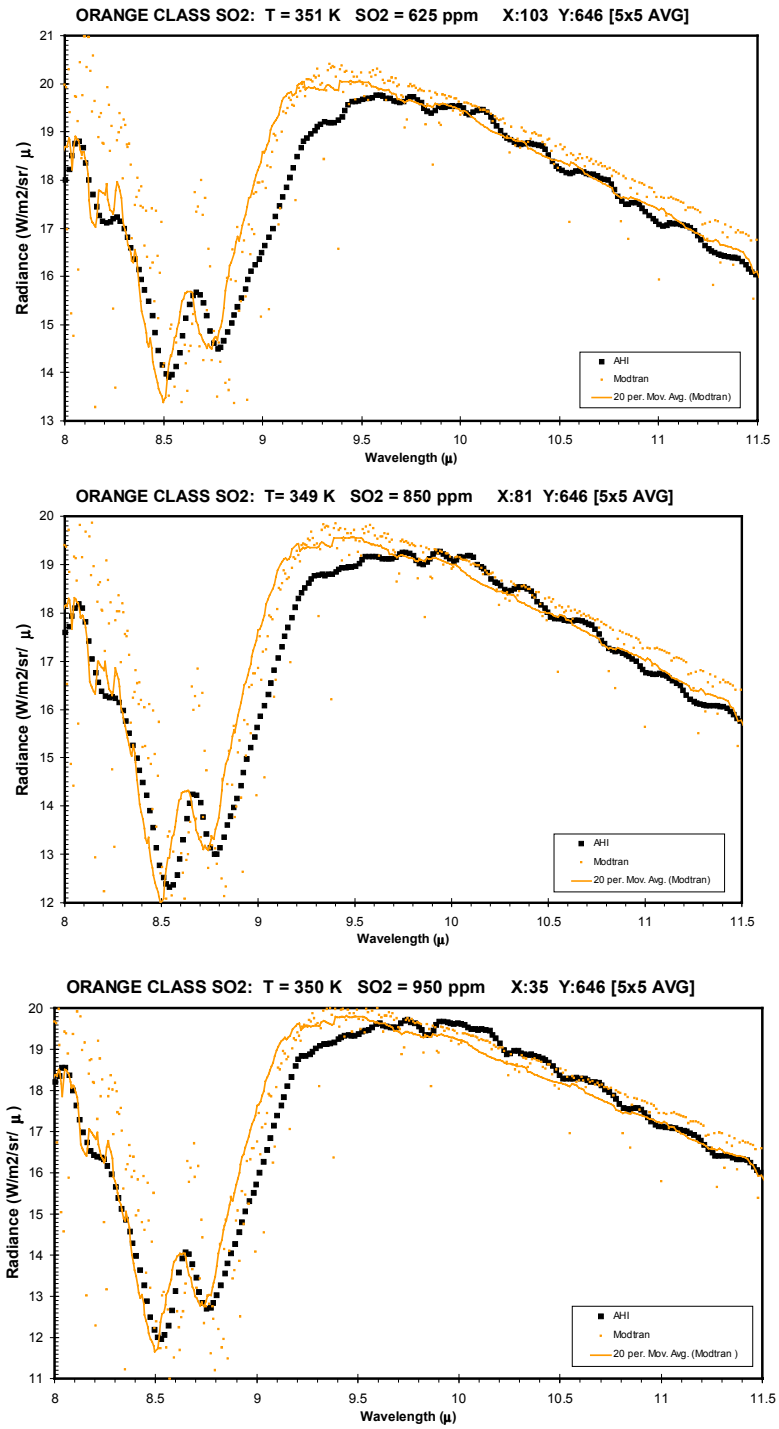

Figure 92. MODTRAN and AHI Radiance Profile Comparison for Pixels of the Orange SO_2 Class

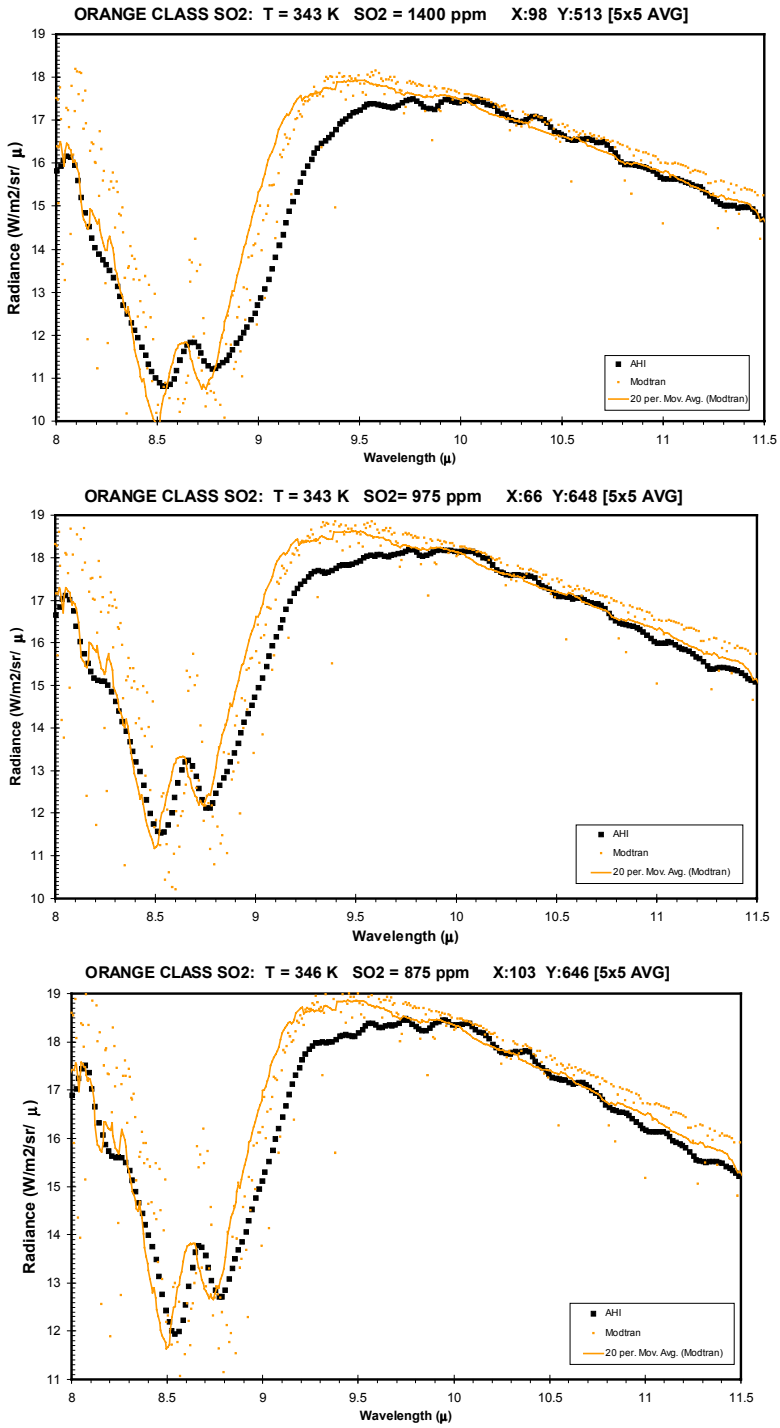

Figure 93. MODTRAN and AHI Radiance Profile Comparison for Pixels of the Orange SO_2 Class Continued

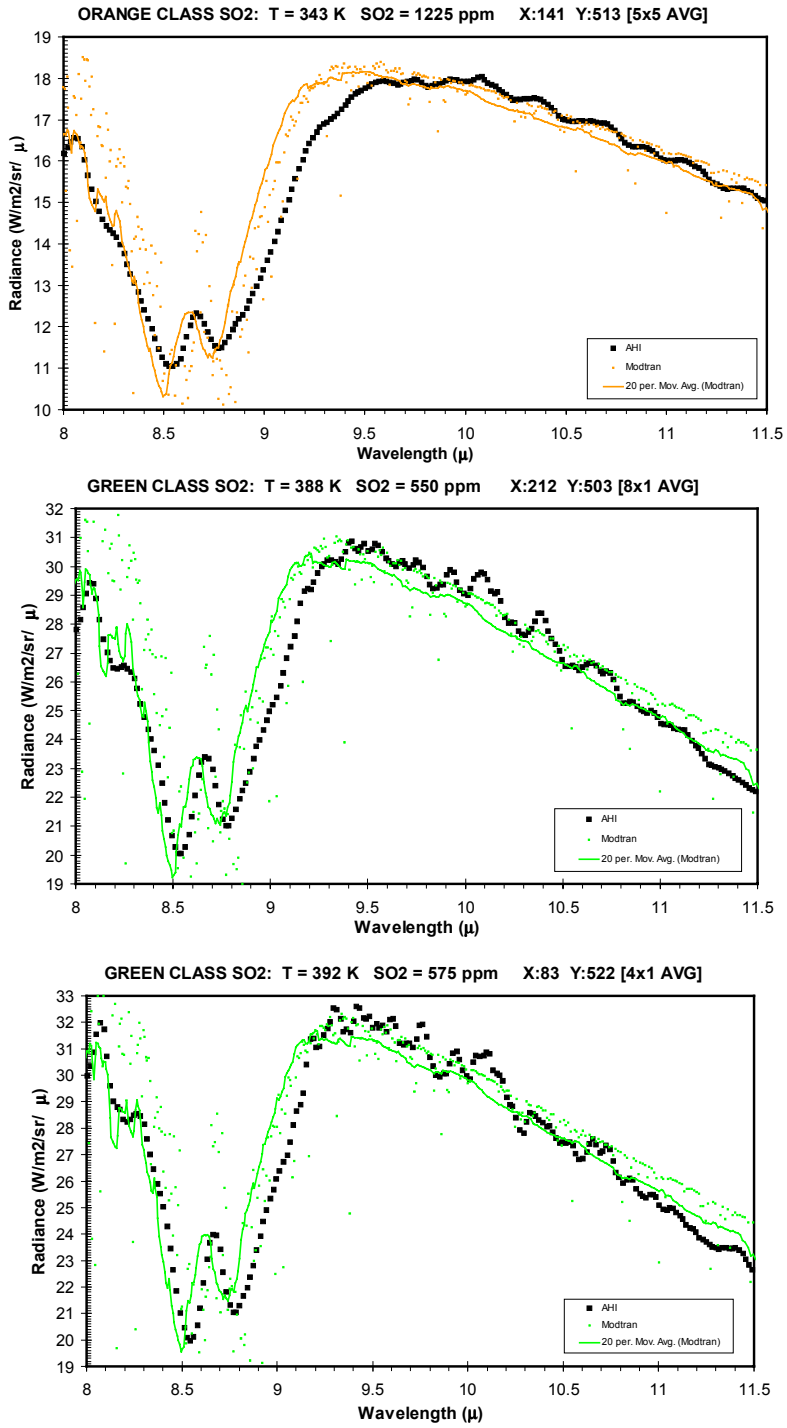

Figure 94. MODTRAN and AHI Radiance Profile Comparison for Pixels of the Orange SO_2 Class End and for Pixels of the Green SO_2 Class

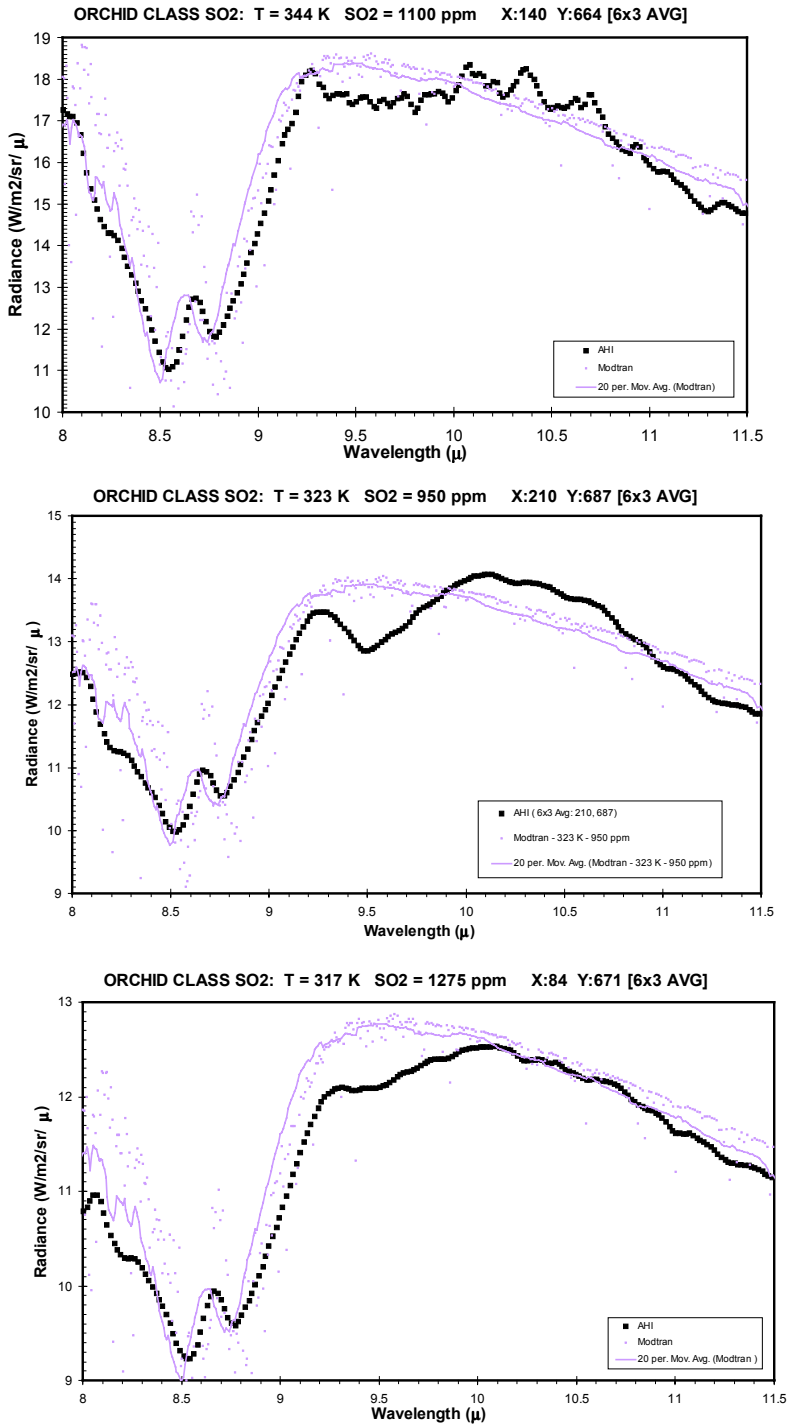

Figure 95. MODTRAN and AHI Radiance Profile Comparison for Pixels of the Orchid SO_2 Class

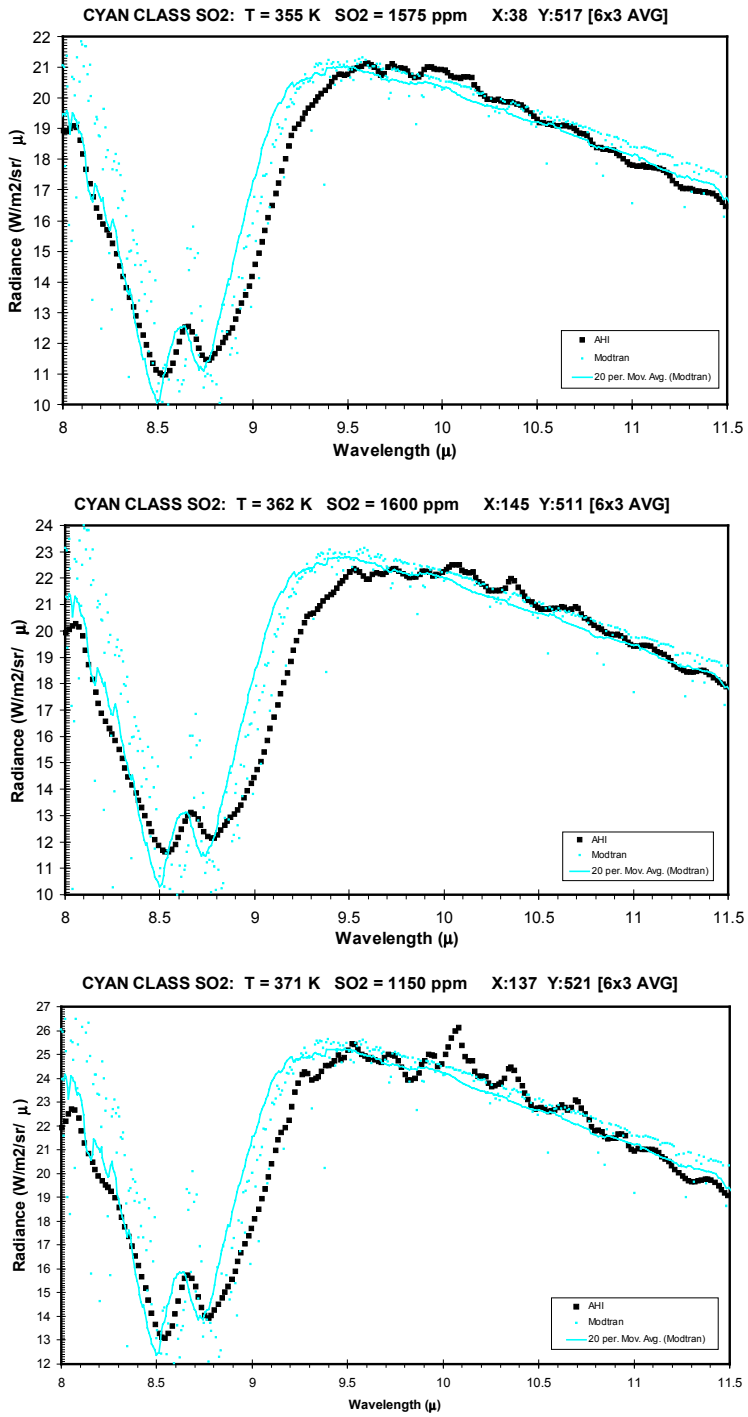

Figure 96. MODTRAN and AHI Radiance Profile Comparison for Pixels of the Orchid SO_2 Class

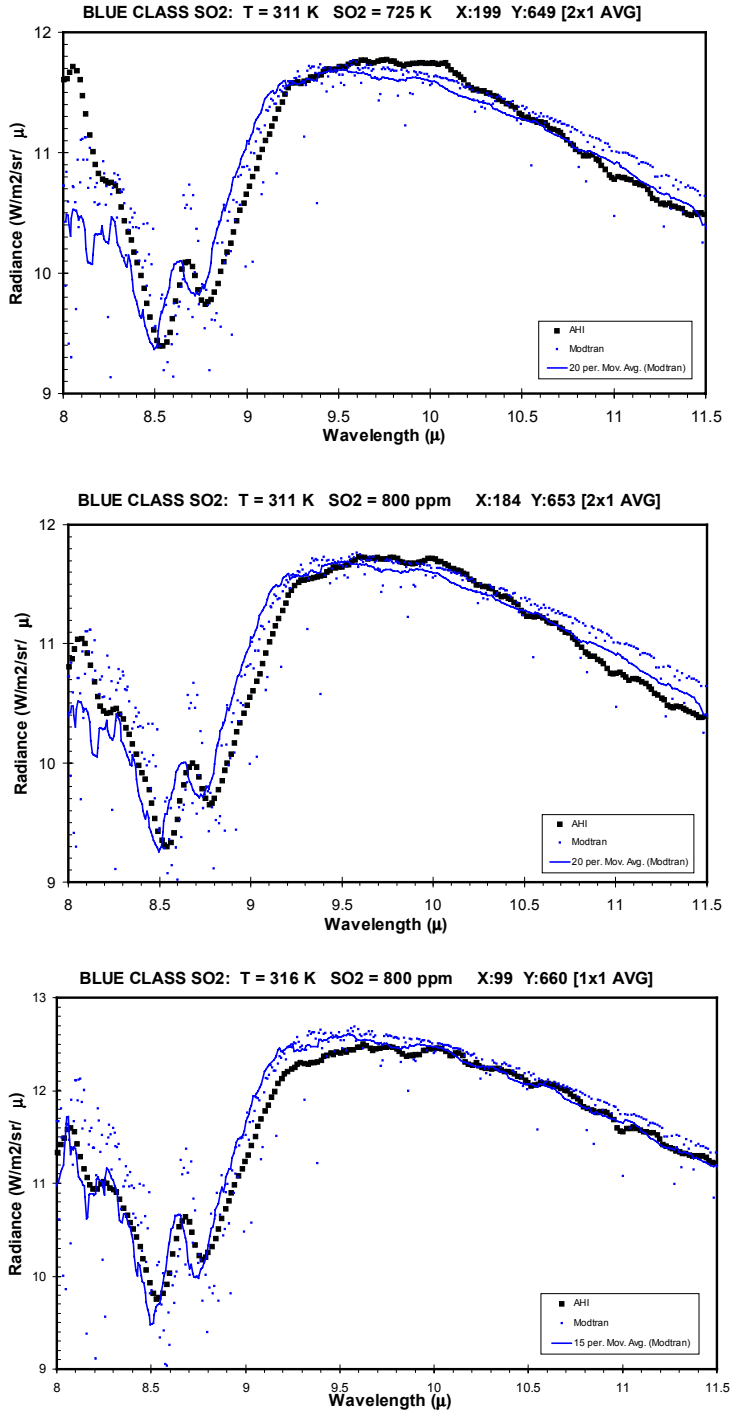

Figure 97. MODTRAN and AHI Radiance Profile Comparison for Pixels of the Orchid SO_2 Class

THIS PAGE INTENTIONALLY LEFT BLANK

LIST OF REFERENCES

Baer-Riedhart, J., "Thermal Infrared Multispectral Scanner", NASA Dryden Flight Research Center, July, 2002. < http://www.dfrc.nasa.gov/airsci/er-2/tims.html>

Berk, A., Anderson, G., Acharya, P., Chetwynd, J., Bernstein, L., Shettle, E., Matthew, M., and Adler-Golden, S., *MODTRAN4 User's Manual*, Air Force Research Laboratory, Space Vehicles Directorate, Hanscom AFB, MA, June, 1999.

Berk, A., Bernstein, and Robetson, D., "MODTRAN: A medium resolution model LOWTRAN-7," *Techinical Report*, GL-TR-89-0122, Geophysics Lab, Hanscom AFB, MA, 1989.

Casadevall, T., Stokes, J., Greenland, L., Malinconico, L., Casadeval, J., and Furukawa, B., 1987, "SO_2 and CO_2 emission rates at Kilauea Volcano, 1979-1984", *Volcanism in Hawaii: U.S. Geological Survey Professional Paper 1350*, v.1, pp. 771-780.

Eilas, T., and Sutton A., 1996, "Long and short-term trends in SO2 eimissions at Kilauea Volcano, Hawaii 1993-1996," *Eos, Transactions, American Geophysical Union*, v. 77, no. 43, p. 670.

Environment for Visualizing Images User's Guide, Research Systems, September, 2001.

Galle, B., Oppenheimer, C., Geyer, A., McGonigle, A., Edmonds, M., and Horrocks, L., "A miniaturized ultraviolet spectrometer for remote sensing of SO2 fluxes: a new tool for volcano surveillance," submitted *to Journal of Vocanology and Geothermal Research.*

Gillespie, A., "Enhancement of Multispectral Thermal Infrared Images: Decorrelation Contrast Stretching," Remote Sensing Environment, v.42, pp. 147-155, 1992.

Greenland, P., Rose, W., and Stokes, J., 1985, "An estimate of gas emissions and magmatic gas content from Kilauea Volcano," *Geochimica et Cosmochimica Acta*, v.49, pp. 125-129.

Heliker, C., Stauffer, P., Hendley, J., "Living on Active Volcanoes – The Island of Hawaii", U.S. Geological Survey Fact Sheet 074-97, August 2000. <http://wrgis.wr.usgs.gov/fact-sheet/fs074-97>

Hook, S., and Howard, L., "Aster", California Institute of Technology, NASA, JPL Home, October, 2001. <http://asterweb.jpl.nasa.gov>

Hydrology Data Support Team, "Thermal Infrared Multispectral Scanner (TIMS)," NASA, December, 1999.
<http://daac.gsfc.nasa.gov/CAMPAIGN_DOCS/SGP97/tims.html>

Kealy, P. and Hook, S., "Separating Temperature and Emissivity in Thermal Infrared Multispectral Scanner Data: Implications for Recovering Land Surface Temperatures," IEEE Transactions on Geoscience and Remote Sensing, vol. 31, no. 6, pp. 1155-1164, November, 1993.

Lucey, P., Williams, T., Mignard, M., Julian, J., Kobubun, D., Allen, G., Hampton, D., Schaff, William, Schlangen, M., Winter, E., Kendall, W., Stocker, A., Horton, K., and Bowman, A., "AHI: an airborne long-wave infrared hyperspectral imager," *SPIE Proceedings*, vol. 3431, pp. 36-43, November, 1998.

Lucey, P., Williams, T., Winter, M., and Winter, E., "Two years of operations of AHI: an LWIR hyperspectral imager," *SPIE Proceedings*, vol. 4030, pp. 31-40.

Lucey, P., Winter, E., "Requirements for calibration of focal plane arrays for imaging spectrometers," *SPIE Proceedings*, vol. 3498, and *EUROPTP Conference on Sensors, Systems, and Next-Generation Satellites II*, Barcelona, Spain, September 1998.

Mouginis-Mark, P., Crisp, J., and Fink, J., Geophysical Monograph 116, *Remote Sensing of Active Volcanism*, American Geophysical Union, 2000.

McGonigle, A., and Oppenheimer, C., "Optical sensing of volcanic gas and aerosol emissions," Department of Geography, University of Cambridge, Dwoning Place, Cambridge, UK, 2002.

Operating Manual and User's Guide USB2000 Miniature Fiber Optic Spectrometers and Accessories, Ocean Optics, Inc., Florida, 2000.

Operation and Maintenance Manual Correlation Spectrometer COSPEC IV, Barringer Research Limited, Rexdale, Ontario, December,1976.

Realmuto, V., "The Potential Use of Earth Observing System Data to Monitor the Passive Emission of Sulfur Dioxide from Volcanoes," Geophysical Monograph 116, *Remote Sensing of Active Volcanism*, American Geophysical Union, 2000.

Realmuto, V., Abrams, M., Fabrizia, V., and Pieri, D., "The use of multispectral thermal infrared image data to estimate the sulfur dioxide flux from volcanoes: A case study from Mount Etna, Sicily, July 29, 1986," *Journal of Geophysical Research*, vol. 99, no. B1, pp. 481-488.

Realmuto, V., Sutton, A., Elias, T., "Multispectral thermal infrared mapping of sulfur dioxide plumes: A case study from the East Rift Zone of Kilauea Volcano, Hawaii," *Journal of Geophysical Research*, vol. 102, no. B7, pp. 15057-15072.

Stefanou, M. S., Olsen, R. C., and Cristi, R., *A Signal Processing Perspective of Hyperspectral Imagery Analysis Techniques*, Master's Thesis, Naval Postgraduate School, Monterey, California, June 1997.

Sutton, A., Elias, T., Gerlach, T., and Stokes, J., "Implications for eruptive processes as indicated by sulfur dioxide emissions from Kilauea Volcano, Hawaii, 1979 – 1997," *Journal of Volcanology and Geothermal Research*, no. 108, pp. 283-302.

Sutton, J., Elias, T., Hendley, J., and Stauffer, P., "Volcanic Air Pollution—A Hazard in Hawaii", U.S. Geological Survey Fact Sheet 169-97, June 2000. <http://wrgis.wr.usgs.gov/fact-sheet/fs169-97>

Tazieff, H., and Sabroux, J., *Forecasting Volcanic Events*, ELSEVIER Amsterdam, New York, 1983.

Tilling, R., Heliker, C., and Wright, T., "Eruptions of Hawaiian Volcanoes (USGS)", U.S. Geological Survey, July, 2002. <http://pubs.usgs.gov/gip/hawaii>

Williams, T., "AHI: Airborne hyperspectral Imager", Hawaii Institute of Geophysics and Planetology, University of Hawaii at Manoa, May, 2002. <http://www.higp.hawaii.edu/ahi>

Williams-Jones, G. and Stix, J., *Using the COSPEC in the field,* Version 10, 2001.

THIS PAGE INTENTIONALLY LEFT BLANK

INITIAL DISTRIBUTION LIST

1. Defense Technical Information Center
   Ft. Belvoir, Virginia

2. Dudley Knox Library
   Naval Postgraduate School
   Monterey, California

3. Richard C. Olsen, Code PH/OS
   Department of Physics
   Naval Postgraduate School
   Monterey, CA

4. Chairman, Code SP
   Space Systems Academic Group
   Naval Postgraduate School
   Monterey, CA

5. David Trask
   MASINT Chair
   Naval Postgraduate School
   Monterey, CA

6. Hawaii Institute Geophysics and Planetology (Attn: Dr Paul G. Lucey)
   University of Hawaii at Manoa
   Honolulu, Hawaii

7. Hawaii Institute Geophysics and Planetology (Attn: Dr Keith Horton)
   University of Hawaii at Manoa
   Honolulu, Hawaii

8. Marine Corps Representative
   Naval Postgraduate School
   Monterey, California

9. Director, Training and Education, MCCDC, Code C46
   Quantico, Virginia

10. Director, Marine Corps Research Center, MCCDC, Code C40RC
    Quantico, Virginia

11. Marine Corps Tactical Systems Support Activity (Attn: Operations Officer)
    Camp Pendleton, California

12. Hawaii Volcano Observatory (Attn: Jeff Sutton / Tamar Elias)
USGS
Volcano, Hawaii

13. Captain Aimee G. Mares
9129 Stonegarden Drive
Lorton, Virginia 22079

14. Cynthia C. Beauman
1102 St. Luke Drive #204
Spencer, Iowa 51301

15. Dr. Harry G. Beauman
14 Saddle Tree Place
Billings, Montana 59106